Determination of Beam Coupling Impedance in the Frequency Domain

Bestimmung von Strahlkoppelimpedanzen im Frequenzbereich
Zur Erlangung des akademischen Grades Doktor-Ingenieur (Dr.-Ing.)
genehmigte Dissertation von Uwe Niedermayer aus Temeschburg / Rumänien
Tag der Einreichung: 09.07.2015, Tag der Prüfung: 24.09.2015
Darmstadt 2016 — D 17

1. Gutachten: Prof. Dr. rer. nat. Oliver Boine-Frankenheim	TEMF / GSI
2. Gutachten: Prof. Dr.-Ing. Thomas Weiland	TEMF

TECHNISCHE
UNIVERSITÄT
DARMSTADT

Fachbereich Elektrotechnik
und Informationstechnik
Institut für
Theorie Elektromagnetischer Felder

Determination of Beam Coupling Impedance in the Frequency Domain
Bestimmung von Strahlkoppelimpedanzen im Frequenzbereich

Genehmigte Dissertation von Uwe Niedermayer aus Temeschburg / Rumänien

1. Gutachten: Prof. Dr. rer. nat. Oliver Boine-Frankenheim TEMF / GSI
2. Gutachten: Prof. Dr.-Ing. Thomas Weiland TEMF

Tag der Einreichung: 09.07.2015
Tag der Prüfung: 24.09.2015

Darmstadt 2016 — D 17

URN: urn:nbn:de:tuda-tuprints-51573
URL: http://tuprints.ulb.tu-darmstadt.de/5157

Erklärung zur Dissertation

Hiermit versichere ich, die vorliegende Dissertation ohne Hilfe Dritter nur mit den angegebenen Quellen und Hilfsmitteln angefertigt zu haben. Alle Stellen, die aus Quellen entnommen wurden, sind als solche kenntlich gemacht. Diese Arbeit hat in gleicher oder ähnlicher Form noch keiner Prüfungsbehörde vorgelegen.

Darmstadt, den 09.07.2015

(Uwe Niedermayer)

Zusammenfassung

Strahlkoppelimpedanzen beschreiben die elektromagnetische Wechselwirkung gleichförmig bewegter geladener Teilchen mit ihrer Umgebung im Frequenzbereich. Sie führen bei hohen Teilchenstrahlintensitäten zu einem Wärmeeintrag in verlustbehafteten Beschleunigerkomponenten sowie zu kohärenten Strahlinstabilitäten. Deshalb muss bereits im Design eines Synchrotrons die Impedanz quantifiziert und möglichst minimiert werden.

Gegenwärtig werden Strahlkoppelimpedanzen meist aus der Fourier-Transformation des Kielwellenpotenzials (*engl.* wake potential) bestimmt, welches das Resultat einer Zeitbereichssimulation ist. Bei niedrigen Frequenzen, niedrigen Strahlgeschwindigkeiten, oder dispersivem Material kann dieses sonst sehr effektive Verfahren jedoch unpraktisch werden. In diesen Bereichen werden heutzutage häufig analytische Berechnungen im Frequenzbereich zusammen mit Geometrieapproximationen angewandt.

Diese Arbeit beschreibt die Entwicklung zweier Simulationswerkzeuge, die die Strahlkoppelimpedanz direkt im Frequenzbereich berechnen. Das erste Werkzeug basiert auf der Finiten Integrations Technik (FIT) auf einem strukturierten Quadergitter und wurde sowohl zweidimensional, als auch dreidimensional implementiert. Das (nicht-konforme) Quadergitter eignet sich jedoch nur schlecht zur Approximation gekrümmter Strukturen. Dies ist insbesondere ein Problem in der Modellierung des Dipolmoments als Quellterm für zur Berechnung der transversalen Strahlkoppelimpedanz.

Das zweite Simulationswerkzeug, welches auf der Finiten Elemente Methode (FEM) und einem unstrukturierten Dreiecksgitter basiert, überwindet dieses Problem. Das Dipolmoment ist hier als Kreisring eingeprägt, dessen Felder im inneren analytisch bekannt sind. Dieses Werkzeug ist zweidimensional implementiert und enthält eine optionale Oberflächenimpedanz-Randbedingung. Es stellt somit eine praktische Möglichkeit zur Bestimmung der Koppelimpedanz langer Strahlrohre dar. Neben beliebiger Frequenz und Strahlgeschwindigkeit können auch dispersive Materialien gewählt werden, was für die Impedanzberechnung von Ferrit-Kickermagneten entscheidend ist.

Numerische Simulationen von Strahlkoppelimpedanzen enthalten immer Vereinfachungen, deren Rechtfertigung an einer Messung überprüft werden muss. Die Koppelimpedanz einer einzelnen Beschleunigerkomponente kann jedoch nicht direkt gemessen werden. Deshalb wurde im Verlauf dieser Arbeit ein neues Hochfrequenztechnik-Labor bei der GSI eingerichtet, um breitbandige Strahlkoppelimpedanzen mit der Drahtmethode indirekt zu messen. Diese Arbeit enthält eine detaillierte Analyse verschiedener Messmethoden in Form eines Vergleiches analytischer Rechnungen, Simulationen und Labormessungen vereinfachter Beschleunigerkomponenten. Eine entscheidende Schlussfolgerung ist hier, dass auch die Labormessung mit einer elektromagnetischen Simulation validiert werden muss.

Die Arbeit schließt mit ausgewählten Effekten der Koppelimpedanz auf den umlaufenden Teilchenstrahl sowie mit ausgewählten Impedanzresultaten für das geplante SIS-100 Synchrotron im Rahmen des FAIR projekts bei der GSI.

Abstract

The concept of beam coupling impedance describes the electromagnetic interaction of uniformly moving charged particles with their surrounding structures in the Frequency Domain (FD). In synchrotron accelerators, beam coupling impedances can lead to beam induced component heating and coherent beam instabilities. Thus, in order to ensure the stable operation of a synchrotron, its impedances have to be quantified and their effects have to be controlled. Nowadays, beam coupling impedances are mostly obtained by Fourier transform of wake potentials, which are the results of Time Domain (TD) simulations. However, at low frequencies, low beam velocity, or for dispersive materials, TD simulations become unhandy. In this area, analytical calculations of beam coupling impedance in the FD, combined with geometry approximations, are still widely used.

This thesis describes the development of two electromagnetic field solvers to obtain the beam coupling impedance directly in the FD, where the beam velocity is only a parameter and dispersive materials can be included easily.

One solver is based on the Finite Integration Technique (FIT) on a staircase mesh. It is implemented both in 2D and 3D. However, the staircase mesh is inefficient on curved structures, which is particularly problematic for the modeling of a dipole source, that is required for the computation of the transverse beam coupling impedance.

This issue is overcome by the second solver developed in this thesis, which is based on the Finite Element Method (FEM) on an unstructured triangular mesh. It is implemented in 2D and includes an optional Surface Impedance Boundary Condition (SIBC). Thus, it is well suited for the computation of longitudinal and transverse impedances of long beam pipe structures of arbitrary cross-section. Besides arbitrary frequency and beam velocity, also dispersive materials can be chosen, which is crucial for the computation of the impedance of ferrite kicker magnets.

Numerical impedance simulations always contain simplifications, therefore they have to be confirmed by dedicated measurements. However, the beam coupling impedance of a single accelerator component cannot be measured directly. Therefore, a dedicated RF-laboratory was established at GSI, in order to measure broadband beam coupling impedances on the bench by means of the wire method, i.e. without beam. A detailed analysis of measurement methods is given by comparison of analytical, numerical, and measurement results for simplified accelerator devices. One conclusion is, that also the bench measurements have to be validated by dedicated electromagnetic simulations.

The thesis closes with selected impedance induced effects on the beam revolving in the synchrotron and relevant impedance results for the future SIS-100 synchrotron for the FAIR project at GSI.

Contents

1 Introduction

Charged particle beams have a variety of applications in science and technology. For protons and heavy ions, the synchrotron is nowadays the best suited acceleration mechanism to obtain high beam energy. The synchrotron allows both to accelerate and to store a charged particle beam. Therefore, it can be used for collision experiments with either fixed targets outside the synchrotron, or as a collider, consisting of two synchrotrons that collide the beam in a particular interaction point within the rings. Since the collisions in a collider can be observed in the center-of-mass frame which is at rest, the observed energy is higher than for a shot on a fixed target observed in the laboratory frame [1]. Nonetheless, in applications beyond elementary particle physics, where the energy is not on the frontier of the technically possible, fixed targets are widely used. Examples of such research areas are nuclear, atomic, and plasma physics, material science, and even biology and medicine.

A major topic of accelerator physics research, i.e. accelerator development, is to obtain maximum beam intensity stored in the synchrotron. In contrast to the maximum beam energy, which depends only on the maximum magnet strength, the maximum beam intensity has a variety limiting factors. These are distinguished between *single-particle effects* and *collective effects*, where collective effects refer to the influence of the 'ensemble' (all the particles) on a test particle. Examples of collective effects are space charge or beam-beam effects, vacuum and electron cloud issues, and, as treated in this thesis, impedance induced *'coherent'* beam instabilities. Within the collective effects, one distinguishes between *incoherent* and *coherent* phenomena, i.e. the particles moving individually or as a whole. Impedance induced beam instabilities are coherent, however, their natural stabilization mechanism, 'Landau damping' [2], is based on momentum *spreads*, i.e the dissimilarity between individual particles (incoherent).

Generally, this thesis deals with the electromagnetic interaction of charged particles with their environment, i.e. accelerator components. Due to the periodic revolution of the particles in the synchrotron ring, it can be advantageous to describe this interaction in the frequency domain. This is called *'beam coupling impedance'* and features many well known properties of the electrical engineering term 'impedance' in the sense of Ohm's law.

The focus of this thesis is on ion synchrotrons, where the velocity of the particles can be significantly lower than the speed of light. Examples of such accelerators are the SIS-18 [3] at GSI (Gesellschaft für Schwerionenforschung) and the SIS-100 [4] for the upcoming FAIR (Facility for Antiproton and Ion Research) project at GSI. The particle bunches used in these machines are long (several meters) and thus lead to a beam spectrum at low frequencies (several MHz). Also the injector chain for the LHC (Large Hadron Collider) [5] at CERN and secondary beam decelerator rings such as the

Extreme Low ENergy Antiproton Ring (ELENA) [6], projected at CERN, face challenges of subrelativistic beams.

Another focus of this thesis is put on relativistic proton and ion beams in very large synchrotrons. The large size of the ring leads to a very low revolution frequency. Therefore, the sidebands of the spectrum, which are susceptible to impedance driven beam instabilities, are also at very low frequencies. For example, one scenario of a post-LHC accelerator is given by the Future Circular Collider (FCC) [7] design study. The FCC proton-proton scenario is outlined for collisions up to 100 TeV in the center of mass. For a projected magnet strength of 16 T this requires a tunnel circumference of roughly 100 km, resulting in a revolution frequency of only 3 kHz [8].

At these low frequencies, frequency domain beam coupling impedance simulation methods are better suited than time domain methods.

This thesis deals with techniques to determine the beam coupling impedance directly in the frequency domain by means of analytic and numeric computation and by means of measurement. Before motivating this work in detail, the basic principle of a synchrotron is introduced. An overview of the treated topics will be given in Sect. 1.3.

Throughout this thesis SI units are used. A description and the unit for each symbol can be found in the Symbol List in Appendix G. Unless stated otherwise, all quantities are observed in the laboratory reference frame.

1.1 Synchrotron Accelerators for Intense Ion Beams

The basic layout of a synchrotron is depicted in Fig. 1.1. It contains magnets for deflection and focusing of the beam as well as cavities to provide an alternating electric field for acceleration. Usually the beam is preaccelerated by a Linear Accelerator (LINAC) and injected into the synchrotron by a fast pulsed magnet (kicker magnet).

The beam energy is a design quantity connected to the magnetic rigidity by

$$B\,R = p/q, \tag{1.1}$$

where B is a homogeneous magnetic field, R is the particle trajectory bending radius in the magnetic field, and p, q are the particle's momentum and charge, respectively. Thus, the magnetic rigidity $B \cdot R$ defines the momentum of a synchronous particle, which is connected to its energy by

$$E = \gamma m c^2 = \sqrt{m^2 c^4 + p^2 c^2}, \tag{1.2}$$

where γm is the relativistic mass and c is the speed of light in vacuum.

Within the aperture of a magnet, the magnetostatic field is both divergence- and curl-free and can thus be derived from a scalar potential satisfying the Laplace equation with

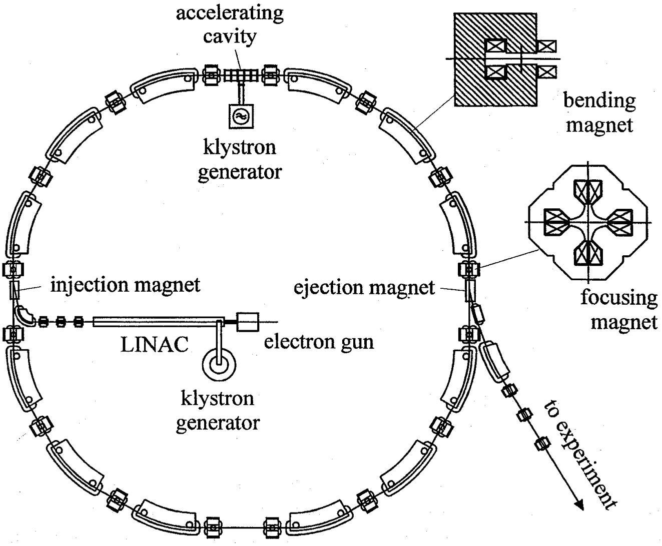

Figure 1.1.: Basic design of a synchrotron. Picture from [1].

appropriate boundary conditions. The thereby obtained field in any normal oriented[1] magnet in the synchrotron can be described in cylindrical coordinates ϱ, φ as [9]

$$\vec{B}(\varrho,\varphi) = B_0 \sum_{n=1}^{\infty} c_n \left(\frac{\varrho}{r_0}\right)^{n-1} \left(\sin((n-1)\varphi)\vec{e}_x + \cos((n-1)\varphi)\vec{e}_y\right), \tag{1.3}$$

where r_0 is a reference radius that defines a two-dimensional (2D) disc[2] on which the Laplace equation is solved. As illustrated in Tab. 1.1, $n = 1$ denotes dipoles, $n = 2$ quadrupoles, $n = 3$ sextupoles and so on. In a particular magnet of order n, its respective coefficient dominates and the other coefficients can be used to describe the magnetic field errors. For example, the field created by an n-pole in the x,z-plane ($\varphi = 0$) reads

$$B_{y,n}(x, y = 0) = B_0 c_n \left(\frac{x}{r_0}\right)^{n-1}, \tag{1.4}$$

from which one can observe that the $(n-1)$-th derivative is constant. This gives rise to a definition of a respective multipole coefficient as denoted in the third column of Tab. 1.1.

---

[1] A complete basis also requires the skew magnet multipoles, which are rotated by $\pi/(2n)$.

[2] For simplicity, fringe fields, where a longitudinal component is present, have been neglected.

Table 1.1.: Magnet types in a synchrotron.

Multipole order	Magnet type	Defining equation	Application
1	Dipole	$\frac{1}{R} = \frac{q}{p} B_y$	Deflection
2	Quadrupole	$\kappa_x = \frac{q}{p} \partial_x B_y$	Focusing
3	Sextupole	$m_x = \frac{q}{p} \partial_x^2 B_y$	Chromaticity control
4	Octupole	$o_x = \frac{q}{p} \partial_x^3 B_y$	Landau damping control
$\vdots$			

Only the dipole magnets act on the beam as a whole, higher multipoles provide focusing dependent on the offset from the center, i.e. each particle is affected differently. Quadrupole magnets provide linear focusing and defocusing in the two transverse planes. They can be set up as periodic focusing channels, e.g. so-called FODO-channels, providing a net focusing in both planes. This so-called ‘strong focusing’ concept [10] allows to store high beam intensities in the synchrotron. Sextupoles, octupoles, and higher order multipoles provide nonlinear focusing. They are used to control lattice errors and the beam stability.

The Radio-Frequency (RF) cavities in a synchrotron provide acceleration and longitudinal focusing. They create the RF-potential well[3] (bucket) in which the particles perform the so-called synchrotron oscillations. When the phase of the RF-wave is chosen such that the RF-voltage is positive at the moment a particle passes the cavity gap, an acceleration takes place.

The crucial property of a synchrotron is that everything has to be synchronized. For a beam that is stored at constant energy, this is in principle described by Eq. 1.1. During acceleration, the energy increase has to be synchronized with the field increase in every magnet as [11]

$$CR\dot{B}_0 \approx \frac{T_0}{q} \dot{E} \approx U_0 \sin \varphi_0, \tag{1.5}$$

where C is the ring circumference, T_0 is the revolution time and U_0 and φ_0 are the acceleration voltage and phase, respectively. The revolution time $T_0 = 1/f_0$ can be seen as a constant only at ultrarelativistic energy, otherwise the revolution frequency f_0 increases proportional to the particle velocity. However, Eq. 1.5 still holds for low energy synchrotrons with $T_0 = T_0(E)$, but it is particularly challenging to synchronize the RF-frequency[4] according to the increasing beam velocity during the acceleration ramp. For this purpose, tunable ferrite cavities are employed, where the resonance frequency can be set by a DC bias current, which determines a working point on the ferrite hysteresis curve. The resonance frequency and the generator frequency and phase need to be precisely controlled in feedback loops including the beam signal. If all the synchronicity

---

[3] In the reference frame of the beam, the RF-wave looks like a constant potential.

[4] The RF-frequency must be an integer harmonic of the revolution frequency, i.e. $f_{\mathrm{RF}} = hf_0$, $h \in \mathbb{N}$.

conditions are fulfilled, the trajectory of an idealized particle in the synchrotron is fixed (independent of the energy) and non-ideal particles can be analyzed by means of small deviations from the ideal particle.

In order to obtain highest beam intensities, all components of the synchrotron need to be optimized. The beam coupling impedance is a powerful tool for the analysis and optimization of the electromagnetic interaction between the beam and its environment. This interaction can lead to intensity dependent beam instabilities and accelerator component heating. Thus, in order to push the intensity higher, the machine impedance has to be understood and, if possible, reduced.

For the intensity limitations originating from the machine impedance, only the components which are 'visible' for the beam have to be taken into account. These are in particular:

- Beam pipe (only weakly lossy, but very long and close to the beam)
- Cavities (fundamental and higher order modes (HOMs))
- Collimators (very close to the beam and sometimes strongly lossy)
- Kicker magnets (dispersively lossy and coupling to external supply network)
- Diagnostic equipment (sometimes close to the beam).

A complete impedance model of a synchrotron should include all these components. However, since obtaining all those impedances is a huge effort (see e.g. [12]), simplified models gain importance.

1.2 Motivation

The goal of this thesis is to provide and analyze numerical and measurement tools to obtain impedance data for particular components in the synchrotron ring. The focus is on structures and frequencies, for which contemporary Time Domain (TD) simulation tools are not suitable.

The constituents of an impedance model for a synchrotron are nowadays mostly obtained by TD simulation, which is well suited only at medium and high frequency (HF). At low frequencies, due to Küpfmüller's uncertainty principle, TD simulations are required to run for a long interval of time. However, due to spatial mesh properties, it is not possible to enlarge the time step[5]. Thus, a strong oversampling happens at low frequency, which makes the otherwise very efficient explicit TD methods unhandy.

Frequency domain (FD) methods allow an arbitrary choice at which points the frequency axis is sampled. However, each frequency point requires solving a Linear System of Equations (LSE), which is costly when the number of unknowns is high. Therefore, FD methods have a particular strength in 2D simulations where the number of

---

[5] This applies only to explicit TD methods which are limited by the CFL criterion.

unknowns can be kept moderate. Particularly for future synchrotron projects, when design changes are still being undertaken, quick 2D impedance estimates are useful to facilitate decisions with the goal of impedance minimization.

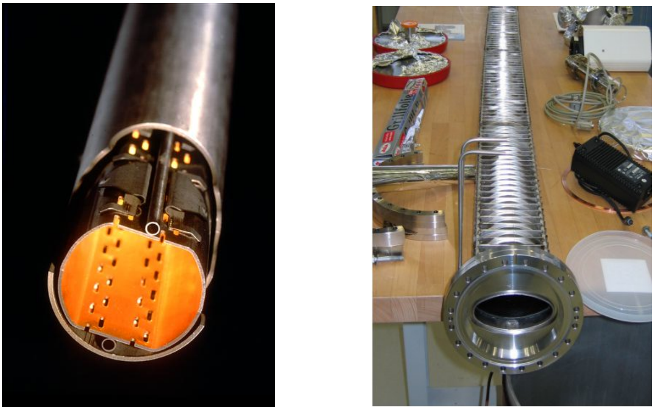

(a) LHC (Pic.: CERN [13]) **(b)** SIS-100 for FAIR

Figure 1.2.: Examples of synchrotron beam pipes (different scales).

Nowadays, beam coupling impedance calculation in the FD is done mostly analytically. For example, the impedance of the beam pipe of the LHC (see Fig. 1.2a) has been computed as if it was circular and form factors were applied [14]. Such theory is very involved, lengthy, and applicable only for particular geometries and particular frequency ranges. The impedance of the elliptical SIS-18 beam pipe, similarly to the one for SIS-100 (see Fig. 1.2b), was estimated by a circular pipe with equivalent radius, which was found inaccurate by a factor of 3 [15] [6].

A 2D FD impedance computation tool is well suited to compute the impedance of a beam pipe. Moreover, dispersive materials can be included easier in the FD, which is required for the computation of the impedance of kicker magnets. Pulsed kicker magnets are used for the injection and extraction of the beam in the synchrotron and they are usually made of dispersively lossy ferrite (see Fig. 1.3).

Another issue, at which FD computation is better suited than TD, is (very) low beam velocity. In the FD the beam velocity is just a parameter, whereas in TD involved boundary conditions are required for the entry and exit of a non-ultrarelativistic beam in the computational domain [17]. Even 3D computations in the FD can employ Floquet (quasi-periodic) boundary conditions for arbitrary beam velocity, which are easy to implement on a structured mesh.

---

[6] Later numerical computations with a quasi-stationary approach [16] could significantly improve the agreement with measured beam instability rise time.

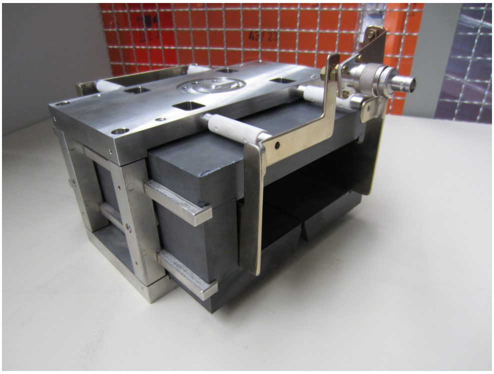

Figure 1.3.: SIS-18 kicker magnet. The horizontal kick is created by a vertical magnetic field. The coil has only one turn and is fixed by the white ceramic insulators. The BNC connector at the end is applied for an inductance measurement, see Fig. F.4 for the inductance as function of the frequency.

Since beam coupling impedance simulations are generally very involved for complicated accelerator structures, simulations have to be accompanied by dedicated measurements in order to gain confidence in the results. Thus, this thesis also includes an analysis of broadband impedance bench measurement methods.

1.3 Overview

After introducing the concept of a synchrotron in Sect. 1.1, the required fundamentals to work with beam coupling impedances in synchrotrons are given in Chapter 2. These are the definitions of wake functions and beam coupling impedances and the theorem of Panofsky and Wenzel, which draws conclusions on properties of the wake functions and impedances solely from Maxwell's equations in vacuum. Additionally, the beam physics in synchrotrons is introduced, in order to derive the equations of motion for beam instabilities.

Chapter 3 deals with wave equations and material properties, which are required for the analytical calculation of beam coupling impedance. Here, also quasi-stationary approaches are introduced. Space charge and (simplified) resistive wall impedances are calculated, as they serve as validation examples in the following chapters.

Numerical methods for the computation of beam coupling impedance in the frequency domain are presented in Chapter 4. After a brief introduction of contemporary time domain methods, the implementation of a FIT (2D/3D) method and a FEM (2D) method in the frequency domain are shown. Both methods are validated on analytic examples, before being applied to structures that cannot be addressed analytically.

Chapter 5 discusses the impedance bench measurements that have been performed in a new RF-laboratory at GSI, which has been established in the framework of this thesis.

Finally, Chapter 6 shows selected consequences of coupling impedances, i.e. heat load and (basic) beam instabilities. Some selected impedance results, which are relevant for the FAIR SIS-100, are presented.

The thesis concludes with a summary and outlook.

2 Fundamentals

2.1 Maxwell's Equations and Particle Beams

A complete macroscopic description of electromagnetic (EM) fields as function of position $\vec{r} \in \Omega \subset \mathbb{R}^3$ and time $t \in \mathbb{R}$ is given by Maxwell's equations[1] (see App. G for the naming of each vector field)

$$\nabla \times \vec{E}(\vec{r},t) = -\partial_t \vec{B}(\vec{r},t) \tag{2.1a}$$

$$\nabla \times \vec{H}(\vec{r},t) = \vec{J}_s(\vec{r},t) + \vec{J}(\vec{r},t) + \partial_t \vec{D}(\vec{r},t) \tag{2.1b}$$

$$\nabla \cdot \vec{D}(\vec{r},t) = \varrho_s(\vec{r},t) \tag{2.1c}$$

$$\nabla \cdot \vec{B}(\vec{r},t) = 0 \tag{2.1d}$$

and material equations

$$\vec{D}(\vec{r},t) = \varepsilon(\vec{r})\vec{E}(\vec{r},t) \tag{2.2a}$$

$$\vec{B}(\vec{r},t) = \mu(\vec{r})\vec{H}(\vec{r},t) \tag{2.2b}$$

$$\vec{J}(\vec{r},t) = \kappa(\vec{r})\vec{E}(\vec{r},t), \tag{2.2c}$$

where ϱ_s and $\vec{J}_s$ denote the source charge and current densities, respectively. The material distribution given by the permittivity ε, the conductivity κ and the permeability μ, which are assumed to be linear and isotropic. At first, the material is also assumed to be non-dispersive. By means of Gauss' and Stokes' theorems, Maxwell's equations can also be written in integral form, which is more general, since the differentiability requirements of the field vector functions can be relaxed.

The force acting on a charged particle[2] $i = 1 \dots N$ is

$$\vec{F}_i(t) = q_i \left(\vec{E}(\vec{r}_i,t) + \vec{v}_i(t) \times \vec{B}(\vec{r}_i,t) \right), \tag{2.3}$$

where q_i and $\vec{v}_i$ are the particle's charge and velocity, respectively.

---

[1] Maxwell originally wrote his equations component-wise [18, 19], the application of vector differential operators was first done by Heaviside [20] and independently by Gibbs and Hertz (see e.g. [21])

[2] The particle is assumed to be point-like.

For a description of particle motion in both their own and external fields, Maxwell's equations have to be coupled with the equations of mechanics,

$$\vec{F}_i(t) = \partial_t \vec{p}_i(t) \tag{2.4}$$

$$\vec{p}_i(t) = \gamma_i(t) m_i \vec{v}_i(t) \tag{2.5}$$

where the the relativistic mass and velocity factors are

$$\gamma = \frac{1}{\sqrt{1-\beta^2}} \quad \text{and} \quad \beta = \frac{|\vec{v}|}{c}, \tag{2.6}$$

and $\vec{p}_i(t)$ is the i-th particle's momentum.

In order to use the charge and current of the particles as sources for Maxwell's equations, they have to be expressed as smooth vector fields, i.e.

$$\varrho_s(\vec{r}) = \sum_i q_i \delta_\xi(\vec{r} - \vec{r}_i) \tag{2.7a}$$

$$\vec{J}_s(\vec{r}) = \sum_i q_i \delta_\xi(\vec{r} - \vec{r}_i)\vec{v}_i, \tag{2.7b}$$

where δ_ξ is a particular square-integrable representation of the δ-function (mollifier) with $\delta_\xi \to \delta$ for $\xi \to 0$. A finite ξ controls how the point-like particles are smeared out.

A tight coupling of Maxwell's equations with the equations of motion is referred to as 'self-consistent' description. This term originates from plasma physics, where the motion of a huge number of particles is studied. In beam physics, many concepts from plasma physics have been adopted, see e.g. [22]. However, in contrast to plasma physics, the external EM fields (magnets, cavities, etc.) acting on a beam in the accelerator are usually much stronger than the ones created by the beam itself [23].

Different approximation approaches to self-consistency can be made, dependent on the time-scale of the problem. A famous simulation approach for beams and plasmas is the Particle-In-Cell (PIC) method (see e.g. [24]), where a huge number of point-like particles are lumped in a smaller number of finite-sized macro-particles. In each time step Δt, the equations for the electromagnetic fields (mean-fields) are solved, interpolated on the particles, the particles pushed and again the fields due to the new sources are computed (see Fig. 2.1a). Such an approach is analytically self-consistent only in the limit $\Delta t \to 0$. Nonetheless, if the problem has a certain time scale, a numerical approach can be self-consistent even for a finite Δt being much smaller than the problem's time scale.

In synchrotrons, the EM fields originating from the beam particles and acting back on the beam are usually not strong enough to destroy the beam within one revolution. However, over many turns, these fields can cause a destructive self-amplifying instability. Thus, such an instability must have a rise time that is much longer than the revolution period and it suffices to compute the impact of those parasitic EM-fields on

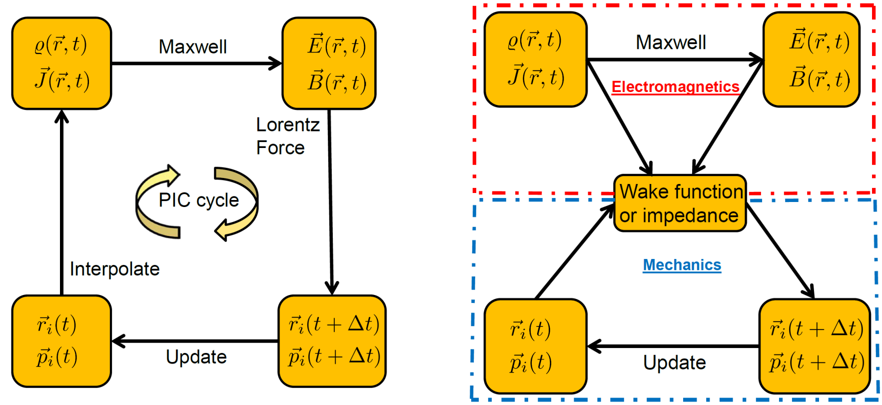

(a) Description of particle motion in electromagnetic fields. For full analytic self-consistency $\Delta t \to 0$ is required. Numerical approaches can, dependent on the time scale of the problem, allow finite Δt and still be self-consistent.

(b) Description of particle motion with wake fields. The electromagnetic forces are precomputed using a rigid beam as source. For synchrotrons, the time step is usually one revolution period, which is a good approximation for multi-turn phenomena.

Figure 2.1.: Particle in Cell (PIC) simulation loop vs. wake field approach.

the beam only once per turn. This is done by the ring wake function or ring impedance, see Fig. 2.1b.

The wake function or beam impedance approach decouples the equations of electromagnetics from the ones of mechanics, i.e. the self-consistency is broken. A precomputed wake function or impedance, which is a description of the environment of a particle beam, is calculated by solving Maxwell's equations subject to a rigid beam excitation. Due to the linearity of Maxwell's equations, the wake-force scales linearly with the source charge. In other words, the deceleration voltage scales linearly with the beam current, which motivates the impedance concept as it was originally proposed by Vaccaro [25] in 1966. Such a voltage can then be used to apply kicks in a periodic manner to (macro-) particles and track them by solving their equations of motion. When the time scale of the EM field effects is much longer than one turn, the particle tracking with wake functions is a good approximation to the much more expensive self-consistent simulation.

Examples of such 'beam dynamics with wake fields' codes are PATRIC [26] or HEADTAIL [27], which simulate only the direct interaction between beam particles with PIC and require a description of the surrounding equipment by means of the ring wake function or beam coupling impedance. Since all the particles in a synchrotron travel at nearly the same speed[3], the direct particle-particle interaction is in good approximation only electrostatic. Thus, only a Poisson solver is required to close the PIC loop. Nowadays such Poisson solvers are extremely fast, such that the interpolation of the particles to the mean field mesh and the evaluation of the electrostatic mean fields on the position of the particles (which is another interpolation) are significant constituents of the overall computation time. The expensive computation of full Maxwell EM fields, required to describe the interaction of the beam with its surrounding structures, is done only once and included in the linear wake function. Finally, such an approach is able to simulate involved particle accelerator processes, such as e.g. the stabilization of a beam instability due to the wall resistivity by Landau damping.

2.2 Frequency Domain

The periodic revolution of the beam in a synchrotron motivates to describe the motion in the frequency domain. This arises also from practical considerations, as TD phenomena in a synchrotron are more difficult to observe than beam spectra. The theories for longitudinal and transverse beam spectra follow in their basic principles the spectra of frequency- and amplitude-modulation, respectively, as known from communication theory. An overview, also in the context of the distinction between coherent and incoherent beam phenomena, is given in [28].

In this framework the following convention for the Fourier transform is used:

$$\underline{F}(\omega) = \mathscr{F}\{f(t)\}(\omega) = \int_{-\infty}^{\infty} f(t) e^{-i\omega t} \mathrm{d}t. \tag{2.8}$$

The inverse transform reads

$$f(t) = \mathscr{F}^{-1}\{\underline{F}(\omega)\}(t) = \frac{1}{2\pi} \int_{-\infty}^{\infty} \underline{F}(\omega) e^{+i\omega t} \mathrm{d}\omega, \tag{2.9}$$

and between the two domains holds Parsevals's (unitarity) theorem[4].

$$||\underline{F}||_{\mathscr{L}^2} = \sqrt{2\pi}||f||_{\mathscr{L}^2}. \tag{2.10}$$

The square of the $\mathscr{L}^2$-norm (see App. B) defines the signal energy

$$E = ||f||^2_{\mathscr{L}^2} = \int_{-\infty}^{\infty} |f(t)|^2 \mathrm{d}t. \tag{2.11}$$

---

[3] In the reference frame of the synchronous particle, the motion of all other particles can be seen as non-relativistic.

[4] More generally Plancherel's theorem states $(\underline{F}, \underline{G}^*) = 2\pi(f^*, g)$ and the Fourier transform is an unitary isomorphism from $\mathscr{L}^2(\mathbb{R})$ to $\mathscr{L}^2(\mathbb{R})$.

Finite energy requires $f \in \mathscr{L}^2(\mathbb{R})$, but we will also allow distributions, such as the Dirac δ–distribution, to be Fourier transformed, keeping in mind that this represents infinite energy. The duration and bandwidth of a signal $f(t)$ are defined as[5] [29]

$$T = \frac{\|tf(t)\|_{\mathscr{L}^2}}{\|f(t)\|_{\mathscr{L}^2}} \tag{2.12}$$

$$B = \frac{\|\omega \underline{F}(\omega)\|_{\mathscr{L}^2}}{\|\underline{F}(\omega)\|_{\mathscr{L}^2}}. \tag{2.13}$$

The two fulfill the Küpfmüller uncertainty principle [30]

$$T \cdot B \geq 1/2, \tag{2.14}$$

where equality is achieved for a Gaussian pulse.

As common in electrical engineering, the underline emphasizes complex quantities. This serves also to distinguish between real valued functions in TD and complex ones in FD. Unless stated otherwise, spectral densities, i.e. Fourier transformed quantities, are used. This is not to be confused with the phasor notation which is very common in engineering. Apart from the fact that a function $\underline{G}(\omega) = \mathscr{F}(g(t))$ contains only the single frequency ω (not $-\omega$) and it is in units of $[g]/\text{Hz}$, it can be used in the same manner as the phasor notation. Additionally, the spectral density enables the representation of arbitrary broadband periodic and non-periodic signals.

Applying Eq. 2.8 to Eqs. 2.1, Maxwell's equations read in the frequency domain

$$\nabla \times \underline{\vec{E}}(\vec{r},\omega) = -i\omega \underline{\vec{B}}(\vec{r},\omega) \tag{2.15a}$$

$$\nabla \times \underline{\vec{H}}(\vec{r},\omega) = \underline{\vec{J}}_s(\vec{r},\omega) + \underline{\vec{J}}(\vec{r},\omega) + i\omega \underline{\vec{D}}(\vec{r},\omega) \tag{2.15b}$$

$$\nabla \cdot \underline{\vec{D}}(\vec{r},\omega) = \underline{\varrho}_s(\vec{r},\omega) \tag{2.15c}$$

$$\nabla \cdot \underline{\vec{B}}(\vec{r},\omega) = 0, \tag{2.15d}$$

where the material relations can easily include dispersive materials as

$$\underline{\vec{D}}(\vec{r},\omega) = \varepsilon_0 \underline{\varepsilon}_r(\vec{r},\omega) \underline{\vec{E}}(\vec{r},\omega) \tag{2.16a}$$

$$\underline{\vec{B}}(\vec{r},\omega) = \mu_0 \underline{\mu}_r(\vec{r},\omega) \underline{\vec{H}}(\vec{r},\omega) \tag{2.16b}$$

$$\underline{\vec{J}}(\vec{r},\omega) = \kappa(\vec{r},\omega) \underline{\vec{E}}(\vec{r},\omega). \tag{2.16c}$$

---

[5] For simplicity we consider both the signal and the spectrum as mean value free.

The real and imaginary parts of the material parameters are usually written as

$$\underline{\mu} = \mu_0(\mu_r' - i\mu_r'') \tag{2.17a}$$

$$\underline{\varepsilon} = \varepsilon_0(\varepsilon_r' - i\varepsilon_r'') - i\frac{\kappa}{\omega}, \tag{2.17b}$$

where κ or ε_r'' is preferred to describe the losses in metals or dielectrics, respectively. Finally, we define the magnetic reluctivity as

$$\underline{\nu} = \underline{\mu}^{-1} = \frac{\mu' + i\mu''}{|\underline{\mu}|^2}. \tag{2.18}$$

2.3 Beam Dynamics in Synchrotrons

For the description of particle motion in synchrotrons one introduces a coordinate system (x, y, s) for the horizontal, vertical, and longitudinal position *deviation* from a reference particle at $(0, 0, z)$, see Fig. 2.2.

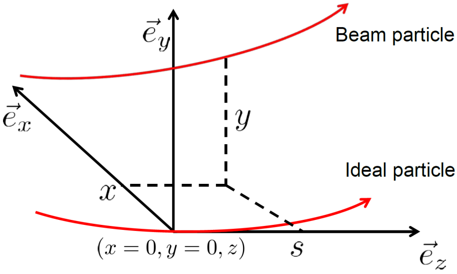

Figure 2.2.: Coordinate system in the synchrotron.

The vector $\vec{R}(z) = (x, x', y, y', s, \Delta p/p_0)^{\mathrm{T}}$ denotes the position of a particle in 6-dimensional phase space, where $x' = \partial_z x$, $y' = \partial_z y$ and s and Δp are the longitudinal position and momentum deviation from the ideal particle, respectively. Note that s can also be understood as time advance or delay with respect to the ideal particle. Generally, $\vec{R}$ can be linearly mapped from one position z to another $\tilde{z}$ in the synchrotron by a matrix

$$\vec{R}(\tilde{z}) = \mathbf{M}_{z\tilde{z}}\vec{R}(z). \tag{2.19}$$

In this framework we will assume that the horizontal, vertical, and longitudinal phase space planes are uncoupled, i.e. $\mathbf{M}_{z\tilde{z}}$ is block-diagonal. However, it will be allowed that the dynamics in one plane depend on another by constant parameters.

The entries of $\mathbf{M}_{z\tilde{z}}$ are determined by the lattice properties[6], such as e.g. the quadrupole focusing strength κ_x (see again Tab. 1.1), which are all periodic functions of the position z, i.e. $\kappa_x(z) = \kappa_x(z + C)$. Quadrupoles provide additionally $\kappa_y(z) = -\kappa_x(z)$.

The equations of transverse motion for a single particle (usually referred to as Hill's equation) are found from $F_{x/y} = p'_{x/y} v_z$ and read [31][7]

$$x'' + \kappa_x(z)x = \frac{1}{R(z)} \frac{\Delta p}{p} \tag{2.20a}$$

$$y'' + \kappa_y(z)y = 0, \tag{2.20b}$$

where $R(z)$ is the local curvature of the ideal trajectory. The ordinary differential equations (ODE) 2.20 provide homogeneous solutions of the pseudo-periodic[8] type [10, 31]

$$y_\beta(z) = \sqrt{\epsilon_y} w_y(z) \cos(\psi_y(z) - \psi_0), \tag{2.21}$$

where $\beta_y = w_y^2$ is the periodic betatron amplitude function and ϵ_y is the so-called Courant-Snyder invariant [10] or single-particle-emittance. Inserting Eq. 2.21 into 2.20, the equations

$$w''(z) - \frac{1}{w^3(z)} + \kappa(z)w(z) = 0 \tag{2.22a}$$

$$\psi'(z) - \frac{1}{w^2(z)} = 0 \tag{2.22b}$$

are readily found in both planes x and y, respectively. The solution of an inhomogeneous ODE as Eq. 2.20a is given as the sum of general homogeneous solution and particular solution, i.e. $x = x_\beta + x_D$. The particular solution x_D determines the dispersion function, i.e. the abberation from the ideal trajectory due to momentum offset

$$x_D(z) = D(z) \frac{\Delta p}{p}. \tag{2.23}$$

The dispersion function $D(z)$ is subject to the ODE [31]

$$D''(z) + \kappa_x(z) D(z) = \frac{1}{R(z)}. \tag{2.24}$$

---

[6] It is rather involved to obtain the complete matrix, see e.g. [31].

[7] The dependence on the (assumed constant) momentum deviation is introduced here, since it has an influence on the beam size.

[8] x_β is (non-)periodic for (ir-)rational tune. An entirely periodic solution can be obtained by applying the Floquet transformation to Hill's equation, see e.g. [32].

The betatron amplitude functions $\beta_x(z), \beta_y(z)$ and the dispersion function $D(z)$ are assumed to be given throughout this thesis. In practice they are obtained by numerical integration of the ODEs 2.22a and 2.24 for the given accelerator lattice using programs like MAD-X [33] (Methodical Accelerator Design). Finally, one finds the local beam size as function of the emittance and momentum spread as [34]

$$a_x^{\mathrm{rms}}(z) = \sqrt{\beta_x(z)\epsilon_x^{\mathrm{rms}} + (D(z)\Delta p^{\mathrm{rms}}/p)^2} \tag{2.25a}$$

$$a_y^{\mathrm{rms}}(z) = \sqrt{\beta_y(z)\epsilon_y^{\mathrm{rms}}}. \tag{2.25b}$$

The betatron tune is the number of betatron oscillation per beam revolution. It is obtained from the lattice as

$$Q_{x/y} = \frac{\psi_{x/y}(C)}{2\pi} = \frac{1}{2\pi}\oint \psi'_{x/y}(z)\mathrm{d}z = \frac{1}{2\pi}\oint \frac{\mathrm{d}z}{\beta_{x/y}(z)}. \tag{2.26}$$

Rational values of the tune lead to x_β or y_β (cf. Eq. 2.21) being periodic. A particle that passes a lattice error at z_0 periodically, is resonantly driven away from the ideal trajectory. The vulnerability of the beam to such resonances is quantified by the resonance order $m+n$, where

$$mQ_x + nQ_y = p \tag{2.27}$$

for $m, n, p \in \mathbb{Z}$. Intensity effects, such as space charge, change the tune for each particle individually. This leads to an (e.g. amplitude dependent) tune spread ΔQ. The tune distribution, however, needs to be fit in between the resonance lines described by Eq. 2.27, which limits the magnitude of the tune spread. In high intensity synchrotrons one considers the fourth order resonance as a (conservative) intensity limit, i.e.

$$N \propto \Delta Q_{x,y} < 1/4, \tag{2.28}$$

where N is the number of particles, see e.g. [35], p. 235 for a detailed discussion.

In order to discuss impedance dependent beam instabilities, which evolve in time scales much larger than T_0, it makes sense to find an equation similar to 2.20 but depending on time $t = nT_0$ rather than on a particular position z in the ring. Such an equation should provide a periodic solution and include a driving term. When z looses its meaning, so does the local oscillation amplitude $w(z)$. This leads to the so-called constant focusing approximation, i.e. $\beta(z)$ is replaced by a constant $\hat{\beta}$ obtained from appropriate averaging.

In order to achieve this, we rewrite Eq. 2.20 as[9]

$$\left[\partial_t^2 + (v\sqrt{\kappa(z)})^2\right] y = 0. \tag{2.29}$$

---

[9] Here we refer only to the vertical plane, y. However, the same formalism applies to x as well.

When looking at Eq. 2.22a and assuming constant envelope, i.e. $w'' = 0$, the focusing strength $\kappa_y(z)$ can be replaced by $\hat{\kappa}(z) \approx w_y^{-4}(s) = \beta_y^{-2}(z)$. The proper average $\hat{\beta}_y$ of $\beta_y(z)$ is then given by the ring average of the oscillation frequency in Eq. 2.29, i.e.

$$\omega_{\beta,y} = \frac{1}{C} \oint v \sqrt{\hat{\kappa}_y(z)} \mathrm{d}s = \frac{v}{C} \oint \frac{\mathrm{d}s}{\beta_y(z)} = Q_y \omega_0. \tag{2.30}$$

The beam coupling impedance enters the equation of motion as a kick

$$\Delta y' = \frac{\Delta v_y}{v} = \frac{\Delta p_y}{\gamma m v}. \tag{2.31}$$

The application of such a kick at z_0, i.e. $y'(z_0) \rightarrow y'(z_0) + \Delta y'$, increases the particle amplitude $\sqrt{\epsilon}$ by $\Delta y' \sqrt{\beta(z_0)}$ as visible from (cf. Eq. 2.21)

$$y'(z) = \sqrt{\frac{\epsilon}{\beta(z)}} \left(\frac{\beta'(z)}{2} \cos(\psi(z) + \psi_0) - \sin(\psi(z) + \psi_0) \right), \tag{2.32}$$

where for the constant focusing approximation the $\beta'(z)$ term can be dropped. Moreover, the origin of impedance kicks, which is the coherent displacement $\overline{y}(z_0)$ resulting in a dipole moment, also depends linearly on $\sqrt{\beta_x(z_0)}$ as visible from Eq. 2.21. Thus, when summing up impedance kicks, the sum has to be weighted linearly with the local betafunction.

Returning to a description that depends only on time t, the kick can be seen as a continuous force, i.e.

$$F_y(t) = \partial_t p_y = p_y'(t) v = \gamma m v^2 y''(t) \tag{2.33}$$

which is employed as a right hand side to the averaged Eq. 2.29. Subsequently, the driven harmonic oscillator equation reads

$$\boxed{\partial_t^2 y(t) + \omega_{\beta,y}^2 y(t) = \frac{F_y(t)}{m\gamma},} \tag{2.34}$$

where the excitation has to be weighted with the local betatron amplitude function as

$$\boxed{F_y(t) = \frac{1}{C\hat{\beta}_x} \oint \beta_y(z) F_y(t,z) dz \approx \frac{1}{C\hat{\beta}_y} \sum_i \beta_y(z_i) F_y(t,z_i) \Delta z_i} \tag{2.35}$$

with

$$\frac{1}{\hat{\beta}_y} = 2\pi\frac{Q_y}{C} = \frac{1}{C}\oint\frac{\mathrm{d}s}{\beta_y(z)} \quad\text{and}\quad \sum_{\mathrm{i}}\Delta \mathrm{z}_{\mathrm{i}} = \mathrm{C}. \tag{2.36}$$

The equation of motion, Eq. 2.34, is written only for a single particle. We will now look at the coherent motion

$$\overline{y} = \frac{1}{N}\sum_{i=1}^{N} y_i. \tag{2.37}$$

The transverse force can be linearized for small incoherent and coherent displacement as depicted in Fig. 2.3 as

$$F \approx F_0 + y\frac{\partial F}{\partial y} + \overline{y}\frac{\partial F}{\partial \overline{y}}, \tag{2.38}$$

where the constant term F_0 only leads to a constant closed orbit displacement and is therefore neglected. The incoherent and coherent tune shifts change the tune according to $Q_i = Q_{0,i} + \Delta Q_i$ and $Q_{\mathrm{coh}} = Q_0 + \Delta Q_{\mathrm{coh}}$, respectively. They can be found from the equations

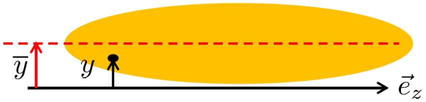

Figure 2.3.: Illustration of coherent and incoherent displacement.

$$\partial_t^2 y_i + \omega_0^2 Q_{0,i}^2 y_i = \frac{1}{m\gamma} y_i \frac{\partial F}{\partial y_i} \tag{2.39a}$$

$$\partial_t^2 \overline{y} + \omega_0^2 Q_0^2 \overline{y} = \frac{1}{m\gamma}\overline{\left(y_i\frac{\partial F}{\partial y_i} + \overline{y}\frac{\partial F}{\partial \overline{y}}\right)} \tag{2.39b}$$

with $Q^2 \approx Q_0^2 + 2Q_0\Delta Q$ as

$$\Delta Q_i = \frac{1}{2Q_{0,i}\omega_{0,i}^2 m\gamma}\frac{\partial F}{\partial y_i} \tag{2.40a}$$

$$\Delta Q_{\mathrm{coh}} = \frac{1}{2Q_0\omega_0^2 m\gamma}\left(\frac{\partial F}{\partial y} + \frac{\partial F}{\partial \overline{y}}\right). \tag{2.40b}$$

Here, $\partial F/\partial y$ is the derivative of the force w.r.t. the coordinate of a test particle at the design trajectory, see Fig. 2.3. In the presence of beam or chamber asymmetries this incoherent force does not average to zero in the coherent tune shift. As it depends linearly on the offset of an individual particle from the design trajectory, it is usually referred to as quadrupolar or detuning term. However, in a convex chamber, which is not extremely flat, the average of this force is rather small [36]. The two forces causing ΔQ_{coh} is what we will later express by the transverse wake potential or beam coupling impedance.

The acceleration process in a synchrotron is closely related to the longitudinal dynamics, i.e. the synchrotron motion. Since the cavity applies a kick on the particles each turn, the equations of motion should be difference-equations. However, since the longitudinal motion (w.r.t. s) is slow compared to the beam revolution, the difference-equations can be well approximated by differential equations [11]. This requires to calculate differentials of some quantities that change only slightly, e.g.[10]

$$\frac{\Delta C}{C} = \frac{\Delta T}{T_0} + \frac{\Delta v}{v_0}, \qquad \frac{\Delta E}{E_0} = \beta_0^2 \frac{\Delta p}{p_0}, \qquad \frac{\Delta v}{v_0} = \frac{\Delta \beta}{\beta_0} = \frac{1}{\gamma_0^2}\frac{\Delta p}{p_0}. \tag{2.41}$$

Due to the dispersion, the length of the particle orbit C changes with the momentum as

$$\frac{\Delta C}{C} = \alpha \frac{\Delta p}{p_0}, \tag{2.42}$$

where the momentum compaction factor α or the transition energy $\gamma_{\text{t}} mc^2$ is a constant lattice property and can be computed by [1]

$$\frac{1}{\gamma_{\text{t}}^2} := \alpha = \frac{1}{C} \oint \frac{D(z)}{R(z)} \mathrm{d}z. \tag{2.43}$$

The phase-slip factor $\eta := \gamma_{\text{t}}^{-2} - \gamma^{-2}$ connects the revolution period with the momentum offset as

$$\frac{\Delta T}{T_0} = -\frac{\Delta \omega}{\omega_0} = \eta \frac{\Delta p}{p_0}. \tag{2.44}$$

Note that η changes the sign, when the energy crosses γ_t during acceleration. Since this requires an RF-phase jump of 180°, most synchrotrons avoid transition energy crossing by appropriate design of the dispersion in the lattice.

The phase deviation $\Delta\varphi$ can be related to arrival time offset ΔT or spatial position offset s by

$$\Delta \varphi = \omega_{RF} \Delta T = \frac{2\pi h}{C} s, \tag{2.45a}$$

---

[10] The first equation is trivial, the second and third are readily found from Eqs. 1.2 and 2.5.

where ω_{RF} is the RF-cavity angular frequency and $h = \omega_{RF}/\omega_0$ is the (integer) harmonic number. Finally, we have all the means to describe the synchrotron motion within the RF-potential well as (see e.g. [1] p. 180)

$$\partial_t \Delta E = \frac{q}{T_0} \left[U_0 (\sin(\varphi_0 + \Delta\varphi) - \sin\varphi_0) \right] \tag{2.46a}$$

$$\partial_t \Delta\varphi = \frac{2\pi h \eta}{\beta^2 T_0 E_0} \Delta E. \tag{2.46b}$$

Note that these equations are the same as the ones for the mathematical pendulum. If the synchronous phase angle φ_0 is set to zero, no acceleration takes place, however there is still longitudinal focusing (stationary bucket). An acceleration is obtained for $\varphi_0 \neq 0$ and among other quantities the magnetic field strength has to be retraced according to Eq. 1.5.

In case of energy loss due to a wake potential $U_{\text{wake}}(\Delta\varphi)$, this (negative) potential has to be added to the energy gain due to the RF-voltage. The second order equation supplemented with such a wake potential reads

$$\boxed{\partial_t^2 \Delta\varphi = \frac{2\pi h \eta}{\beta^2 T_0^2 E_0} [\underbrace{U_0 (\sin(\varphi_0 + \Delta\varphi) - \sin\varphi_0)}_{\approx U_0 \cos\varphi_0 \Delta\varphi} + U_{\text{wake}}(\Delta\varphi)].} \tag{2.47}$$

For simplicity we consider only small amplitudes ($\Delta\varphi \ll 1$) for which Eq. 2.47 can be linearized and the synchrotron frequency reads

$$\omega_s^2 = -\frac{2\pi h \eta}{\beta^2 T_0^2 E_0} q U_0 \cos\varphi_0. \tag{2.48}$$

In order to have a stable oscillation, i.e. longitudinal focusing, the synchrotron frequency must be real valued. Thus, for positive η, i.e. $\gamma > \gamma_t$, $\cos\varphi_0 < 0$ must hold. Contrarily, for negative η, i.e. $\gamma < \gamma_t$, $\cos\varphi_0 > 0$ is required. The electric potential $U_{\text{wake}}(\Delta\varphi)$ is dependent on the beam distribution and intensity, and will be expressed by the wake potential or beam coupling impedance in the next section.

2.4 Wake Functions

The wake function is a Green's function that describes how a single source charge q_1 applies a force on a test charge q_2, both directly and indirectly by interference with the (lossy) wall, see Fig. 2.4. The relevant quantity for both beam dynamics and heat load considerations is the integrated force, i.e. the energy or momentum change, rather than at the instantaneous values. This integrated force depends neither on time, nor on the longitudinal position, but only on the relative distance s between q_1 and q_2 and their transverse positions. Usually one makes two assumptions that decouple the equations

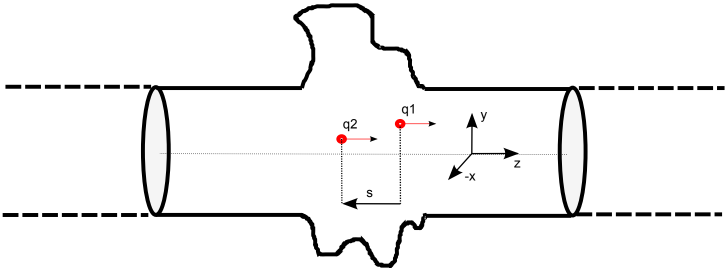

Figure 2.4.: Longitudinal cut through an accelerator structure and centered coordinate system. The charge q_1 is usually referred to as source or leading charge and q_2 is referred to as test or trailing charge.

of motion from electromagnetics (cf. Fig. 2.1b):

1. **Rigid Beam Approximation:** Although the leading charge loses energy, its velocity remains unchanged. This is exactly fulfilled for an ultrarelativistic beam which carries infinite energy.

2. **Kick Approximation:** The wake force continuously acting on the trailing charge is lumped in a single kick *after* the passage through the device. This means that the trailing charge is also assumed to be rigid during the passage.

These approximations are justified by the different time scales of the particle passage (fast) and the evolution of wake field effects (slow). We define the wake function as (see also e.g. [37, 38])

$$\begin{aligned} \vec{W}(\vec{r}_2^{\perp}, \vec{r}_1^{\perp}, s) &:= \frac{1}{q_1 q_2} \int_{-\infty}^{\infty} \vec{F}\left(\vec{r}_2, z_2, t = \frac{z_2 + s}{v}\right) \mathrm{d}z_2 \\ &= \frac{1}{q_1} \int_{-\infty}^{\infty} \left[\vec{E} + \vec{v} \times \vec{B}\right]\left(\vec{r}_2, z_2, t = \frac{z_2 + s}{v}\right) \mathrm{d}z_2, \end{aligned} \tag{2.49}$$

such that a positive value indicates momentum or energy gain for the test charge. The integral 2.49 exists only if the assumed infinitely long pipe connections (see Fig. 2.4) do not cause any wakefields, which requires the following conditions:

- Smooth pipe (no geometric wakefields)
- Perfectly conducting pipe (no resistive wakefields)
- Ultrarelativistic beam (no space charge wakefields)

When all these conditions are fulfilled, the infinite integration in Eq. 2.49 can be replaced by a finite one, since the scattered fields from the 3D region decay in the pipe

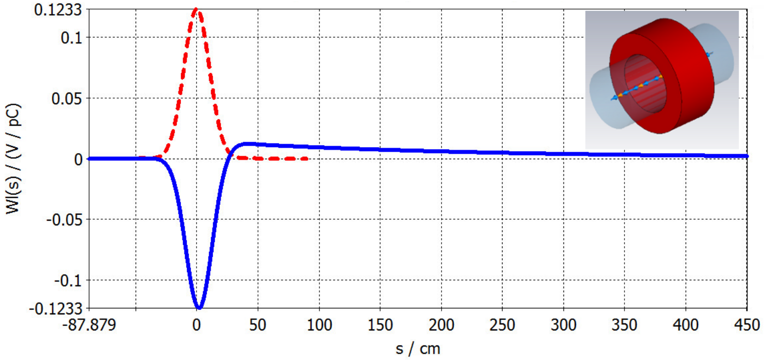

Figure 2.5.: Example longitudinal wake potential for a ferrite ring obtained by CST Particle Studio® [40] (PS). Such a non-oscillating wake corresponds to a broadband impedance. The dashed red line denotes the excitation bunch shape in arbitrary units (bunch length $\sigma_s = 10\,\text{cm}$, $\beta = 1$).

below the waveguide cutoff frequency. Above the cutoff frequency, waveguide modes do not interact with the particle beam in average, since the fields are periodic and $v_{\text{beam}} \leq c < v_{\text{phase}}^{\text{mode}}$. An estimate of the decay length for a given threshold can be found in [17]. For non-ultrarelativistic velocity, sophisticated boundary conditions are required for the entry and exit of the beam in a finite-sized computational domain, see [39]. In order to ensure that the integral 2.49 is finite, even if the third assumption is not fulfilled, the integration can be performed over a finite length and the space charge interaction in the infinitely long pipe can be described by a space charge wake function per length.

The wake potential describes the wake force acting on the test particle q_2 due to the whole beam. Since $\vec{W}(s)$ is a Green's function, the wake potential can be obtained by a convolution with the beam distribution,

$$\vec{W}_{\text{pot}}(\vec{r}_1^{\perp},\vec{r}_2^{\perp},s) = \iiint \vec{W}(\vec{r}_2^{\perp},\vec{r}_1^{\perp\prime},s')\lambda(s-s')\sigma(\vec{r}_1^{\perp}-\vec{r}_1^{\perp\prime})\mathrm{d}s'\mathrm{d}^2\vec{r}_1^{\perp\prime} \tag{2.50}$$

where $\sigma(\vec{r}^{\perp})$ is the normalized transverse density and $\lambda(s)$ is the normalized longitudinal density such that the source charge density is $\varrho_s(\vec{r}) = q_{\text{total}}\sigma(\vec{r}^{\perp})\lambda(s)$. An example wake potential for a dispersive ferrite ring, computed by CST Particle Studio® [40] (PS), is plotted in Fig. 2.5. The wake potential is the (lumped) momentum change ('kick') the trailing particle q_2 receives due to passing the structure at relative distance s to the beam,

$$\Delta\vec{p}_2(\vec{r}_2^{\perp},s) = \frac{q_{\text{total}}q_2}{v}\vec{W}_{\text{pot}}(\vec{r}_2^{\perp},s). \tag{2.51}$$

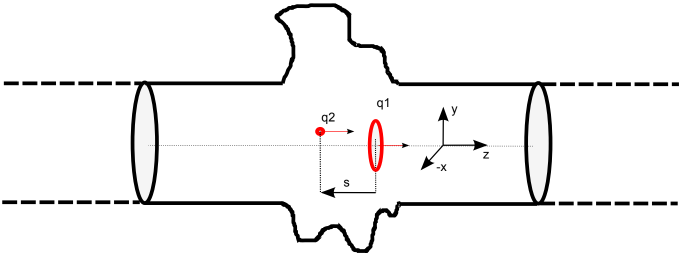

Figure 2.6.: Replacement of the source particle by a transversely uniform beam.

The longitudinal wake potential provides the voltage to be added to the RF-voltage in Eq. 2.47,

$$U_{\text{wake}}(s) = q_{\text{total}} W_{\text{pot},||}(s), \tag{2.52}$$

the so-called potential well distortion. This means, that the total potential well, which determines the bunch shape, depends on the bunch shape itself and on the intensity. A self-consistent bunch distribution can be found for a given wake function, beam intensity, and RF-potential by solving Haissinski's integral equation [41] (see also [42], Eq 2.57), which is, however, beyond the scope of this thesis.

A coherent oscillation of a transversely uniform circular beam of radius a can be written as

$$\sigma(\vec{r}^{\perp}) = \frac{1}{\pi a^2} \Theta(a - |\vec{r}^{\perp} - \vec{d}|), \tag{2.53}$$

where $\vec{d}$ is the transverse displacement vector and Θ denotes the Heaviside step function. This displacement can be approximated in polar coordinates ϱ, φ by [43]

$$\sigma(\varrho, \varphi) \approx \frac{1}{\pi a^2} (\Theta(a - \varrho) + \delta(a - \varrho)(d_{\text{x}} \cos\varphi + d_{\text{y}} \sin\varphi) + \ldots) \tag{2.54}$$

as illustrated in Fig. 2.7. Equation 2.54 cannot be seen as a Taylor expansion, since the distributions do not form a metric space, but from both Eqs. 2.53 and 2.54 the moments

$$M_{m,n} = \int \sigma x^m y^n \mathrm{d}A, \tag{2.55}$$

where $m, n \in \mathbb{N}_0$, can be determined, equated, and in this way the expansion coefficients can be calculated. Such an expansion is independent of the reference radius a, but it requires distributional derivatives[11] for $m, n > 1$. Therefore it is convenient only up to the first order, i.e. the dipole moment.

---

[11] Derivatives of the δ-distribution in Eq. 2.54 can be shifted by $m-1$ partial integrations in Eq. 2.55.

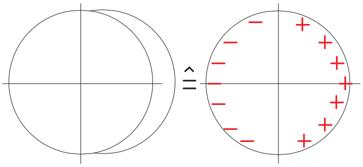

Figure 2.7.: Illustration of a coherent transverse oscillation represented by a dipole moment according to Eq. 2.53 (left) and Eq. 2.54 (right).

Usually, for the coherent beam dynamics, only $m, n \in \{0, 1\}$ play a role in the source term. The relevant multipoles for the test charge are discussed in App. A. Generally, the transverse wake function can be defined for a pencil beam as linearized w.r.t. the source and test charge offset (cf. Fig. 2.3),

$$W_{\perp,x}^{\text{drive}}(s) = \frac{1}{q_1 d_{x_1}} \int_{-\infty}^{\infty} \left[\vec{E} + \vec{v} \times \vec{B}\right]\left(\vec{r}_2^{\perp} = 0, z, \frac{z_2 + s}{v}\right) \mathrm{d}z_2 \tag{2.56}$$

$$W_{\perp,x}^{\text{det}}(s) = \frac{1}{q_1 d_{x_2}} \int_{-\infty}^{\infty} \left[\vec{E} + \vec{v} \times \vec{B}\right]\left(\vec{r}_2^{\perp} = d_{x_2}\vec{e}_x, z, \frac{z_2 + s}{v}\right) \mathrm{d}z_2. \tag{2.57}$$

The dipolar or driving wake acts coherently, since the force experienced by a test charge does not depend on the test charge's position in a dipole field. Contrarily, the detuning wake acts incoherently, as it depends on the displacement of the test charge linearly. The transverse force acting on a slice of the beam at relative position s originating from the whole beam is

$$\frac{\partial F}{\partial \overline{x}}(s) = \frac{q_{\text{slice}}(s) q_{\text{total}}}{C} \int_{-C/2}^{C/2} W_{\perp}^{\text{drive}}(s') \lambda(s - s') \mathrm{d}s' \tag{2.58a}$$

$$\frac{\partial F}{\partial x}(s) = \frac{q_{\text{slice}}(s) q_{\text{total}}}{C} \int_{-C/2}^{C/2} W_{\perp}^{\text{det}}(s') \lambda(s - s') \mathrm{d}s', \tag{2.58b}$$

where the slice charge is $q_{\text{slice}} = q_{\text{total}} \lambda(s)$. The expressions 2.58 can be inserted into Eq. 2.40a to obtain the corresponding coherent tune shift for each slice.

2.5 Beam Coupling Impedance

The beam coupling impedance is defined as the Fourier transform of the wake function,

$$\underline{\vec{Z}}(\vec{r}_1^{\perp}, \vec{r}_2^{\perp}, \omega) = -\int_{-\infty}^{\infty} \vec{W}(\vec{r}_1^{\perp}, \vec{r}_2^{\perp}, s) e^{-i\omega s/v} \frac{\mathrm{d}s}{v}. \tag{2.59}$$

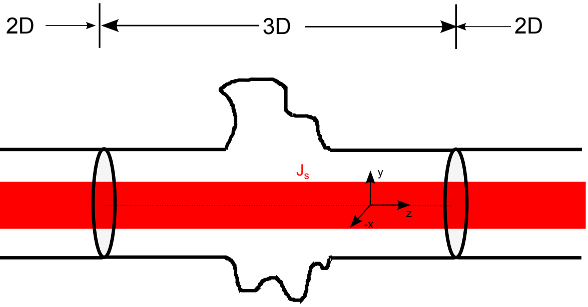

Figure 2.8.: Visualization of the longitudinal de-localization of source and witness particles in the frequency domain and 2D/3D split.

Since a positive wake indicates energy gain of the test particle, the minus sign is required to comply with the engineering convention of positive resistance indicating energy loss. The real valued wake function implies for the impedance

$$\underline{\vec{Z}}(-\omega) = \underline{\vec{Z}}^*(\omega), \tag{2.60}$$

i.e., it is sufficient to determine the impedance for positive frequencies only.

Using the spectrum of the force $\underline{F}(z,\omega) = \mathscr{F}\{F(z,t)\}(z,\omega)$, Eq. 2.59 can be rewritten by inserting Eq. 2.49 as

$$\underline{\vec{Z}}(\vec{r}_1^{\perp}, \vec{r}_2^{\perp}, \omega) = -\frac{1}{q_1 q_2} \int_{-\infty}^{\infty} \underline{\vec{F}}(\vec{r}_1^{\perp}, \vec{r}_2^{\perp}, z, \omega) e^{+i\omega z/v} \mathrm{d}z, \tag{2.61}$$

where one should note that the integral is not a Fourier transform, but the wake integration in the frequency domain.

In the same manner as in the TD, the wake integration length can be restricted to a finite value l, such that the integral reads

$$\underline{\vec{Z}}(\vec{r}_1^{\perp}, \vec{r}_2^{\perp}, \omega) = -\frac{1}{q_1 q_2} \int_{-l/2}^{l/2} \underline{\vec{F}}(\vec{r}_1^{\perp}, \vec{r}_2^{\perp}, z, \omega) e^{+i\omega z/v} \mathrm{d}z, \tag{2.62}$$

with the assumptions that scattered fields have decayed after $l/2$ and only space charge fields remain. The way how 2D and 3D impedances are split is illustrated in Fig. 2.8.

In the following, the impedance definition will be reformulated, such that it depends only on electromagnetic field quantities in the frequency domain, i.e. spectral densities.

Additionally, a volumetric expression shall be obtained, which will be particularly useful in numerical simulations. First, we recall the current density in the TD,

$$\vec{J}_s(\vec{r}_\perp, z, t) = q_1 \sigma(\vec{r}_\perp)\delta(z - vt)\vec{v} \tag{2.63}$$

which is transformed as

$$\underline{\vec{J}}_s(\vec{r}_\perp, z, \omega) = q_1 \sigma(\vec{r}_\perp) e^{-i\omega z/v}\vec{e}_z. \tag{2.64}$$

The source particle is de-localized in the FD, as illustrated in Fig. 2.8. The longitudinal impedance for a witness particle of such a beam is found from the product (convolution in TD) of Eq. 2.62 with σ, i.e.

$$\underline{\vec{Z}}(\omega, \vec{r}_2^{\perp}) = -\frac{1}{q_1 q_2}\int_{\text{beam}} \underline{\vec{F}}(\vec{r}_1^{\perp}, \vec{r}_2^{\perp}, z, \omega) e^{i\omega z/v}\sigma(\vec{r}_1^{\perp})\mathrm{d}r_1^{\perp}\mathrm{d}z. \tag{2.65}$$

Moreover, assuming that the beam experiences the impedance coherently, one can define more generally

$$\boxed{\underline{Z}_{\parallel}(\omega) = -\frac{1}{q^2}\int_{\text{beam}} \underline{\vec{E}}\cdot\underline{\vec{J}}_s^{*}\mathrm{d}V.} \tag{2.66}$$

The transverse impedance is found in a similar way from the transverse components of Eq. 2.62. At first, we look only at dipolar impedances, defined as the force acting on q_2, normalized by the source dipole moment $q_1 d_x$

$$\underline{Z}_{\perp,x}(\omega, \vec{r}_2) = -\frac{(-i)}{q_1 d_x}\int_{-l/2}^{l/2}\left[\underline{\vec{E}}(\omega) + \vec{v}\times\underline{\vec{B}}(\omega)\right]_x e^{i\omega z/v}\mathrm{d}z. \tag{2.67}$$

The $(-i)$ in the definition is put by convention, in order to relate the real part to growth and the imaginary part to phase shift in stability considerations, as it is the case for the longitudinal impedance. For negative frequencies, this implies $\underline{Z}_{\perp}(-\omega) = -\underline{Z}_{\perp}^{*}(\omega)$. With Faraday's law (Eq. 2.15a), Eq. 2.67 can be written as

$$\begin{aligned}\underline{Z}_{\perp,x}(\omega) &= \frac{i}{q d_x}\int_{-l/2}^{l/2}\left[\underline{E}_x + \frac{v}{i\omega}\left(\frac{\partial \underline{E}_x}{\partial z} - \frac{\partial \underline{E}_z}{\partial x}\right)\right]e^{i\omega z/v}\mathrm{d}z \\ &= -\frac{v}{q d_x \omega}\left[\int_{-l/2}^{l/2}\frac{\partial \underline{E}_z}{\partial x}e^{i\omega z/v}\mathrm{d}z - \left[\underline{E}_x e^{i\omega z/v}\right]_{-l/2}^{l/2}\right],\end{aligned} \tag{2.68}$$

in which the last term was obtained using partial integration, such that the $\underline{E}_x$-term cancels out. This boundary term is supposed to vanish for large l. We finally define with the dipolar part of the source current density

$$\boxed{\underline{Z}_{\perp,x/y}(\omega) = -\frac{v}{\omega(qd_{x/y})^2}\int_{\text{beam}} \underline{\vec{E}}\cdot\underline{\vec{J}}^{*}_{s,d_{x/y}}\,\mathrm{d}V.} \tag{2.69}$$

The reformulation of the transverse impedance as dependent on the longitudinal component of the electric field is usually referred to as Panofsky-Wenzel [44] theorem. It will be proven and discussed in more detail in the next section.

The impedance definitions in Eqs. 2.66 and 2.69 are easy to be seen as the beam's power loss integrals. A more general approach would take arbitrary (different) multipoles for the excitation and evaluation, see App. A. In a circularly symmetric setup, only multipoles of the same order couple and impedances for different excitation and evaluation orders vanish. If the symmetry of the structure is broken, generally all multipoles couple.

2.6 Panofsky-Wenzel Theorem

A connection between the longitudinal and transverse wake force can be established by investigating the curl and divergence of the Lorentz force vector-field due to an arbitrary source charge distribution[12], see also [23]. With Faraday's law we have

$$\nabla\times\vec{F}(\vec{r}_2^{\,\perp},z,t) = -q_2(\partial_t + v\partial_z)\vec{B}(\vec{r}_2^{\,\perp},z,t) = -q_2\frac{\mathrm{d}\vec{B}}{\mathrm{d}t}(\vec{r}_2^{\,\perp},z,t). \tag{2.70}$$

For the wake function or wake potential follows

$$\begin{aligned}\nabla'\times\vec{W}(\vec{r}_2^{\,\perp},s) &= \frac{1}{q_2q_1}\int_{-\infty}^{\infty}\nabla\times\vec{F}(\vec{r}_2^{\,\perp},z,t=(s+z)/v)\mathrm{d}z\\ &= \left[\frac{v}{q_1}\vec{B}(\vec{r}_2^{\,\perp},z,t=(s+z)/v)\right]_{z=-\infty}^{\infty} = 0\end{aligned} \tag{2.71}$$

where the gradient ∇ refers to the absolute position of the test charge and $\nabla' = (\partial_{x_2},\partial_{y_2},-\partial_s)^{\mathrm{T}}$ refers to the relative position of the test charge.

We introduce the split of the curl in longitudinal and transverse components as

$$\nabla\times\vec{f} = \left(\begin{array}{cc|c} 0 & -\partial_z & \partial_y\\ \partial_z & 0 & -\partial_x\\ \hline -\partial_y & \partial_x & 0\end{array}\right)\vec{f} =: \left(\begin{array}{c|c} \hat{\mathrm{Z}} & \hat{\mathrm{A}}\\ \hline \hat{\mathrm{B}} & 0\end{array}\right)\vec{f}. \tag{2.72}$$

---

[12] For simplicity, we keep calling the total source charge q_1 in this section.

The two-dimensional vectorial and scalar curl operators are concatenations of $\hat{\mathrm{A}}_{3\mathrm{D}} = -\vec{e}_z \times \nabla$ and $\hat{\mathrm{B}}_{3\mathrm{D}} = \vec{e}_z \cdot \nabla\times$ and have the property

$$\hat{\mathrm{A}} = \begin{pmatrix} \partial_y \\ -\partial_x \end{pmatrix} = -\hat{\mathrm{B}}^{\mathrm{T}}. \tag{2.73}$$

The operator $\hat{\mathrm{Z}}$ is a concatenation of $\hat{Z}_{3\mathrm{D}} = \partial_z \vec{e}_z \times$ and has the property

$$\hat{\mathrm{Z}}^2 = -\hat{\mathrm{I}}\partial_z^2, \tag{2.74}$$

where $\hat{\mathrm{I}}$ is the identity matrix. With the above notation follows from Eq. 2.71

$$-\partial_s \vec{W}_\perp = \nabla_\perp W_\parallel \tag{2.75}$$

$$\hat{\mathrm{B}}\vec{W}_\perp = 0 \tag{2.76}$$

and finally

Theorem 1 (Panofsky-Wenzel)**.** *The transverse kick on a charged particle can be deduced from the longitudinal one by*

$$\vec{W}_\perp(\vec{r}_2^{\,\perp}, s) = -\int_{-\infty}^{s} \nabla_\perp W_\parallel(\vec{r}_2^{\,\perp}, s')\mathrm{d}s'. \tag{2.77}$$

Moreover, the impedances are related by

$$\frac{\omega}{v}\underline{\vec{Z}}_\perp(\vec{r}_2^{\,\perp}, \omega) = \nabla_\perp \underline{Z}_\parallel(\vec{r}_2^{\,\perp}, \omega). \tag{2.78}$$

Note that the transverse gradient always refers to the position of the test charge.

The divergence of the transverse wake function reads

$$\nabla_\perp \cdot \vec{W}_\perp(\vec{r}_2^{\,\perp}, s) = \nabla' \cdot \vec{W}(\vec{r}_2^{\,\perp}, s) + \partial_s W_\parallel(\vec{r}_2^{\,\perp}, s) \tag{2.79}$$

where the divergence of the 3D wake is

$$\nabla' \cdot \vec{W}(\vec{r}_2^{\,\perp}, s) = \frac{1}{q_1 q_2}\int_{-\infty}^{\infty} \nabla \cdot \vec{F}(\vec{r}_2^{\,\perp}, z, (s+z)/v)\mathrm{d}z. \tag{2.80}$$

The divergence of the force is found with Faraday's and Gauss' law as

$$\nabla \cdot \vec{F} = \frac{q_2 \varrho_s(\vec{r}_2^{\,\perp}, z, (s+z)/v)}{\varepsilon_0 \gamma^2} - q_2 \beta^2 \partial_s E_z(\vec{r}_2^{\,\perp}, z, (s+z)/v), \tag{2.81}$$

where $\varrho_s(\vec{r}_2^{\perp}, z, (s+z)/v)$ denotes the source charge density at the position of the test charge. Applying the transverse divergence to Eq. 2.75 and inserting the last three equations successively one finds

Theorem 2 (Wave equation for the longitudinal wake)**.** *The longitudinal wake function satisfies the wave equation*

$$\left[\triangle_\perp + \frac{1}{\gamma^2}\partial_s^2\right] W_\parallel(\vec{r}_2, s) = \frac{1}{\gamma^2 \varepsilon_0 q_1}\partial_s \int_{-\infty}^{\infty} \varrho_s(\vec{r}_2^{\perp}, z, (s+z)/v)\mathrm{d}z. \tag{2.82}$$

Hence, in the ultrarelativistic limit ($\beta \to 1$) holds

$$\triangle_\perp W_\parallel(\vec{r}_2, s) = \triangle_\perp \underline{Z}_\parallel(\vec{r}_2, \omega) = 0. \tag{2.83}$$

Theorem 2 states that only waves with $k_z = \omega/c$ can affect an ultrarelativistic beam, see also an alternative derivation in [37].

In order to solve Eq. 2.82, boundary conditions are required, which are again wake functions. Therefore, Eq. 2.82 does not provide a technique to avoid solving Maxwell's equations. Nonetheless, together with Theorem 1, it is the basis of several techniques to change the wake integration contour, see e.g. [45, 46, 47, 48, 49], which can reduce the effort in the numerical determination of wake functions significantly.

A direct consequence of both Theorems 1 and 2 is

$$\lim_{\beta \to 1} W_{\perp,x}^{\mathrm{det}}(s) + W_{\perp,y}^{\mathrm{det}}(s) = 0, \tag{2.84}$$

i.e., the detuning wakes in both planes can be described by a single function. Moreover, the detuning wake has a focusing and defocusing effect in the two transverse planes, which motivates the name 'quadrupolar wake'.

Theorem 1 is not convenient to establish a relation between the longitudinal and transverse planes, as the dependence of the longitudinal wake on the transverse position is usually unknown. However, in the ultrarelativistic limit, the longitudinal wake fulfills the Laplace equation, which allows to perform a multipole expansion similar to the one for the magnets without fringe fields. Thus, the transverse wake can be calculated by Theorem 1 from the longitudinal one for each multipole separately, see App. A.

3 Analytical Impedance Calculation in the Frequency Domain

This chapter discusses different formulations and simplifications of Maxwell's equations. The goal is to present methods to calculate beam impedances analytically and to elaborate which formulations are suitable for numerical calculation. Both exact and approximate formalisms are considered.

3.1 Wave Equation and Dispersion Relation

Combining Eqs. 2.15 leads to the curl-curl equation

$$\nabla \times \underline{\nu} \nabla \times \underline{\vec{E}} + i\omega\kappa\underline{\vec{E}} - \omega^2 \varepsilon \underline{\vec{E}} = -i\omega \underline{\vec{J}}_s \tag{3.1}$$

and the continuity equation

$$\nabla \cdot (\underline{\vec{J}}_s + \kappa\underline{\vec{E}}) + i\omega\underline{\varrho}_s = 0. \tag{3.2}$$

We assume that the beam runs only in vacuum, i.e. $\operatorname{supp}\{\kappa\} \cap \operatorname{supp}\{J_s\} = \emptyset$, leading to disjoint continuity equations,

$$\nabla \cdot \underline{\vec{J}}_s + i\omega\underline{\varrho}_s = 0 \tag{3.3a}$$

$$\nabla \cdot \kappa\underline{\vec{E}} = 0. \tag{3.3b}$$

The beam current density is modeled as a convection current density $\underline{\vec{J}}_s = \underline{\varrho}_s v\vec{e}_z$. Therefore, the spatial Fourier correspondence $\partial_z \rightarrow -ik_z$ is given for the source fields (beam in free space) by

$$\boxed{k_z = \frac{\omega}{v}.} \tag{3.4}$$

In a longitudinally homogeneous and smooth 2D structure, this property must hold also for the fields scattered back from the wall.

In 2D structures, fields and finally impedances can be determined by the so-called 'field matching' technique, i.e. assuming $\underline{\mu}, \underline{\varepsilon}$ to be constant in particular subdomains and enforcing the continuity conditions of the electric and magnetic field at the interfaces. For particular structures such as concentric cylinders or parallel plates, the field matching technique can be cast into a matrix formalism, see e.g. [50, 51, 52]. The field matching method can also be generalized to the so-called ‘mode matching’ method in 3D, where the fields of infinitely many modes have to be matched on the subdomain boundaries. Numerical results are obtained by considering a large but finite number of modes. Examples for beam pipe cross-section changes are given in [53] and a cylindrical tube of finite length is presented in [54]. The mode matching method can also be used with numerically calculated eigenmodes, see e.g. [55].

Assuming $\underline{\mu} = \text{const}$ in each particular subdomain and $\underline{\mu} = \mu_0, \underline{\varepsilon} = \varepsilon_0$ where the beam runs, the vector-analytical identity $\nabla \times \nabla \times = \nabla(\nabla\cdot) - \triangle$ transforms Eq. 3.1 into

$$\triangle\underline{\vec{E}} + \frac{\omega^2}{c^2}\underline{\vec{E}} = -i\omega\mu_0\underline{\vec{J}}_s - \frac{1}{\varepsilon_0}\nabla\underline{\varrho}_s \tag{3.5a}$$

$$\triangle\underline{\vec{E}} + \omega^2\underline{\mu}\underline{\varepsilon}\,\underline{\vec{E}} = 0, \tag{3.5b}$$

respectively. The dispersion relation is found from a Bernoulli separation ansatz in Eq. 3.5b as

$$\boxed{k_\perp^2 + k_z^2 = \omega^2\underline{\mu}\underline{\varepsilon},} \tag{3.6}$$

which holds true in each subdomain with constant $\underline{\mu}$ and $\underline{\varepsilon}$. Restricting Eqs. 3.5 to 2D, i.e. $\triangle = \triangle_\perp - \omega^2/v^2$ and invoking only conductive and vacuum domains, the Helmholtz equation for the z-component reads

$$\left(\triangle_\perp - \frac{\omega^2}{\beta^2\gamma^2c^2} - i\omega\mu_0\kappa\right)\underline{E}_z = \frac{i\omega\mu_0}{\beta^2\gamma^2}\underline{J}_{s,z}. \tag{3.7}$$

Note the similarity of Eq. 3.7 and Eq. 2.82 in Theorem 2 and also $\triangle_\perp\underline{E}_z = 0$ in the ultrarelativistic limit in vacuum domains.

Returning to the full 3D six-component fields, function spaces (here: Sobolev spaces) are introduced, in order define a unique Helmholtz decomposition. Furthermore, it can be advantageous to adapt the language of differential forms, as this becomes relevant in describing mimetic discretizations. A discretization is called mimetic, when it inherits the properties of the continuous fields, such as $\nabla\cdot\nabla\times = 0$. We choose naturally

$$\underline{\Phi}\in\mathscr{H}^1(\Omega), \qquad \underline{\vec{E}},\underline{\vec{H}}\in\mathscr{H}^{\mathrm{curl}}(\Omega), \qquad \underline{\vec{D}},\underline{\vec{J}},\underline{\vec{B}}\in\mathscr{H}^{\mathrm{div}}(\Omega), \qquad \underline{\varrho}_s\in\mathscr{L}^2(\Omega), \tag{3.8}$$

where Ω is a Lipschitz domain. Relevant mathematical details and definitions of the Sobolev spaces are given in App. B. Under certain conditions, it makes sense to regard $\underline{\vec{H}}$ not in $\mathscr{H}^{\mathrm{curl}}(\Omega)$, but in $\tilde{\mathscr{H}}^{\mathrm{curl}}(\Omega)$, which is the dual space of $\mathscr{H}^{\mathrm{div}}(\Omega)$. The dual space is the space of functionals, mapping the functions to the complex numbers. By means of the Riesz representation theorem, these functionals can be constructed from $\mathscr{H}^{\mathrm{div}}(\Omega)$ functions. Similar reasoning applies to $\underline{\vec{D}}$ and $\underline{\vec{J}}$ in $\tilde{\mathscr{H}}^{\mathrm{div}}(\Omega)$, as illustrated in the de-Rham diagram in Fig. 3.1.

$$\begin{tikzcd}
\mathscr{H}^1 \arrow[r, "\nabla"] & \mathscr{H}^{\text{curl}} \arrow[r, "\nabla\times"] \arrow[d, dotted, <->, "\varepsilon"] & \mathscr{H}^{\text{div}} \arrow[r, "\nabla\cdot"] \arrow[d, dotted, <->, "\nu"] & \mathscr{L}^2 \\
\tilde{\mathscr{L}}^2 & \tilde{\mathscr{H}}^{\text{div}} \arrow[l, "\nabla\cdot"'] & \tilde{\mathscr{H}}^{\text{curl}} \arrow[l, "\nabla\times"'] & \tilde{\mathscr{H}}^1 \arrow[l, "\nabla"']
\end{tikzcd}$$

Figure 3.1.: De Rham diagram for the operators relevant for Maxwell's equations.

In this framework, though a bit sloppy, we call something a k-form, when it appears under a k-dimensional integral, e.g. $\underline{\Phi}$ is a 0-form, $\underline{\vec{E}}$ is a 1-form, and $\underline{\varrho}_s$ is a 3-form. For a domain $\Omega \subset \mathbb{R}^n$, the $(n-k)$-forms of the dual space are invertibly mapped to the k-forms of the primal space by Hodge operators, which are for Maxwell's equations the constitutive material relations. This allows to interpret energy or impedance functionals as dual pairings.

In a simply connected domain $\Omega \subset \mathbb{R}^3$, the exterior derivative operators (gradient, curl, divergence) form an exact de-Rham sequence. This means that the image of one exterior derivative operator is the kernel of the next (see Fig. 3.1). Thus, the de-Rham cohomology spaces, i.e. the set difference between the kernel of one and the image of the previous exterior derivative operator, are empty.

The following theorem can be formulated for the Helmholtz split of $\underline{\vec{E}}$ in Eq. 3.1 [1]:

Theorem 3 (Helmholtz decomposition in $\mathscr{H}^{\text{curl}}$)**.** *In a simply connected domain $\Omega \subset \mathbb{R}^3$, any vector field $\underline{\vec{E}} \in \mathscr{H}_0^{\text{curl}}(\Omega)$ can be written as $\underline{\vec{E}} = \underline{\vec{E}}_{\text{curl}} + \underline{\vec{E}}_{\text{div}}$, where $\underline{\vec{E}}_{\text{curl}}$ and $\underline{\vec{E}}_{\text{div}}$ are uniquely determined by demanding $\nabla \times \underline{\vec{E}}_{\text{div}} = 0$ and $\nabla \cdot \underline{\varepsilon}\,\underline{\vec{E}}_{\text{curl}} = 0$ for a piecewise smooth non-vanishing function $\underline{\varepsilon} : \Omega \to \mathbb{C}$.*

Proof. See [56], p.86. The demand of Dirichlet boundary conditions ($\mathscr{H}_0^{\text{curl}}$) can be somewhat relaxed by allowing integrable impedance boundary conditions. A demonstrative explicit calculation of $\underline{\vec{E}}_{\text{div}}$ and $\underline{\vec{E}}_{\text{curl}}$ as function of $\underline{\vec{E}}$ for constant $\underline{\varepsilon}$ can be found in [57]. ☐

If the domain Ω is not simply connected, the Helmholtz decomposition has to be generalized to the so-called Hodge decomposition, i.e. a third field will become constituent of $\underline{\vec{E}}$. This so-called harmonic field[2] satisfies both $\nabla \times \underline{\vec{E}}_{\text{harm}} = 0$ and $\nabla \cdot \underline{\varepsilon}\,\underline{\vec{E}}_{\text{harm}} = 0$ and is yet nonzero, see e.g. [58]. Note that in this case the de-Rham cohomology spaces are not empty anymore.

By applying Theorem 3 with $\underline{\vec{E}}_{\text{div}} = -\nabla\underline{\Phi}$ to Eq. 3.1, the two consecutive PDEs are obtained

$$-\nabla \cdot \underline{\varepsilon} \nabla \underline{\Phi} = \underline{\varrho}_s \tag{3.9a}$$

$$\nabla \times \underline{\nu} \nabla \times \underline{\vec{E}}_{\text{curl}} - \omega^2 \underline{\varepsilon}\, \underline{\vec{E}}_{\text{curl}} = \underline{\vec{R}}, \tag{3.9b}$$

---

[1] A similar theorem can be formulated in $\mathscr{H}_0^{\text{div}}$.

[2] From $\nabla \times \underline{\vec{E}}_{\text{harm}} = 0$ and $\nabla \cdot \underline{\vec{E}}_{\text{harm}} = 0$ follows $\Delta \underline{\vec{E}}_{\text{harm}} = 0$.

where $\underline{\varrho}_s = (i/\omega)\nabla \cdot \vec{\underline{J}}_s$ and

$$\vec{\underline{R}} = -\omega^2 \underline{\varepsilon} \nabla \underline{\Phi} - i\omega \vec{\underline{J}}_{s,z} \vec{e}_z. \tag{3.10}$$

Crucial is here, that $\nabla \cdot \vec{\underline{R}} = 0$ holds due to the continuity equation, i.e. all vector fields in Eq. 3.9b are divergence free. Moreover, for a beam in z-direction, the charge can be written as $\underline{\varrho}_s = \underline{J}_{s,z}/v$.

3.2 Dispersive Materials

The complex and lossless refraction index and the loss tangents are defined for dispersive materials as (all functions of the frequency)

$$\underline{n} = \sqrt{\underline{\mu}_r \underline{\varepsilon}_r}, \quad n_{\text{ll}} = \sqrt{\mu_r' \varepsilon_r'}, \quad \tan\delta_\mu = \frac{\mu_r''}{\mu_r'} \quad \text{and} \quad \tan\delta_\varepsilon = \frac{\varepsilon_r'' + \kappa/\omega\varepsilon_0}{\varepsilon_r'}. \tag{3.11}$$

This allows to rewrite the dispersion relation, Eq. 3.6, in the 2D case as

$$k_\perp^2 = \frac{\omega^2}{c^2}\left[n_{\text{ll}}^2(1 - \tan\delta_\mu \tan\delta_\varepsilon) - \frac{1}{\beta^2} - i n_{\text{ll}}^2(\tan\delta_\mu + \tan\delta_\varepsilon)\right], \tag{3.12}$$

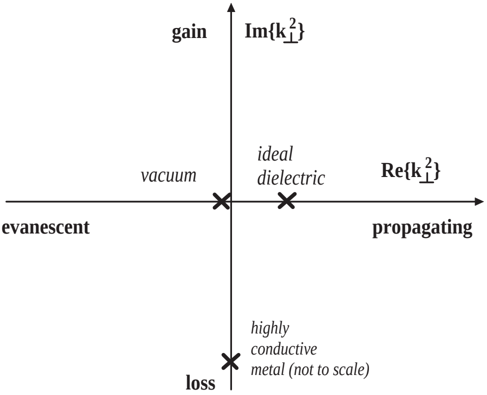

Figure 3.2.: Complex $k_\perp^2$ plane. The vertical axis represents the Cherenkov condition and the horizontal axis separates passive and active materials or devices [59].

where in most cases the product of the two tangents can be neglected[3]. For metals with frequency independent conductivity[4] Eq. 3.12 reads

$$k_\perp^2 = \frac{\omega^2}{c^2}\left[-\frac{1}{\beta^2\gamma^2} - i\frac{\kappa}{\omega\varepsilon_0}\right], \tag{3.13}$$

where one observes that the real part is small compared to the imaginary one, unless β is very small. Figure 3.2 shows the different regimes of $k_\perp^2$ in the complex plane. The vertical axis separates propagating from evanescent waves by the Cherenkov condition

$$\beta n_{\text{II}} > 1. \tag{3.14}$$

The horizontal axis separates energy gain and energy loss, i.e. in passive systems the upper half plane is forbidden. Equation 3.12 allows particular conclusions on the mesh requirements in a 2D simulation, i.e. the mesh size depends only on β, if β is very small, otherwise it depends only on the frequency and the material distribution.

3.2.1 Ferrites

Magnetic composition materials such as non-conductive ferrites or conductive Magnetic Alloy (MA) materials do usually not follow a simple analytical dispersion relation. Nonetheless, one can model the material with a complex permeability, which is determined as a function of the frequency by measurement.

Figure 3.3 shows the modeling of the small signal permeability and the frequency dependent material parameters as provided by the manufacturer. The power loss density is obtained from the complex permeability $\underline{\mu} = \mu' - i\mu''$ as

$$p_{\text{loss}}(\omega) = \frac{1}{T}\int_T B(t)\mathrm{d}H(t) = \frac{1}{2}\omega\mu''(\omega)H_0^2, \tag{3.15}$$

where H_0 is the magnetic field amplitude and $T = 2\pi/\omega$. In this way, the ellipse in Fig. 3.3 can be seen as the linearized hysteresis loop. From the complex permeability one can determine the transverse wave number and draw plots as outlined in Fig. 3.2, see Fig. 3.4.

The data provided by the manufacturer's datasheet for ferrite materials is usually specified under restrictive assumptions. These are in particular the linearization at zero bias field, the neglect of remanence fields and the assumption of isotropy. Furthermore, permeability curves over frequency are given only at room temperature or for heated ferrite and they usually contain a 20% error range. For the determination of beam cou-

---

[3] Exceptions are materials with both conductive and magnetic loss, e.g. Magnetic Alloys (MA).

[4] This assumption is justified for frequencies below the inverse of the Drude-model [60] relaxation time constant $\tau_f = \kappa_{\text{DC}}/(\varepsilon_0\omega_p^2) \sim 10^{-15}$ s (angular plasma frequency ω_p).

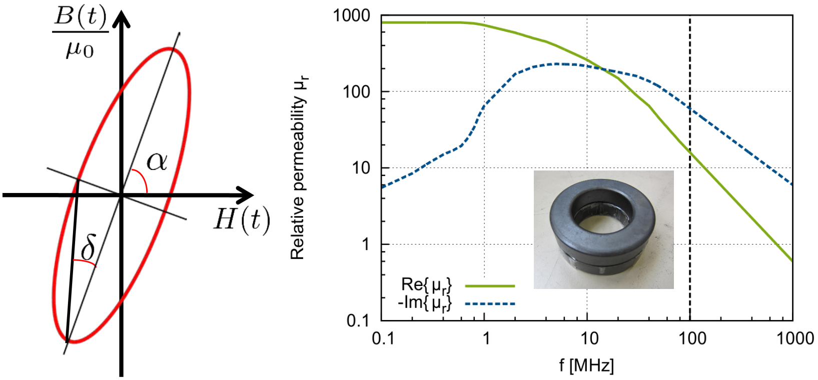

Figure 3.3.: Linear approximation of the lossy hysteresis loop and frequency dependent material parameters for ferrite 'Amidon material 43' [61]. The angles are $\tan\alpha = \mu_r'$ and $\tan\delta = \mu_r''/\mu_r'$. Since manufacturer's data were only available below 100 MHz a power law extrapolation with $\mu_r' \propto f^{-1.43}$ and $\mu_r'' \propto f^{-1.0}$ was performed above [59]. The permittivity of such ferrites is roughly $\varepsilon_r \approx 10$ and the conductivity can be neglected.

pling impedances from ferrite components, the manufacturer's data are suitable within the specified frequency range, which reaches up to 0.1 or 1 GHz. At higher frequencies, sample measurements are required. Methods for such are presented by Barry [62], Caspers *et al.* [63], and Völlinger *et al.* [64] using coaxial or stripline techniques. A

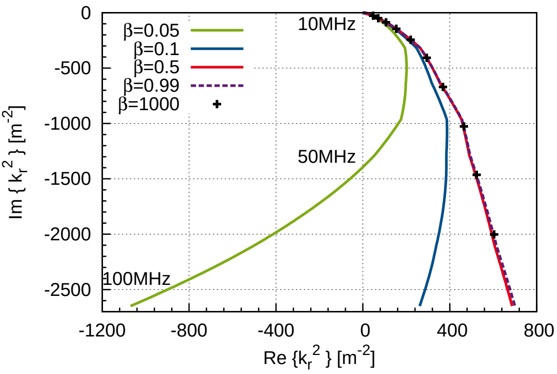

Figure 3.4.: Transverse wavenumber for the ferrite material shown in Fig. 3.3, for different relativistic velocities β and radial model ($\beta = 1000$) [59].

detailed treatise about ferrite data measurements for power converter applications at low and medium frequencies is given in [65].

Another field where more accurate ferrite data are required is eigenmode calculation for tunable ferrite accelerator cavities, see e.g. [66, 67]. The tensorial permeability under strong DC magnetic bias fields is usually not provided by the manufacturer. For parallel bias, measurements have been conducted up to 5 MHz (20 MHz with lower accuracy requirement) in the framework of this thesis, see [68]. For perpendicular bias, measurements can be found in [69] up to 100 MHz.

3.2.2 Wave Length and Penetration Depth

From solving the wave equation for a plane wave impinging perpendicularly on a half space one finds the wave length and penetration depth in the material as

$$\lambda_{\mathrm{s}} = \frac{1}{\operatorname{Im}\left\{i\omega\sqrt{\underline{\mu}\,\underline{\varepsilon}}\right\}} \quad \text{and} \quad \delta_{\mathrm{s}} = \frac{1}{\operatorname{Re}\left\{i\omega\sqrt{\underline{\mu}\,\underline{\varepsilon}}\right\}}, \tag{3.16}$$

respectively. At the boundary of the half space holds the Leontovich[5] Surface Impedance Boundary Condition (SIBC) $\vec{n} \times \vec{n} \times \underline{\vec{E}} = \underline{Z}_s \vec{n} \times \underline{\vec{H}}$, where $\vec{n}$ is the normal vector, and the surface impedance reads

$$\underline{Z}_s = \sqrt{\frac{\underline{\mu}}{\underline{\varepsilon}}}. \tag{3.17}$$

The half-space approximation is valid only if the curvature radius[6] of the surface and the wall thickness[7] are much larger than the penetration depth. For smooth metal surfaces this is usually the case and one finds

$$\underline{Z}_s = \frac{1}{\underline{Y}_s} = \frac{1+i}{\sqrt{2}}\sqrt{\frac{\omega\mu}{\kappa}} \quad \text{and} \quad \delta_{\mathrm{s}} = \lambda_{\mathrm{s}} = \sqrt{\frac{2}{\mu\kappa\omega}}, \tag{3.18}$$

where $\varepsilon \ll \kappa/\omega$ has been dropped in the metal.

The SIBC can also be applied for a coated surface. For a metal coating layer (thickness d, permeability μ_1 and conductivity κ_1) on a metal surface (permeability μ_2 and conductivity κ_2), the first order surface impedance can be written as

$$Z_s = \frac{1+i}{\kappa_1 \delta_{s1}} \frac{M^{(+)} e^{ik_{z1}d} + M^{(-)} e^{-ik_{z1}d}}{M^{(+)} e^{ik_{z1}d} - M^{(-)} e^{-ik_{z1}d}}, \tag{3.19}$$

---

[5] See [70] p.11 for more details on the naming.

[6] Otherwise, higher order surface impedance boundary conditions can be applied, see e.g. [70].

[7] Otherwise, impedance transmission conditions can be applied, see e.g. [70, 71].

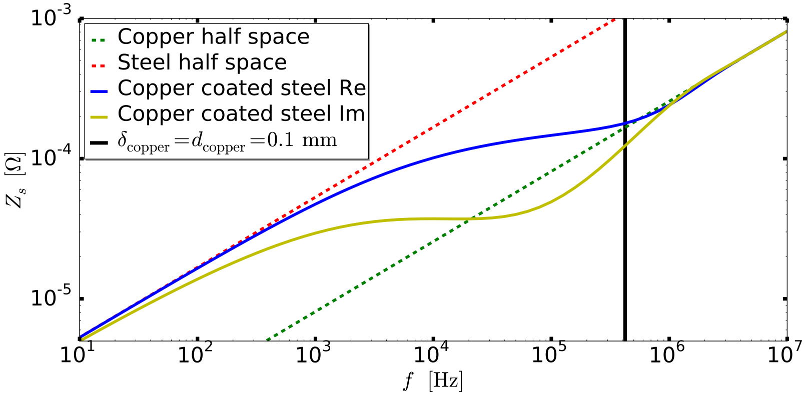

Figure 3.5.: Surface impedance for a thick steel surface, coated by a thin copper layer.

where

$$k_{z1,2} = \frac{1-i}{\delta_{s1,2}}, \quad M^{(+)} = 1 + \sqrt{\frac{\mu_1 \kappa_2}{\mu_2 \kappa_1}}, \quad M^{(-)} = 1 - \sqrt{\frac{\mu_1 \kappa_2}{\mu_2 \kappa_1}}. \tag{3.20}$$

The requirements for the coated boundary condition are the same as for Eq. 3.18, i.e. $d_2 \gg \delta_2$ and $\kappa_1, \kappa_2 \gg \omega\varepsilon$, and the curvature radius should be much larger than the skin depth. Note that there are no requirements on d_1/δ_1. The surface impedance of a copper ($\kappa = 70$MS) coated steel ($\kappa = 1.4$MS) surface is plotted in Fig. 3.5. For frequencies smaller than

$$f_s = \frac{1}{\pi \mu_0 \kappa_1 d^2}, \tag{3.21}$$

i.e. when the skin depth exceeds the coating thickness, the fields can penetrate the copper and create losses in the steel. Thus, the surface impedance approaches the one of the steel half space for lower frequencies asymptotically, i.e. when $\delta_{s,1} \to \infty$.

Finally, we report for a ferrite half space

$$\delta_s = \frac{1}{\frac{\omega}{c}\sqrt{\varepsilon_r |\underline{\mu}_r(\omega)| \sin\frac{1}{2}\delta_\mu(\omega)}}, \tag{3.22}$$

but the requirements for the Leontovich boundary condition are usually not met in practical cases ($f < 1$GHz, $d < 0.1$m).

3.3 Quasi-Stationary Modeling

Consider a domain of size l with an arbitrary piece of material $\mu_\mathrm{d}, \varepsilon_\mathrm{d}, \kappa_\mathrm{d}$ of thickness $d \ll l$, as depicted in Fig. 3.6. The DC surface resistance in units of Ω is[8]

$$z_s = \frac{1}{\kappa_d d} \text{ such that } R_\mathrm{Ohm} = z_s \frac{\text{length}}{\text{width}}. \tag{3.23}$$

The frequency and relaxation-time diagram following Dirks [72] can be seen in Fig. 3.7. This diagram shows the material surface resistance on the horizontal axis and the frequency on the vertical axis. There are limit frequencies for the validity of quasi-stationary approximations which are associated with time constants of the structure and materials. For the wave propagation through the whole domain

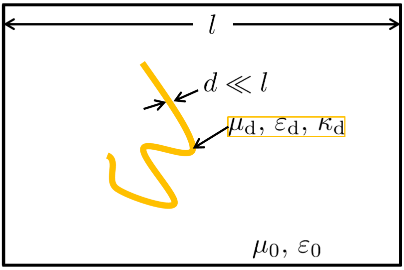

Figure 3.6.: Domain of size l with a material sheet of thickness $d \ll l$ to exemplify quasi stationary approximations.

$$\frac{1}{\omega_\mathrm{em}} = \tau_\mathrm{em} = l\sqrt{\mu_0 \varepsilon_0} \tag{3.24}$$

is the limit frequency. Above this frequency, the wave properties of Maxwell's equations have to be considered and quasi-stationary approximations are invalid. The relaxation of displaced charges happens within the time

$$\frac{1}{\omega_\mathrm{e}} = \tau_\mathrm{e} = \frac{\varepsilon_\mathrm{d}}{\kappa_\mathrm{d}}. \tag{3.25}$$

This is the limit frequency for the Electro-Quasi-Stationary (EQS) approximation. Finally, the magnetic field diffusion through conductive domains has the time constant

$$\frac{1}{\omega_\mathrm{m}} = \tau_\mathrm{m} = \mu_\mathrm{d} \kappa_\mathrm{d} d^2/2, \tag{3.26}$$

---

[8] In engineering it is also common to write Ω/□, where □ is a dimensionless pseudo-unit.

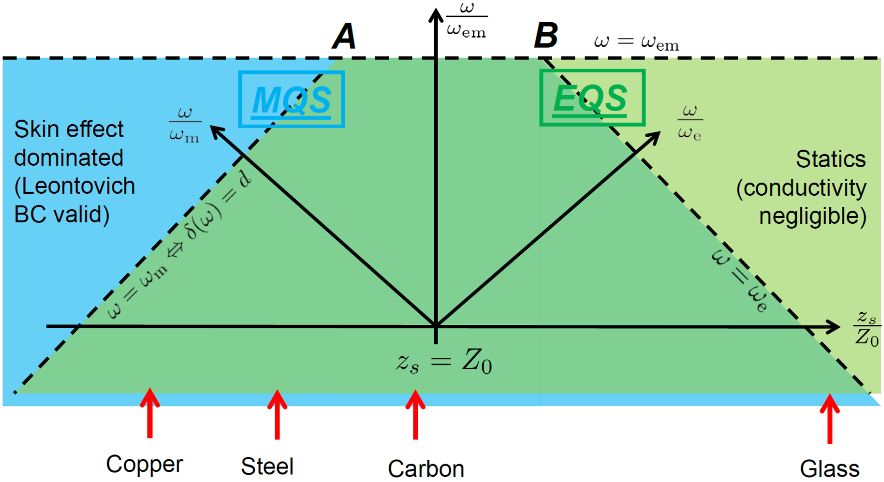

Figure 3.7.: Frequency and material ranges for quasi-stationary approximations in the style of Dirks [72]. All axes are logarithmically scaled.

which determines the limit frequency for the Magneto-Quasi-Stationary (MQS) approximation. The intersection points of the limit frequency lines with the wave propagation limit (see Fig. 3.7) are point A ($\omega_{\mathrm{e}} = \omega_{\mathrm{em}}$),

$$\frac{z_s}{Z_0} = \frac{l}{d\varepsilon_{rd}} \gg 1 \tag{3.27}$$

and point B ($\omega_{\mathrm{m}} = \omega_{\mathrm{em}}$),

$$\frac{z_s}{Z_0} = \frac{\mu_{rd} d}{2l} \ll 1. \tag{3.28}$$

The domains of validity of EQS and MQS are schematically illustrated in Fig. 3.7. Non-dispersive materials would represent straight vertical lines in this plot. Dispersive materials can be illustrated as curves, but the limit frequencies depend on the material parameters which again depend on the frequency. Thus, finding the limiting frequencies becomes a nonlinear problem for dispersive materials.

In the following, standard (EQS / MQS) and advanced (Darwin model / radial model) quasi-stationary models are discussed in order to check their applicability for beam coupling impedance calculation. For simplicity, we assume proper and sufficiently smooth boundary conditions (e.g. PEC), which do not impair the solvability of the system.

3.3.1 Electro- and Magneto-Quasi-Statics

The EQS approximation of Maxwell's equations is obtained by neglecting the induction term in Eq. 2.15a. The system reads

$$\nabla \times \underline{\vec{E}} = 0 \tag{3.29a}$$

$$\nabla \cdot \varepsilon \underline{\vec{E}} = \underline{\varrho}_s \tag{3.29b}$$

$$\nabla \cdot \kappa \underline{\vec{E}} + \nabla \cdot \underline{\vec{J}}_s + i\omega \underline{\varrho}_s = 0, \tag{3.29c}$$

which can be uniquely solved. The substitution $\underline{\vec{E}} = -\nabla \underline{\Phi}$ converts the problem into a complex Poisson equation, which is regular for non-vanishing ε. However, since the EQS can model neither the skin-effect, nor inductances, it is in practice inappropriate for the determination of beam coupling impedance.

The MQS approximation of Maxwell's equations is obtained by neglecting the displacement current in Eq. 2.15b. The system reads

$$\nabla \times \underline{\nu} \nabla \times \underline{\vec{E}} + i\omega\kappa \underline{\vec{E}} = -i\omega \underline{\vec{J}}_s \tag{3.30a}$$

$$\nabla \cdot (\kappa \underline{\vec{E}} + \underline{\vec{J}}_s) = 0, \tag{3.30b}$$

where one should note that the source current density must be divergence free in non-conductive domains.

The system 3.30 has a unique solution only if domains with $\kappa = 0$ are absent. Since all gradient fields are in the kernel of the curl-curl operator, the solution of the MQS system is not unique in non-conductive domains. Regularizations of the singular curl-curl operator can be obtained by gauging, i.e. fixing data for $\nabla \cdot \underline{\vec{E}}$ where κ is zero. A famous gauge is obtained by adding a 'grad-div' term (see e.g. [73, 74]), such that the curl-curl operator converts into something similar to a vectorial Laplacian. However, the exact properties of the operator depend on $\underline{\nu}, \kappa$, and gauge constants in the 'grad-div' term. There are also opportunities to fix the gauge on the discrete level, e.g. by 'tree-cotree' gauging. Here, the degrees of freedom (DoFs) of a spanning tree are identified as the singular ones in the curl-curl operator and a regular system is obtained by solving for the cotree dofs only (see e.g. [75]).

In the computation of beam coupling impedance, the MQS approximation is almost identical to the radial model which will be discussed in the next subsection.

3.3.2 Darwin Model and Radial Model

More sophisticated quasi-stationary models are obtained by performing a Helmholtz split $\underline{\vec{E}} = \underline{\vec{E}}_{\text{div}} + \underline{\vec{E}}_{\text{curl}}$ on the displacement current density in Maxwell's equations:

$$\nabla \times \underline{\vec{E}} = -i\omega\vec{B} \tag{3.31a}$$

$$\nabla \times \underline{\vec{H}} = \underline{\vec{J}}_s + \kappa\underline{\vec{E}} + i\omega\varepsilon(\underline{\vec{E}}_{\text{div}} + \underline{\vec{E}}_{\text{curl}}) \tag{3.31b}$$

$$\nabla \cdot \varepsilon\underline{\vec{E}} = \underline{\varrho}_s \tag{3.31c}$$

$$\nabla \cdot \underline{\vec{B}} = 0 \tag{3.31d}$$

In Eq. 3.31b, the neglect of $\underline{\vec{E}}_{\text{curl}}$ is called *Darwin model* [76] and we will call the neglect of $\underline{\vec{E}}_{\text{div}}$ *radial model* (cf. [51, 52]). In the Darwin model we obtain the system

$$-\nabla \cdot \varepsilon\nabla\underline{\Phi} + i\nabla \cdot \frac{\kappa}{\omega}\nabla\underline{\Phi} = \underline{\varrho}_s \tag{3.32a}$$

$$\nabla \times \underline{\nu}\nabla \times \underline{\vec{E}}_{\text{curl}} + i\omega\kappa\underline{\vec{E}}_{\text{curl}} = \underline{\vec{R}} \tag{3.32b}$$

$$\underline{\vec{R}} = -\omega^2\underline{\varepsilon}\nabla\underline{\Phi} - i\omega\underline{\vec{J}}_s \tag{3.32c}$$

$$\nabla \cdot \underline{\vec{R}} = 0. \tag{3.32d}$$

Although the curl-curl equation looks similar as the one in the MQS approximation, it is regular since $\underline{\vec{E}}_{\text{curl}}$ is divergence-free by definition. The Darwin model is famous in plasma physics, when different velocity scales apply in different spatial directions. Generally, the Darwin model is well suited for low velocities and we report the following

Theorem 4. *The Darwin model approximates Maxwell's equations in free space to second order in β.*

Proof. See [77]. ☐

Furthermore, the Darwin model is restricted in frequency only by the wave propagation limit ω_{em} as it comprises both EQS (Eq. 3.32a) and MQS (Eq. 3.32b). Thus, the Darwin model seems to be suitable for impedance computation, provided the beam velocity is small, e.g. nonrelativistic ($v \ll c$).

The radial model reads as a second order PDE

$$\nabla \times \underline{\nu}\nabla \times \underline{\vec{E}}_{\text{curl}} + i\omega\kappa\underline{\vec{E}}_{\text{curl}} - \omega^2\varepsilon\underline{\vec{E}}_{\text{curl}} = -i\omega\underline{\vec{J}}_s \tag{3.33a}$$

$$\nabla \cdot (\underline{\vec{J}}_s + \kappa\underline{\vec{E}}) = 0, \tag{3.33b}$$

i.e. it is identical to the MQS with a divergence free wave term added. The source current density must also be divergence free, i.e. the charge is forced to zero.

In order to apply the beam source (cf. Eq. 2.64)

$$\underline{\vec{J}}_s = \sigma(\vec{r}_\perp)e^{-i\omega z/v}\vec{e}_z \tag{3.34a}$$

$$\underline{\varrho}_s = \frac{1}{v}\sigma(\vec{r}_\perp)e^{-i\omega z/v} \tag{3.34b}$$

to the radial model, the limit $v \to \infty$ has to be taken. Thus, the radial model is suitable under conditions where the Cherenkov condition is well exceeded, i.e.

$$\beta|\underline{n}| \gg 1. \tag{3.35}$$

This holds particularly in lossy material such as metals, but also in ferrites, see again Fig. 3.4, where it is illustrated that the material properties enter the beam impedance calculation for the radial model and the (highly relativistic) beam model in a similar manner.

Since the approximation property of the Darwin model is obtained by parametric expansion of Maxwell's equations, where the parameter is identified as the velocity, it can be suspected that similar reasoning applies to the radial model with the inverse parameter. Thus we formulate

Conjecture 1. *The radial model approximates Maxwell's equations to second order in* $1/\beta$*.*

The correspondence of the radial model to infinite velocity leads to the source fields being entirely 2D, i.e. $\partial_z = 0$. In longitudinally smooth structures, this property must also hold for the scattered fields.

Below the wave propagation frequency ω_{em}, the radial model coincides with MQS. Thus, at LF the radial model is suitable for numerical computation by standard tools, which are also used e.g. for eddy current problems. Also, the radial model supports modeling beam impedances by equivalent circuits, as $\nabla \cdot \underline{\vec{J}}_s = 0$ implies Kirchhoff's current law. Appropriate boundary conditions for the entry and exit of the current are given by a Perfectly Electric Conducting (PEC) surface, which forces the tangential component of the electric field to zero but keeps its normal component undefined.

Since the excitation is done by a current path of small size, the results for the imaginary impedance are severely polluted by the current path inductance, which depends strongly on the (equivalent) thickness of the current path. For FDTD or FIT on an equidistant Cartesian mesh, an equivalent thickness of a current path can be determined by fitting the fundamental solution of the 2D Helmholtz equation to numerically calculated fields, which results in an equivalent radius of ≈ 0.2 mesh cells [78]. The same approach can in principle also be performed for an unstructured mesh.

The inductance determined from the equivalent radius corresponds to the longitudinal space charge impedance (to be discussed in detail in the next section) in the limit of $\beta \to \infty$, i.e.

$$\lim_{\beta\to\infty} \beta^2\gamma^2 = \lim_{\beta\to\infty} \gamma^2 - 1 = -1. \tag{3.36}$$

This inductance usually outshines the imaginary part of the resistive wall impedance, which can thus not be determined by computation with the radial model.

However, the real part of the beam coupling impedance can be determined either from the real part of the source current path impedance, or, more accurately, from the losses in the whole computational domain. The loss integral reads for a model with conductive and magnetic losses as (cf. Poynting's theorem)

$$P(\omega_i) = \frac{1}{2} \int_{\Omega} \left(\omega \mu''(\vec{r}) |\vec{H}(\vec{r}, \omega_i)|^2 + \kappa(\vec{r}) |\vec{E}(\vec{r}, \omega_i)|^2 \right) \mathrm{d}^3 \vec{r}. \tag{3.37}$$

Note that we have switched here to phasor notation for the evaluation of fields and current of a particular fixed frequency ω_i, as it is done in CST EM-Studio® [40] (EMS). The longitudinal and dipolar transverse impedance can be calculated from the power loss as

$$\mathrm{Re}\left\{\underline{Z}_{\|}(\omega_i)\right\} = \frac{P(\omega_i)}{|\underline{I}|^2} \tag{3.38a}$$

$$\mathrm{Re}\left\{\underline{Z}_{\perp,x/y}(\omega_i)\right\} = \frac{c}{\omega_i d_{x/y}^2} \frac{P(\omega_i)}{|\underline{I}|^2}, \tag{3.38b}$$

where for the transverse impedance a dipole source with horizontal or vertical distance $d_{x/y}$ of the current paths has to be applied.

Figure 3.8 shows the example of a thin sheet beam pipe, which is a simplified model of the SIS-100 pipe (cf. Fig. 1.2b). The LF impedance calculation of the SIS-100 pipe by means of the radial model is discussed in [52] and excerpts are in App. C. The LF impedance curves for the bellow structure are in [79].

The longitudinal impedance can also be modeled as a transformer circuit, see Fig. 3.9, featuring a typical low-pass behavior. The calculation of the edge frequency can be found in [52]. For the transverse impedance a similar replacement circuit can be found

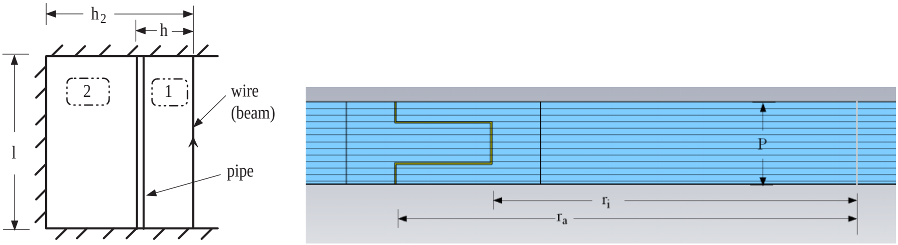

Figure 3.8.: Longitudinal cut through a thin resistive beam pipe [59] (left) and a bellow structure with period P (right).

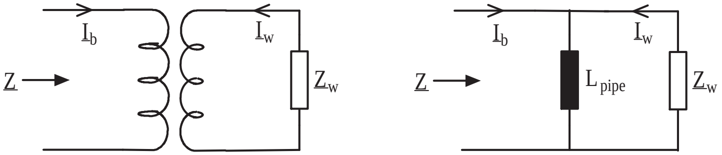

Figure 3.9.: Transformer model for beam and wall current and lumped element circuit for the longitudinal impedance at low frequency [59].

in [80] or [81], however, note that the edge frequency is different for longitudinal and transverse impedances.

A summary of the properties of the approximations of Maxwells equations is shown in Tab. 3.1. At low frequencies, the Darwin model and the radial model can be used for the determination of beam coupling impedance, provided the origin of the impedance is properly modeled. The Darwin model is particularly suitable for low beam velocity and the radial model is suitable for resistive wall impedances at high beam velocity, where the velocity term in the dispersion relation (Eq. 3.12) can be neglected. For the determination of beam coupling impedances in the high frequency range, the full Maxwell equations have to be solved.

Table 3.1.: Selected properties of approximations to Maxwell's equations (JS = Stationary Current, ES = Electro Statics, MS = Magneto Statics, FM = Full Maxwell).

	JS	ES	MS	EQS	MQS	Darwin	Radial	FM
Waves	✗	✗	✗	✗	✗	✗	✓	✓
Resonant circuits	✗	✗	✗	✗	✗	✓	✗	✓
Coulomb integral	✗	✓	✗	✓	✗	✓	✗	✓
Biot-Savart integral	✗	✗	✓	✓	✓	✓	✓	✓
L	✗	✗	✓	✗	✓	✓	✓	✓
C	✗	✓	✗	✓	✗	✓	✗	✓
R	✓	✗	✗	✓	✓	✓	✓	✓
Continuity eq.	✗	✗	✗	✓	✗	✓	✗	✓
Skin effect	✗	✗	✗	✗	✓	✓	✓	✓

3.4 Analytical Impedance Calculation in Cylindrically Symmetric Structures

An analytical calculation of the beam coupling impedance is only possible for simple structures, where a dedicated coordinate system can be attached. In the following we will assume a 2D cylindrical geometry as depicted in Fig. 3.10. Impedance calculations for parallel plate geometry can be found in e.g. [82, 83]. Two-dimensional impedance calculations always correspond to distributed impedances, as the dependence in longitudinal direction is solely given by the beam's longitudinal wave number $k_z = \omega/v$.

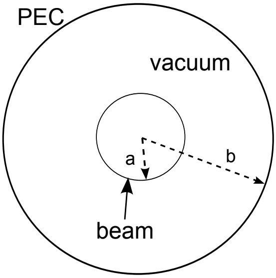

Figure 3.10.: Model for space charge impedance computation.

3.4.1 Space Charge Impedance

In a smooth perfectly conducting pipe, the beam experiences only the space charge impedance, which is at low frequencies proportional to γ^{-2}, since electric defocusing and magnetic focusing forces cancel [84]. The full Maxwell equations in vacuum imply (cf. Eq. 3.7)

$$\left[\triangle_\perp - \frac{\omega^2}{\beta^2\gamma^2c^2}\right]\underline{E}_z(\varrho,\varphi) = -\frac{i\omega\mu_0}{\beta^2\gamma^2}\sigma(\varrho,\varphi). \tag{3.39}$$

This PDE can be solved by a separation ansatz for both the longitudinal and transverse impedance, see e.g. [85, 86, 43]. In the following, the full Maxwell solutions are compared to the results from a modified version of the Darwin model. The Darwin model reads in the lossless case

$$\nabla\times\nu_0\nabla\times\underline{\vec{E}} + \omega^2\varepsilon_0\nabla\underline{\Phi} = -i\omega\underline{\vec{J}}_s, \tag{3.40a}$$

$$\nabla\cdot(\varepsilon_0\underline{\vec{E}}) = \underline{\varrho}_s, \tag{3.40b}$$

where the $\nabla\underline{\Phi}$ term is necessary to allow a current density on the right hand side that is not divergence free. Rewriting the first equation using $\nabla\times\nabla\times = \nabla(\nabla\cdot) - \triangle$ results in

$$\triangle\underline{\vec{E}} = i\omega\mu_0\underline{\vec{J}}_s + \frac{1}{\varepsilon_0}\nabla\underline{\varrho}_s + \omega^2\mu_0\varepsilon_0\nabla\underline{\Phi}, \tag{3.41a}$$

$$\triangle\underline{\Phi} = \frac{1}{i\omega\varepsilon_0}\nabla\cdot\underline{\vec{J}}_s = -\frac{\underline{\varrho}_s}{\varepsilon_0}, \tag{3.41b}$$

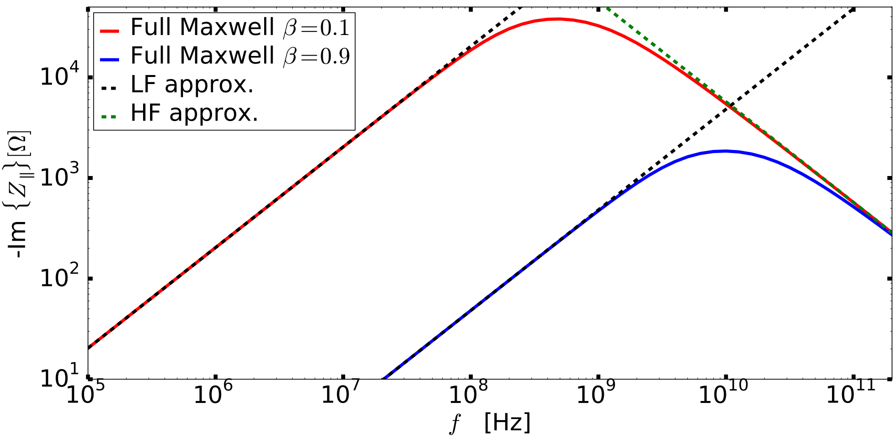

Figure 3.11.: Longitudinal space charge impedance with asymptotes.

where the second equation is obtained from taking the divergence of the first. The modification of the Darwin model consists of neglecting the wave term on the right hand side of Eq. 3.41a, while keeping the gradient of the charge density. The single second order PDE follows from Eq. 3.41a as

$$\left[\triangle_{\perp} - \frac{\omega^2}{\beta^2 c^2}\right] \underline{E}_z(\varrho,\varphi) = -\frac{i\omega\mu_0}{\beta^2\gamma^2}\sigma(\varrho,\varphi), \tag{3.42}$$

which is uniquely solvable in the same way as Eq. 3.39.

The solution of the full Maxwell system represented by Eq. 3.39 is for a monopole excitation (uniform beam) [85]

$$\underline{Z}_{\parallel}^{\text{spch}} = \frac{l}{i\omega\varepsilon_0\pi a^2}\left[1 - 2\mathrm{I}_1(k_\varrho a)\left(\mathrm{K}_1(k_\varrho a) + \frac{\mathrm{K}_0(k_\varrho b)}{\mathrm{I}_0(k_\varrho b)}\mathrm{I}_1(k_\varrho a)\right)\right], \tag{3.43}$$

with $k_\varrho = \omega/(\beta\gamma c)$ [9], where I_n and K_n are the modified Bessel functions of the first and second kind and n-th order, respectively. From Eq. 3.43 one finds the asymptotes for low and high frequency as (see Fig. 3.11)

$$\underline{Z}_{\parallel,\text{LF}}^{\text{spch}} = \frac{-i\omega\mu_0 l g_0}{2\pi\beta^2\gamma^2}\,, \quad g_0 = \frac{1}{4} + \ln\frac{b}{a}\,, \quad \underline{Z}_{\parallel,\text{HF}}^{\text{spch}} = \frac{-il}{\omega\varepsilon_0\pi a^2}, \tag{3.44}$$

---

[9] Although the radial dependence is an evanescent wave, k_ϱ has been chosen real-valued and it is combined with modified Bessel functions.

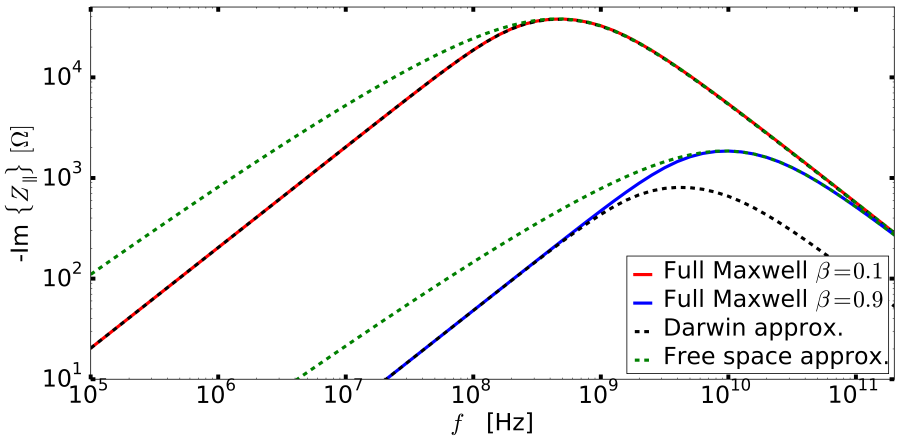

Figure 3.12.: Longitudinal space charge impedance with free-space and low-velocity approximations. The red and blue lines are the same as in Fig. 3.11.

where g_0 is usually referred to as geometry factor.

In the limit $b \to \infty$ in Eq. 3.43, one finds the free space solution,

$$\underline{Z}_{\|,\text{freespace}}^{\text{spch}} = \frac{l}{i\omega\varepsilon_0\pi a^2}\left[1 - 2\mathrm{I}_1(k_\varrho a)\mathrm{K}_1(k_\varrho a)\right]. \tag{3.45}$$

The free space solution for the longitudinal impedance should be considered carefully, as it is invalid at low frequency and also inconsistent with the low frequency approximation (Eq. 3.44).

The solution of the modified Darwin model reads

$$\underline{Z}_{\|,\mathrm{D}}^{\text{spch}} = \frac{l}{i\omega\varepsilon_0\pi a^2\gamma^2}\left[1 - 2\mathrm{I}_1(k_\varrho^{\mathrm{D}} a)\left(\mathrm{K}_1(k_\varrho^{\mathrm{D}} a) + \frac{\mathrm{K}_0(k_\varrho^{\mathrm{D}} b)}{\mathrm{I}_0(k_\varrho^{\mathrm{D}} b)}\mathrm{I}_1(k_\varrho^{\mathrm{D}} a)\right)\right] \tag{3.46}$$

with $k_\varrho^{\mathrm{D}} = \omega/(\beta c)$. Darwin and free-space longitudinal space charge impedances are plotted in Fig. 3.12, as comparison to the full Maxwell solution.

The transverse space charge impedance is found by applying the dipolar part of $\sigma(\varrho,\varphi)$ in Eq. 3.39 as [85]

$$\underline{Z}_{\perp}^{\text{spch}} = \frac{ilZ_0}{\beta\gamma^2\pi a^2}\mathrm{I}_1^2(k_\varrho a)\left(\frac{\mathrm{K}_1(k_\varrho b)}{\mathrm{I}_1(k_\varrho b)} - \frac{\mathrm{K}_1(k_\varrho a)}{\mathrm{I}_1(k_\varrho a)}\right). \tag{3.47}$$

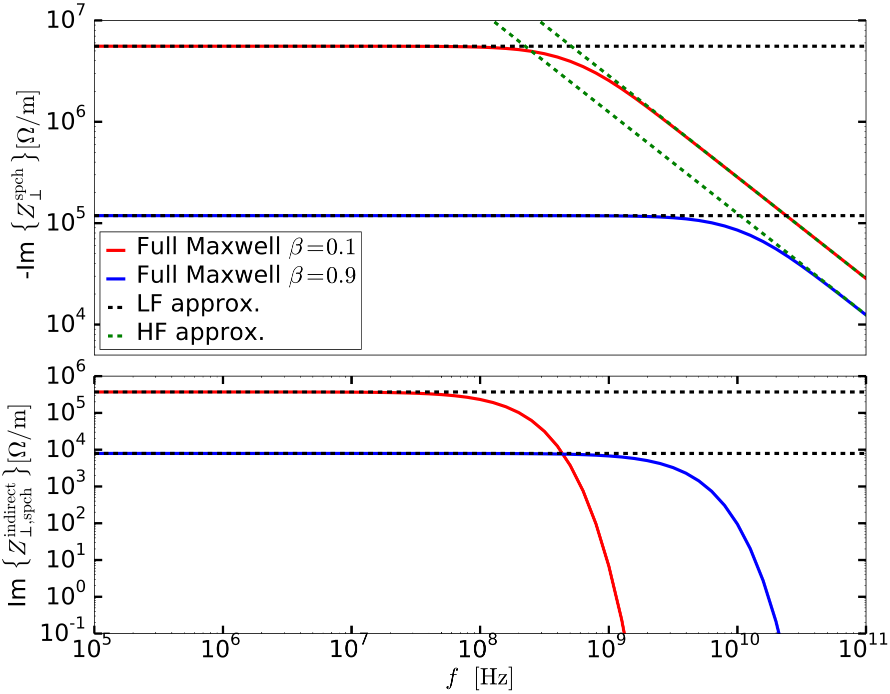

Figure 3.13.: Full transverse space charge impedance (top) and indirect part (bottom).

In order to take into account only the effect of the wall (‘indirect space charge’), one needs to subtract the ‘direct’ interaction of the source charge density. Only this *indirect* part acts *coherently* on the beam, whereas the direct part acts incoherently on the source charge distribution, i.e. different source particles are affected differently. Hence, the direct space charge impedance depends strongly on the particular representation of the dipole moment.

The indirect space charge impedance can be obtained from the total impedance by

$$\underline{Z}_{\perp,\mathrm{spch}}^{\mathrm{indirect}} = \underline{Z}_\perp^{\mathrm{spch}} - \lim_{b\to\infty} \underline{Z}_\perp^{\mathrm{spch}} = \frac{ilZ_0}{\beta\gamma^2\pi a^2}\mathrm{I}_1^2(k_\varrho a)\frac{\mathrm{K}_1(k_\varrho b)}{\mathrm{I}_1(k_\varrho b)}, \tag{3.48}$$

where one should note that this ‘free space approximation’, i.e. only the direct transverse space charge impedance, is consistent with its LF approximation. The asymptotes to Eq. 3.47 are

$$Z_{\perp,\mathrm{LF}}^{\mathrm{spch}} = \frac{-iZ_0 l}{2\pi\beta\gamma^2}\left(\frac{1}{a^2}-\frac{1}{b^2}\right), \quad \underline{Z}_{\perp,\mathrm{HF}}^{\mathrm{spch}} = \frac{-ilZ_0 c}{2\pi a^3\gamma\omega}, \tag{3.49}$$

where one observes again that the high frequency limit is independent of the pipe. Indirect and direct transverse space charge impedances are plotted in Fig. 3.13.

The Darwin model provides (note that there is no γ^2 in the denominator)

$$\underline{Z}^{\mathrm{spch}}_{\perp,\mathrm{D}} = \frac{ilZ_0}{\beta\pi a^2}\mathrm{I}_1^2(k_\varrho^{\mathrm{D}}a)\left(\frac{\mathrm{K}_1(k_\varrho^{\mathrm{D}}b)}{\mathrm{I}_1(k_\varrho^{\mathrm{D}}b)} - \frac{\mathrm{K}_1(k_\varrho^{\mathrm{D}}a)}{\mathrm{I}_1(k_\varrho^{\mathrm{D}}a)}\right), \tag{3.50}$$

which is invalid even in the LF limit for $\gamma \not\approx 1$.

3.4.2 Simplified Approach to Resistive Wall Impedance

A simplified approach to the calculation of the resistive wall impedance is obtained by allowing a finite, frequency dependent, surface impedance in Fig. 3.10. This surface impedance gives rise to a scattered field, which obeys the homogeneous Maxwell equations. For simplicity, a point charge is employed as source, denoted in FD as

$$\underline{\vec{J}}_s(\varrho,\varphi,z,\omega) = q\frac{\delta(\varrho)}{2\pi\varrho}e^{-i\omega z/v}\vec{e}_z. \tag{3.51}$$

For the longitudinal resistive wall impedance, the exact shape of the source plays only a minor role, as discussed in [87]. Without loss of generality, we set $z=0$ in the smooth pipe. With the point charge source, the (fundamental) solution[10] of the Helmholtz equation 3.39 reads (see e.g. [85])

$$\underline{E}_z^{\mathrm{source}}(\varrho,\varphi,z=0,\omega) = q\frac{i\omega\mu_0}{2\pi\beta^2\gamma^2}\mathrm{K}_0(\mathrm{k}_\varrho\varrho), \tag{3.52}$$

where again $k_\varrho = \omega/(\beta\gamma c)$. The scattered field must be finite in the origin, therefore

$$\underline{E}_z^{\mathrm{scat}}(\varrho,\varphi,z=0,\omega) = \underline{A}\mathrm{I}_0(k_\varrho\varrho), \tag{3.53}$$

with a complex amplitude $\underline{A}$ yet to be determined. From Maxwell's equations in cylindrical coordinates one finds the radial electric and azimuthal magnetic fields as

$$\underline{E}_\varrho = i\frac{\beta c}{\omega}\gamma^2\partial_\varrho\underline{E}_z, \quad \underline{H}_\varphi = \frac{\beta}{Z_0}\underline{E}_\varrho, \tag{3.54}$$

which holds for both source and scattered fields.

---

[10] A more demonstrative way to find this source field is to take the electrostatic field distribution in the beam's reference frame and perform a Lorentz transformation to the laboratory frame. Subsequent Fourier transform results in the same expression for $\underline{E}_z$, see [16].

Thus, the magnetic source and scattered fields read

$$\underline{H}_{\varphi}^{\text{source}} = \frac{q}{2\pi} k_{\varrho} \mathrm{K}_1(k_{\varrho}\varrho), \quad \underline{H}_{\varphi}^{\text{scat}} = \frac{\underline{A}}{Z_0} i\beta\gamma \mathrm{I}_1(k_{\varrho}\varrho). \tag{3.55}$$

The surface impedance gives

$$\underline{Z}_s(\omega) = \left. \frac{\underline{E}_z^{\text{source}} + \underline{E}_z^{\text{scat}}}{\underline{H}_{\varphi}^{\text{source}} + \underline{H}_{\varphi}^{\text{scat}}} \right|_{\varrho=b} \tag{3.56}$$

from which the amplitude $\underline{A}$ and thus the longitudinal impedance can be determined as

$$\underline{Z}_{\parallel} = \frac{\underline{A}l}{q} = \frac{l}{2\pi} \frac{\frac{i\omega\mu_0}{\beta^2\gamma^2}\mathrm{K}_0(k_{\varrho}b) - \underline{Z}_s k_{\varrho} \mathrm{K}_1(k_{\varrho}b)}{\frac{\underline{Z}_s}{Z_0} i\beta\gamma \mathrm{I}_1(k_{\varrho}b) - \mathrm{I}_0(k_{\varrho}b)}. \tag{3.57}$$

An asymptotic expansion of the Bessel functions for $\omega b \ll \beta\gamma c$ yields

$$\underline{Z}_{\parallel} = \frac{l}{2\pi} \frac{\underline{Z}_s/b + \frac{i\omega\mu_0}{\beta^2\gamma^2}(\gamma_e + \ln(k_{\varrho}b/2))}{1 - i\frac{\omega b}{2c}\frac{\underline{Z}_s}{Z_0}}, \tag{3.58}$$

where $\gamma_e \approx 0.577$ is Euler's constant. In the ultrarelativistic limit one obtains (cf. [88])

$$\underline{Z}_{\parallel} \approx \frac{l\underline{Z}_s}{2\pi b}, \tag{3.59}$$

where the cutoff term in the denominator, $\underline{Z}_s\omega b/2Z_0c$, is small for a metallic pipe and can be neglected unless extremely high frequencies are considered.

A similar expression is found for the dipolar transverse resistive wall impedance in the ultrarelativistic limit [89],

$$\underline{Z}_{\perp} \approx \frac{cl\underline{Z}_s}{\omega\pi b^3}. \tag{3.60}$$

Low and high frequency aspects of resistive wall impedance are discussed in more detail in [52] and [88], respectively. The full longitudinal and transverse impedance of an axis-symmetric multilayer cylindrical structure can be obtained by means of the field matching technique by the Mathematica® [90] script Rewall [50], developed at CERN. Although the calculation is fully analytical, the numerical evaluation of the final result can become time consuming and is prone to numerical cancellation effects. Nonetheless, if the number of layers is not too high, Rewall has proven to be an effective tool. Especially for the validation of the 2D numerical impedance solvers presented in this thesis, Rewall was used extensively.

4 Numerical Impedance Computation

The first section of this chapter presents TD methods to calculate beam coupling impedance. Here, the focus is on applicability and results, rather than on detailed computational aspects. The section 4.2 presents the FIT and FEM full Maxwell approaches which have been implemented in FD in the course of this thesis. Applicability, implementation, numerical issues, and finally the results relevant for beam physics, are discussed.

4.1 Time Domain

Wakefield and impedance computation is nowadays mostly done in the time domain, due to efficient algorithms which are available in commercial and non-commercial software packages. Summaries of those can be seen in e.g. [91, 92]. The wake potential is obtained by integrating the electromagnetic fields in the TD and the impedance is subsequently found by discrete Fourier transform (DFT). In order to obtain the point-charge impedance, the convolution theorem requires to divide by the excitation bunch spectrum as

$$\underline{\vec{Z}}(\omega) = \frac{\mathscr{F}\{\vec{W}(s)\}(\omega)}{\mathscr{F}\{\lambda(s)\}(\omega)}. \tag{4.1}$$

Due to the minimal duration-bandwidth-product, the excitation is usually done by a Gaussian bunch

$$\lambda(z,t) = \frac{q}{\sqrt{2\pi}\sigma_s} e^{-\frac{1}{2}\left(\frac{z-vt}{\sigma_s}\right)^2} \tag{4.2}$$

which rigidly moves through the structure. The spectrum of this pulse is obtained from the FT over $s = vt - z$ as

$$\left|\underline{\lambda}(\omega)\right| = \frac{q_\omega}{\sqrt{2\pi}\sigma_\omega} e^{-\frac{1}{2}\left(\frac{\omega}{\sigma_\omega}\right)^2}, \tag{4.3}$$

where $\sigma_\omega = v/\sigma_s$ and the normalization is $q_\omega = q\sqrt{2\pi}\sigma_\omega/v$. The duration and bandwidth are

$$T = \frac{\sigma_s}{\sqrt{2}v}, \qquad B = \frac{v}{\sigma_s\sqrt{2}}, \tag{4.4}$$

resulting in $TB = 1/2$. The choice of the bunch length σ_s does not necessarily depend on the real bunch length in the accelerator, but rather on the frequency of interest. The maximum frequency at which a reasonable excitation amplitude is present, is roughly $2\sigma_f$, i.e. the spectrum is mainly located at $\sigma_f = v/(2\pi\sigma_s)$, the so-called frequency associated with the bunch length. Shorter bunches increase the maximum frequency, but they decrease the frequency resolution, which is a particular problem at LF. The frequency resolution depends on the total number of points employed for the DFT[1], N_{DFT}, as

$$\Delta f = \frac{1}{N_{\text{DFT}}\Delta t}. \tag{4.5}$$

The total integrated wake length is $L_{\text{W}} = vN_{\text{DFT}}\Delta t$. Bunch length and wake length are the two crucial parameters for TD impedance computation. The choice of finite L_{W} puts a window-function on the real wake potential. If it is chosen too small, i.e. when the window closes before the wake has decayed, the resulting impedance will show the Gibbs phenomenon. This can be smoothed by choosing other than rectangular window functions, however, this does not provide additional information or increase the frequency resolution.

Most common TD wake field computation methods are based on Finite Differences Time Domain (FDTD, Yee 1966 [93]) or Finite Integration Technique (FIT, Weiland 1977 [94]). More specialized techniques are the Boundary Element Method (BETD) [95, 96, 97], the Finite Volume method (FVTD) [98], Discontinuous Galerkin Finite Element (DG-FEM), and implicit methods. In the following we focus on the FIT, which gives an identical space discretization as FDTD for a Cartesian mesh.

The discretization of time derivatives can be done by forward (explicit) or backward (implicit) finite differences. Implicit methods are unconditionally stable, but they require solving a System of Linear Equations (SLE) in each time step. Explicit methods are much lighter in computation, since they can be written as a matrix-vector multiplication in each time step. A major drawback of explicit methods is that they are only conditionally stable and some are even always unstable. The most commonly used explicit method is the so-called ‘leap-frog’ method, introduced by Yee [93] in 1966. It consists of a (staggered) central difference quotient featuring second order accuracy. The stability of the scheme is connected to the grid dispersion relation, which describes the velocity of a plane wave on the grid as dependent on the direction of the wave vector. It reads for a particular Cartesian cell $(\Delta x, \Delta y, \Delta z)$ (see e.g. [99])

$$\left(\frac{\sin\frac{k_x\Delta x}{2}}{\Delta x/2}\right)^2 + \left(\frac{\sin\frac{k_y\Delta y}{2}}{\Delta y/2}\right)^2 + \left(\frac{\sin\frac{k_z\Delta z}{2}}{\Delta z/2}\right)^2 = \mu\varepsilon\left(\frac{\sin\frac{\omega\Delta t}{2}}{\Delta t/2}\right)^2, \tag{4.6}$$

reproducing the continuous dispersion relation

$$k_x^2 + k_y^2 + k_z^2 = \omega^2\mu\varepsilon \tag{4.7}$$

in the limit $\Delta x, \Delta y, \Delta z, \Delta t \to 0$.

---

[1] We assume an equidistant DFT. More advanced semi-analytical Fourier transform techniques for beam coupling impedances can be found in e.g. [14].

In order to fulfill 4.6 with real valued frequency and wavenumbers, at least

$$\Delta t \leq \min_i \sqrt{\frac{\mu_i \varepsilon_i}{\frac{1}{\Delta x_i^2} + \frac{1}{\Delta y_i^2} + \frac{1}{\Delta z_i^2}}} \tag{4.8}$$

must hold, where the minimum is taken over all mesh cells[2]. This is also referred to as the Courant-Friedrichs-Lewy (CFL) criterion [100] for the time step Δt. It can be shown [99, 101], that Eq. 4.8 is also a sufficient condition for stability on the time step.

At low frequencies, Eq. 4.8 already poses a strong requirement on the time step. Due to the uncertainty principle, lower frequencies require computing longer wakes. As the time step is fixed by structure properties via the CFL criterion (Eq. 4.8), this leads to the necessity to compute a large number of time steps, i.e. massive oversampling of a LF wave.

Time domain simulations using FIT or FDTD are suitable at medium and high frequency, and particularly in perfectly conducting structures. They are disadvantageous for low frequencies and low velocity of the beam. Also dispersively lossy materials are difficult to treat in TD, since a convolution with the impulse response, i.e. the inverse FT of the material dispersion curve, is necessary. This impulse response is usually taken as a particular dispersion model featuring a number of resonances, which are fitted to the dispersion data given for the material in FD (see e.g. [102] for details).

An example, which is used for the validation of different methods throughout this thesis, is a ferrite (cf. Fig. 3.3) ring. The longitudinal impedance is obtained by DFT of the wake potential, which is computed by CST Particle Studio® [40] (PS). The impedance for two different housing scenarios is shown in Fig. 4.1. One is small beam pipe, with radius equal to the inner radius of the ring and the other is a large beam pipe enclosing the whole ring. Plotted is the longitudinal impedance normalized to the length $l_0 = 2.54\,\mathrm{cm}$, for 2D analytic calculation using a field matching algorithm [59], and 3D PS computation for varying length. The two scenarios show a quite different behavior for the length scaling.

In order to explain this we have to introduce the concept of lumped and distributed impedance. A lumped impedance is located at a particular z-position, it can be due to an abrupt cross-section or pipe material change. A distributed impedance scales linearly with its length, as e.g. space charge or resistive wall impedance for a smooth pipe. Obviously, 2D (x, y) impedance solvers are suitable only for distributed impedances. Lumped impedances can in some simple cases be treated by 0D replacement circuits (lumped elements), however, in most practical cases, a full 3D simulation is required.

For the ferrite ring in Fig. 4.1, one recognizes that the cavity-like setup (left) features an impedance which scales (almost) linearly with the length. Thus, the transition from the pipe to the ferrite must have a rather small lumped impedance. This is different for the large pipe setup (right), where ten times the length is required to see a length inde-

---

[2] A more detailed analysis of the time-step requirements can be done by looking at the eigenvalues of the iteration matrix, see [99].

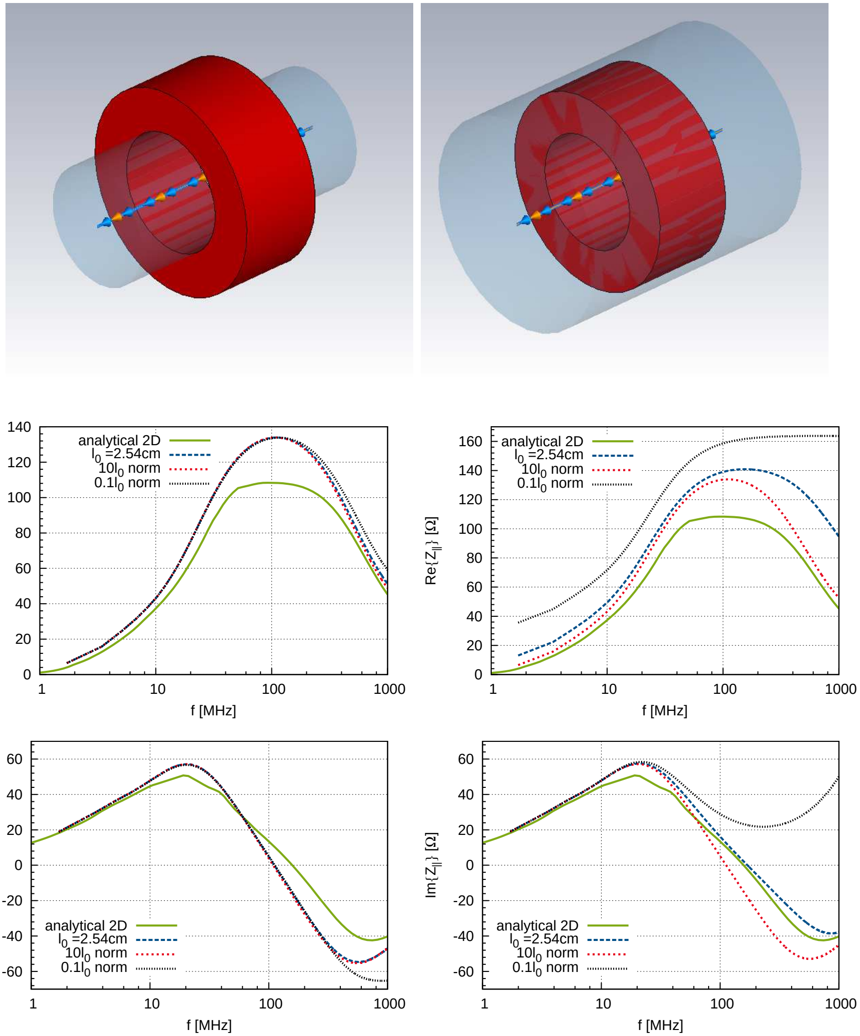

Figure 4.1.: PS simulation for varying length of a ferrite ring compared to analytical 2D model (see [59]). The left plots are for a Cavity-like setup with beam pipe radius $r_p = r_1 = 1.78\,\text{cm}$ and the right ones are for larger beam pipe with radius $r_p = r_3 = 3.3\,\text{cm}$ enveloping the whole ferrite ring. The dashed curves are for different length of the ring, normalized to the length l_0 =2.54 cm. The pictures are reused from [59].

pendent normalized curve. The discrepancy between the length independent curve to the 2D analytical result originates from the error due to the fitting of the dispersive material data to the impulse response model. Choosing a very high order impulse response model was found to diminish this discrepancy only slightly.

4.2 Frequency Domain

This section treats the two solvers that have been implemented in the course of this thesis. Although already used as software package for TD wake field computation, the FIT is introduced here and the implementation of Floquet boundary conditions for the entry and exit of the beam is described.

The FIT on a rectangular (staircase) mesh is not suitable for modeling structures with curved boundaries. Especially the circular shape of the beam source, required for the computation of space charge impedances, cannot be modeled by FIT. Therefore the second part of this section is dedicated to a 2D Finite Element solver, which enhances the quality of the source modeling and the representation of curved boundaries significantly.

Many decisive properties of the Maxwell-system in FD are given by the kernel of the curl-curl operator, namely the space of all gradient fields. The curl-curl wave equation is regular, only because the $\omega^2\varepsilon$ term is added. However, this term becomes small at low frequency and thus the system matrix is close to singular, i.e. ill conditioned. This phenomenon is called the *low frequency instability* for the curl-curl wave equation [103].

The low frequency instability has been clearly observed during this thesis, see e.g. [104]. However, already established countermeasures can be mentioned [103, 105], but an implementation is beyond the scope of this work. A detailed treatise on low frequency stabilized FEM formulations can be found in [106].

4.2.1 Finite Integration Technique (FIT)

The finite integration technique introduced by Weiland in 1977 [94] is based on evaluating the integral form of Maxwell's equations on a given mesh, i.e.

$$\begin{aligned}
\overset{\frown}{\underline{\mathbf{e}}}_i &= \int_{L_i} \underline{\vec{E}}\cdot\mathrm{d}\vec{s} & \overset{\frown}{\underline{\mathbf{h}}}_i &= \int_{\tilde{L}_i} \underline{\vec{H}}\cdot\mathrm{d}\vec{s} & \underline{\mathbf{q}}_i &= \int_{\tilde{V}_i} \underline{\varrho}\,\mathrm{d}V \\
\overset{\frown\frown}{\underline{\mathbf{d}}}_i &= \int_{\tilde{A}_i} \underline{\vec{D}}\cdot\mathrm{d}\vec{A} & \overset{\frown\frown}{\underline{\mathbf{b}}}_i &= \int_{A_i} \underline{\vec{B}}\cdot\mathrm{d}\vec{A} & \overset{\frown\frown}{\underline{\mathbf{j}}}_i &= \int_{\tilde{A}_i} \underline{\vec{J}}\cdot\mathrm{d}\vec{A}.
\end{aligned} \tag{4.9}$$

The resulting quantities[3] are the electric and magnetic edge voltages $\overset{\frown}{\underline{\mathbf{e}}}$ and $\overset{\frown}{\underline{\mathbf{h}}}$, face fluxes $\overset{\frown\frown}{\underline{\mathbf{d}}}$ and $\overset{\frown\frown}{\underline{\mathbf{b}}}$, and the face current $\overset{\frown\frown}{\underline{\mathbf{j}}}$ and volume charge $\underline{\mathbf{q}}$, which are connected by the

---

[3] Here, all quantities are spectral densities.

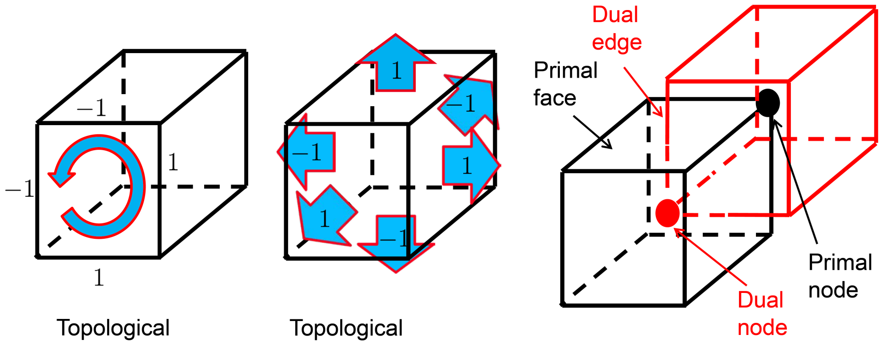

Topological curl ($\mathbf{C}$)

Topological div ($\mathbf{S}$)

Mesh duality

Figure 4.2.: Topological FIT mesh properties.

continuity equation. Combining the integrals 4.9 to closed loops or closed surfaces (see Fig. 4.2) results in the Maxwell-grid-equations (MGE)

$$\mathbf{C}\underline{\widehat{\mathbf{e}}} = -i\omega\underline{\widehat{\widehat{\mathbf{b}}}} \tag{4.10a}$$

$$\widetilde{\mathbf{C}}\underline{\widehat{\mathbf{h}}} = \underline{\widehat{\widehat{\mathbf{j}}}}_s + \underline{\widehat{\widehat{\mathbf{j}}}} + i\omega\underline{\widehat{\widehat{\mathbf{d}}}} \tag{4.10b}$$

$$\widetilde{\mathbf{S}}\underline{\widehat{\widehat{\mathbf{d}}}} = \underline{\mathbf{q}}_s \tag{4.10c}$$

$$\mathbf{S}\underline{\widehat{\widehat{\mathbf{b}}}} = 0, \tag{4.10d}$$

where $\mathbf{C}$ and $\mathbf{S}$ are purely topological curl and divergence operators, that form a discrete de-Rham sequence as shown in Fig. 4.3. The operators $\widetilde{\mathbf{C}}, \widetilde{\mathbf{S}}$ in Eqs. 4.10 represent evaluation on a dual grid, which has the property that dual vertices and edges intersect primal volumes and faces with same index, respectively, and vice versa, see Fig. 4.2 (right). The MGE 4.10 are exact, since they represent an evaluation of Maxwell's equations on a given grid topology.

$$\begin{tikzcd}
\underline{\varphi} \arrow[r, "\mathbf{G}"] & \underline{\widehat{\mathbf{e}}} \arrow[r, "\mathbf{C}"] \arrow[d, dotted, leftrightarrow, "\mathbf{M}_{\underline{\varepsilon}}"] & \underline{\widehat{\widehat{\mathbf{b}}}} \arrow[r, "\mathbf{S}"] \arrow[d, dotted, leftrightarrow, "\mathbf{M}_{\underline{\nu}}"] & 0 \\
\underline{\mathbf{q}} & \underline{\widehat{\widehat{\mathbf{d}}}} \arrow[l, "\widetilde{\mathbf{S}}"'] & \underline{\widehat{\mathbf{h}}} \arrow[l, "\widetilde{\mathbf{C}}"'] & \underline{\varphi}_{\mathrm{m}} \arrow[l, "\widetilde{\mathbf{G}}"']
\end{tikzcd}$$

Figure 4.3.: Connection of the FIT state variables and matrix operators. The operators form a complete discrete de-Rham sequence.

Throughout this thesis, for FIT only hexahedral (staircase) mesh and the so-called canonical indexing

$$\begin{aligned} n = 1 + (n_x - 1)M_x + (n_y - 1)M_y + (n_z - 1)M_z, \\ M_x = 1, \quad M_y = N_x, \quad M_z = N_x \cdot N_y \end{aligned} \tag{4.11}$$

are used, where n_x, n_y, n_z are the x, y, z indices running from 1 to N_x, N_y, N_z and n is the global index. Another indexing scheme, which can be particularly advantageous for parallel computing, can be found in [67]. For the indexing according to Eq. 4.11 the discrete partial derivative operators are given by

$$\left[\mathbf{P}_{x,y,z}\right]_{m,n} = \begin{cases} -1, & \text{if} \quad m = n \\ 1, & \text{if} \quad m = n - M_{x,y,z} \\ 0, & \text{else.} \end{cases} \tag{4.12}$$

The grid incidence matrices $\mathbf{C}$ and $\mathbf{S}$ can be written in terms of the partial derivative incidence operators $\mathbf{P}_x, \mathbf{P}_y, \mathbf{P}_z$ as

$$\mathbf{C} = \begin{bmatrix} 0 & -\mathbf{P}_z & \mathbf{P}_y \\ \mathbf{P}_z & 0 & -\mathbf{P}_x \\ -\mathbf{P}_y & \mathbf{P}_x & 0 \end{bmatrix} \quad \mathbf{S} = \begin{bmatrix} \mathbf{P}_x & \mathbf{P}_y & \mathbf{P}_z \end{bmatrix} \quad \mathbf{G} = \begin{bmatrix} \mathbf{P}_x \\ \mathbf{P}_y \\ \mathbf{P}_z \end{bmatrix}. \tag{4.13}$$

The following crucial relations can be established [107]:

$$\begin{aligned} &\widetilde{\mathbf{P}}_\xi = -\mathbf{P}_\xi^{\mathrm{T}} && \mathbf{P}_\xi \mathbf{P}_\chi = \mathbf{P}_\chi \mathbf{P}_\xi && \text{for} \quad \xi, \chi \in \{x, y, z\} && \\ &\widetilde{\mathbf{C}} = \mathbf{C}^{\mathrm{T}} && \mathbf{G} = -\widetilde{\mathbf{S}}^{\mathrm{T}} && \widetilde{\mathbf{G}} = -\mathbf{S}^{\mathrm{T}} && \\ &\mathbf{C}\mathbf{G} = 0 && \widetilde{\mathbf{C}}\widetilde{\mathbf{G}} = 0 && \mathbf{S}\mathbf{C} = 0 && \widetilde{\mathbf{S}}\widetilde{\mathbf{C}} = 0 \end{aligned} \tag{4.14}$$

The numerical approximations required to solve the MGE are included in the material matrices

$$\underline{\widehat{\mathbf{h}}} = \mathbf{M}_\nu \underline{\widehat{\widehat{\mathbf{b}}}}, \qquad \underline{\widehat{\widehat{\mathbf{d}}}} = \mathbf{M}_\varepsilon \underline{\widehat{\mathbf{e}}}, \qquad \underline{\widehat{\widehat{\mathbf{j}}}} = \mathbf{M}_\kappa \underline{\widehat{\mathbf{e}}}, \tag{4.15}$$

which are diagonal matrices due to the dual orthogonal mesh. The expressions for $\mathbf{M}_\nu$ and $\mathbf{M}_\varepsilon$ are obtained from appropriate averaging (see Fig. 4.4) of the material parameters, which are assumed to be homogeneous fillings in the primal cells. This averaging must therefore include the dimensions of the mesh, i.e. the metric, represented here by edge lengths L_i and face areas A_i, and the respective duals denoted by a tilde. Invoking

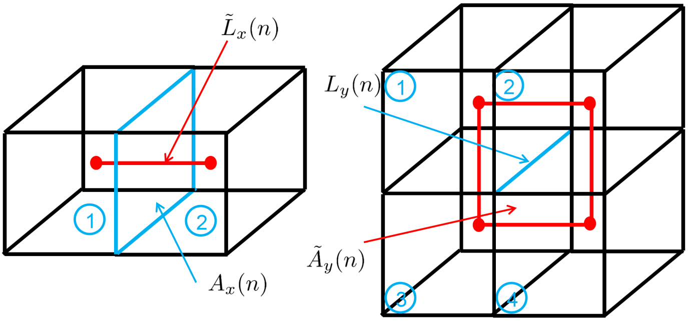

Figure 4.4.: Material averaging in the dual-orthogonal mesh. Left: averaging of ν over a dual edge, and right: averaging of ε over a dual face.

the normal component of $\vec{B}$ and and the tangential component of $\vec{E}$ to be continuous at a material jump, one finds [108]

$$[\mathbf{M}_\nu]_{n,n} = \overline{\nu}_n \frac{\tilde{L}_n}{A_n} = \frac{\int_{\tilde{L}_n} \vec{H} \cdot \mathrm{d}\vec{s}}{\int_{A_n} \vec{B} \cdot \mathrm{d}\vec{A}} + \mathcal{O}(h^{2\ldots3}) \tag{4.16a}$$

$$[\mathbf{M}_\varepsilon]_{n,n} = \overline{\varepsilon}_n \frac{\tilde{A}_n}{L_n} = \frac{\int_{\tilde{A}_n} \vec{D} \cdot \mathrm{d}\vec{A}}{\int_{L_n} \vec{E} \cdot \mathrm{d}\vec{s}} + \mathcal{O}(h^{3\ldots4}) \tag{4.16b}$$

where h is the mesh size parameter and the averaged material parameters are[4]

$$\overline{\nu}_x(n) := \frac{\nu_1 L_{x,1} + \nu_2 L_{x,2}}{L_{x,1} + L_{x,2}} \tag{4.17a}$$

$$\overline{\varepsilon}_y(n) := \frac{\varepsilon_1 A_{y,1} + \varepsilon_2 A_{y,2} + \varepsilon_3 A_{y,3} + \varepsilon_4 A_{y,4}}{A_{y,1} + A_{y,2} + A_{y,3} + A_{y,4}}, \tag{4.17b}$$

with proper choice of the local indices according to Fig. 4.4 and Eq. 4.11. The error order in Eq. 4.16 is the local inconsistency error of the material matrices (see also [109]). The global error order, which matters for the field energy or localized quantities of interest (e.g. impedance), reaches 3 only in an equi-distant mesh and constant material distribution and is 2 in the other cases which are practically relevant [108]. The inverse material relations are by definition

$$\mathbf{M}_\mu := \mathbf{M}_\nu^{-1}, \quad \mathbf{M}_{\varepsilon^{-1}} := \mathbf{M}_\varepsilon^{-1}, \tag{4.18}$$

---

[4] The nodes of the dual mesh are assumed to be centered in the primal volumes, i.e. the primal nodes are not centered in the dual volumes for a non-equidistant mesh.

where the inverse of such a diagonal matrix is to be seen as a ‘pseudo-inverse’, i.e.

$$\left[\mathbf{D}^{-1}\right]_{n,n} = \begin{cases} [\mathbf{D}]_{n,n}^{-1} & , \quad [\mathbf{D}]_{n,n} \neq 0 \\ 0 & , \quad [\mathbf{D}]_{n,n} = 0. \end{cases} \tag{4.19}$$

Note that the above material matrices can be treated in the same way for complex material parameters and for brevity we will sometimes write

$$\mathbf{M}_{\underline{\varepsilon}} = \mathbf{M}_{\varepsilon} + \frac{1}{i\omega}\mathbf{M}_{\kappa}. \tag{4.20}$$

Combining Eqs. 4.10, the discrete curl-curl wave equation reads

$$\left(\widetilde{\mathbf{C}}\mathbf{M}_{\underline{\nu}}\mathbf{C} + i\omega\mathbf{M}_{\kappa} - \omega^2\mathbf{M}_{\varepsilon}\right)\underline{\widehat{\mathbf{e}}} = -i\omega\underline{\widehat{\widehat{\mathbf{j}}}}_s. \tag{4.21}$$

In the following, the system is rewritten using $\underline{\widehat{\mathbf{e}}} = \mathbf{M}_{\varepsilon}^{-1/2}\underline{\widehat{\mathbf{e}}}'$ as

$$(\mathbf{M}_{\varepsilon}^{-1/2}\widetilde{\mathbf{C}}\mathbf{M}_{\underline{\nu}}\mathbf{C}\mathbf{M}_{\varepsilon}^{-1/2} - i\omega\mathbf{M}_{\varepsilon}^{-1/2}\mathbf{M}_{\kappa} - \omega^2 I)\underline{\widehat{\mathbf{e}}}' = -i\omega\mathbf{M}_{\varepsilon}^{-1/2}\underline{\widehat{\widehat{\mathbf{j}}}}_e, \tag{4.22}$$

abbreviated $\mathbf{A}\underline{\widehat{\mathbf{e}}}' = b$, which is symmetric but non-Hermitian, since the losses due to conductivity or complex permeability lead to complex eigenvalues of the system matrix.

Source Terms and Impedance Evaluation

The monopolar excitation current is given for a single beam filament as

$$\underline{\widehat{\widehat{\mathbf{j}}}}_{e,z}^{\text{mono}}(n_z) = \int \underline{\vec{J}} \cdot \mathrm{d}\vec{A}_z = qe^{-i\omega\tilde{z}_i/v} \tag{4.23}$$

where $\tilde{z}_i$ is the z coordinate at which $L_z(n_z)$ and $\tilde{A}_z(n_z)$ intersect. Similarly as for the radial model simulations (cf. Sect. 3.3.2), Waldschmidt’s equivalent thickness of filaments [78] applies here. However, a thick beam source can be defined by taking many such filaments in parallel. This allows to get an approximation of a round beam, within the accuracy constraints of the staircase FIT. A simple model to show that the FIT recovers all the qualitative properties of the longitudinal space charge impedance can be found in App. D.

The dipolar excitation current is modeled by the twin wire dipole approximation as (see also [110])

$$\underline{\widehat{\widehat{\mathbf{j}}}}_{e,z}^{\text{dip}}(i_z) = \underline{\widehat{\widehat{\mathbf{j}}}}_{e,z}^{\text{mono}}(x = -d_x/2) - \underline{\widehat{\widehat{\mathbf{j}}}}_{e,z}^{\text{mono}}(x = +d_x/2). \tag{4.24}$$

This approximation is convenient only for ultrarelativistic beams, since the space charge impedance cannot be obtained analytically for such a dipole on the finite rectangular mesh. Thus, the direct transverse space charge impedance is unknown and cannot be subtracted from the final result, in order to obtain the wall impedance only.

The beam's charge in the dual volumina is obtained using the continuity equation

$$\underline{\mathbf{q}}_s(i_z) = \frac{i}{\omega}\widetilde{\mathbf{S}}\underline{\widehat{\widehat{\mathbf{j}}}}_s = \frac{i}{\omega}(e^{-i\omega\frac{\Delta z}{2v}} - e^{-i\omega\frac{-\Delta z}{2v}})qe^{-i\omega z_i/v} = \frac{\Delta z}{v}\underline{\widehat{\widehat{\mathbf{j}}}}_s + \mathcal{O}(\Delta z^3) \tag{4.25}$$

for a longitudinally equidistant grid.

Finally, the impedance can be evaluated by a discretization of Eqs. (2.66) and (2.69) as

$$\underline{Z}_{\|}(\underline{\widehat{\mathbf{e}}}(\omega)) = -\frac{1}{q^2}\underline{\widehat{\mathbf{e}}} \cdot \underline{\widehat{\widehat{\mathbf{j}}}}^*_{\text{mono}} \tag{4.26}$$

$$\underline{Z}_{\perp}(\underline{\widehat{\mathbf{e}}}(\omega)) = -\frac{v}{\omega(qd_x)^2}\underline{\widehat{\mathbf{e}}} \cdot \underline{\widehat{\widehat{\mathbf{j}}}}^*_{\text{dip}}, \tag{4.27}$$

which can be seen as a functional of the discrete solution of Maxwell's equations in FD.

Boundary Conditions and 2D Simulations

Perfectly electric (PEC) boundaries are imprinted by enforcing the respective Degree of Freedom (DoF) of the electric field to be zero at the particular edge. This can be done by setting a particular column in the curl matrix to zero. The boundary normal magnetic flux is set to zero by setting a row in the curl matrix to zero. The according effect on the dual curl matrix is created by taking the transpose of the primal one. Thus, the system matrix maintains its symmetry. Another way to include PEC boundary conditions is in the material matrices, which keeps the system matrix symmetric according to Eq. 4.22.

For the entry and exit of the beam current (Eq. 4.23) in the computational domain, dedicated boundary conditions are required. There are two different options to implement them, quasi-periodic (Floquet-) boundary conditions or infinite beam pipe boundary conditions. Both assume that the excitation frequency is below the cut-off of the pipe, and the port is sufficiently far away such that scattered fields are decayed and only source fields are present in the port region.

For a longitudinally homogeneous pipe the correspondence $\partial_z \rightarrow -i\omega/v$ holds, see again Eq. 3.4. Therefore one can solve the boundary in 2D and attach the solution as an inhomogeneous Dirichlet condition to the 3D case. Simpler, one can also think of many identical devices in a sequence, which leads to phase corrected periodic (Floquet-) boundary conditions. For the transformation from the entry to the exit of the beam the phase factor reads

$$P_{z,\text{exp}} = e^{-i\frac{\omega(L+\Delta z_{\text{exit}})}{\beta c}}, \tag{4.28}$$

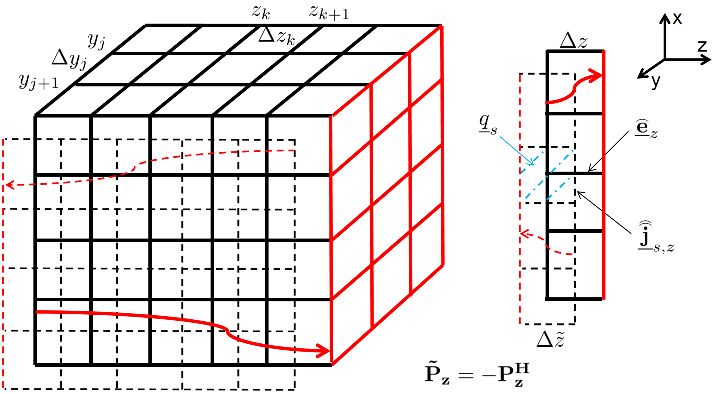

Figure 4.5.: Quasi-periodic (Floquet) boundary conditions in 3D and 2D.

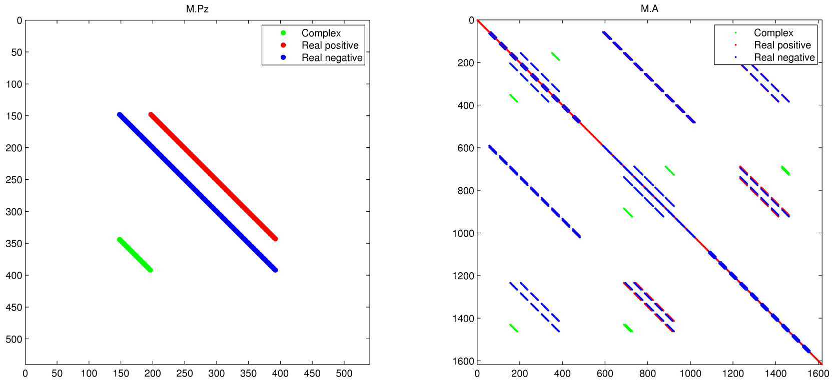

Figure 4.6.: Sparsity pattern of partial derivative $\mathbf{P}_z$ (left) and system matrix **A** of Eq. 4.22 (right) with Floquet BC in z-direction and PEC-BC in x,y-direction.

where Δz_{exit} is the length of a former ‘ghost’-edge[5] and the total length of the computational domain is now $L + \Delta z_{\text{exit}}$. The factor $P_{z,\text{exp}}$ enters the partial derivative matrix

---

[5] A ’ghost’ edge/face/volume is an entity which is supposedly placed outside the computational domain.

$\mathbf{P}_z$ as displayed in Fig. 4.6. As the impact of $P_{z,\mathrm{exp}}$ on the dual operator $\widetilde{\mathbf{P}}$ is in reverse direction, it follows that

$$\boxed{\widetilde{\mathbf{P}} = -\mathbf{P}^{\mathrm{H}}} \tag{4.29}$$

and subsequently the transposes in Eq. 4.14 can be replaced by Hermitian transposes. This means that a lossless system with Floquet BC is still Hermitian. Choosing $L = 0$, the length of the domain is just one edge Δz_{exit}, which constitutes the two-dimensional setup (see Fig. 4.5). As for the analytical calculations, in the 2D numerical computation the scattered fields have to have the same longitudinal periodicity as the source fields.

Helmholtz Decomposition

Mostly in 3D it makes sense to apply a Helmholtz-split on the wave equation, since a divergence free curl-curl algebraic system is easier to treat with iterative solvers [111, 110]. Analogously to Theorem 3 (see also [56] p.170) a Helmholtz decomposition can be performed for mimetically discretized fields. Since FIT is a mimetic discretization, the requirements for the discrete Helmholtz decomposition are the same as for the continuous ones. The electric field can be written as $\underline{\widehat{\mathbf{e}}} = \underline{\widehat{\mathbf{e}}}_{\mathrm{curl}} + \underline{\widehat{\mathbf{e}}}_{\mathrm{div}}$, where $\widetilde{\mathbf{S}}\mathbf{M}_{\underline{\varepsilon}}\underline{\widehat{\mathbf{e}}}_{\mathrm{curl}} = 0$ and $\mathbf{C}\underline{\widehat{\mathbf{e}}}_{\mathrm{div}} = 0$. Entirely analogous to Eq. 3.9 we have

$$\widetilde{\mathbf{S}}\mathbf{M}_{\underline{\varepsilon}}\widetilde{\mathbf{S}}^{\mathrm{H}}\underline{\varphi} = \underline{\mathbf{q}}_s \tag{4.30a}$$

$$\mathbf{C}^{\mathrm{H}}\mathbf{M}_{\underline{\nu}}\mathbf{C}\underline{\widehat{\mathbf{e}}}_{\mathrm{curl}} - \omega^2\mathbf{M}_{\underline{\varepsilon}}\underline{\widehat{\mathbf{e}}}_{\mathrm{curl}} = \underline{\widehat{\widehat{\mathbf{r}}}} \tag{4.30b}$$

with $\underline{\mathbf{q}}_s = (i/\omega)\widetilde{\mathbf{S}}\underline{\widehat{\widehat{\mathbf{j}}}}_s$ and

$$\underline{\widehat{\widehat{\mathbf{r}}}} = -\omega^2\mathbf{M}_{\underline{\varepsilon}}\mathbf{G}\underline{\varphi} - i\omega\underline{\widehat{\widehat{\mathbf{j}}}}_s, \tag{4.31}$$

which is discretely divergence free, i.e. $\widetilde{\mathbf{S}}\underline{\widehat{\widehat{\mathbf{r}}}} = 0$. The total field is finally obtained by

$$\underline{\widehat{\mathbf{e}}} = -\mathbf{G}\underline{\varphi} + \underline{\widehat{\mathbf{e}}}_{\mathrm{curl}}. \tag{4.32}$$

Equation 4.30a is Hermitian in the absence of conductivity and Eq. 4.30b can be made complex symmetric for purely real reluctivity. However, a Hermitian curl-curl system is obtained only when the material is entirely lossless.

Software

The FIT was implemented using different software packages, see Fig. 4.7 for an overview. The mesh originates from EMS. It is imported to MATLAB® [112] by M2M (Schuhmann *et al.*, TEMF internal) and the material matrices are saved as vectors in ascii files. The main code is written in C++ using Visual Studio® [113]. The format of vectors and matrices is given by the PETSc [114] (Portable, Extensible Toolkit for Scientific computation) package, which also includes LSE solvers and preconditioners.

In order to run a loop over many frequency points, the material matrices have to be imported only once. However, dispersive material needs to be rescaled for every frequency point. Thus, the system matrix and the excitation vector need to be reassembled. The impedance evaluation functional is computed from the source current density and delivers the resulting impedance as ascii file for further processing in MATLAB. The entire solution fields can also be imported in MATLAB and subsequently written back by M2M to EMS for visualization.

It has been experimented with different iterative solvers and preconditioners to improve the solution speed, which particularly required for the 3D computation. The performance of iterative solvers crucially depends on the condition number[6] of the system matrix. For a high condition number, the convergence of iterative solvers becomes slow, or the solver might not converge at all.

The curl-curl equation is usually ill conditioned when different materials are present. In order to search a solution of the curl-curl system only in the space of discretely divergence free functions, the Helmholtz split can be employed. The required solving of the Poisson problem, Eq. 4.30a, is very fast, since conjugate gradient solvers converge in a few iterations for the positive definite matrix in the absence of conductivity. However, the effect on accelerating the solution of the curl-curl problem was found to be small, when employing standard iterative solvers. It has particularly been observed, that the convergence is slow for low frequency and low β. Therefore, in order to obtain a general

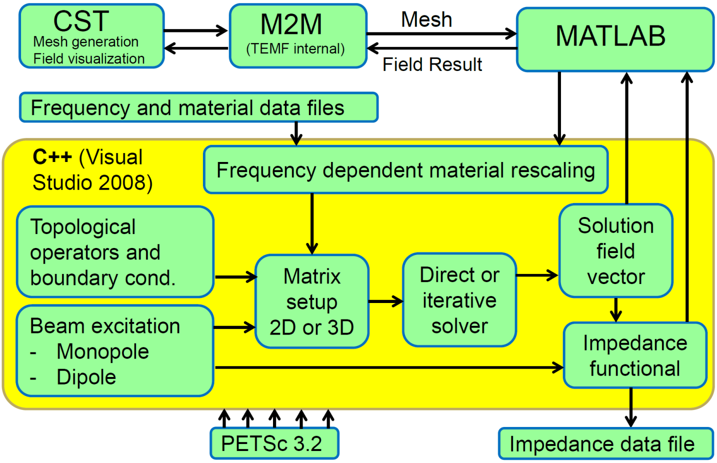

Figure 4.7.: Implementation of the FIT-FD solver for beam coupling impedance.

---

[6] The condition number is defined as $\text{cond}_{||\cdot||}(A) = ||A||||A^{-1}||$ and can be related to the ratio of the largest and smallest eigenvalue when the 2-norm is used.

tool that is applicable for all frequencies, velocities and materials, a direct solver (Lower Upper (LU) decomposition) was employed.

Simulation Results and Discussion

The first example to validate the 2D solver is the same ferrite ring as already treated with PS in Fig. 4.1. The 2D staircase mesh is taken as a cross-section cut from a 3D mesh created by EMS. The longitudinal impedance obtained by the FIT is shown in Fig. 4.8 (crosses), as a comparison to analytical results (thick solid lines) from a field matching algorithm implemented in Mathematica, see [59]. Additionally, also the result from the radial model is plotted. Due to the slow convergence of the FIT on curved boundaries, the results agree only poorly, even for the rather fine mesh (205 × 205) that has been chosen.

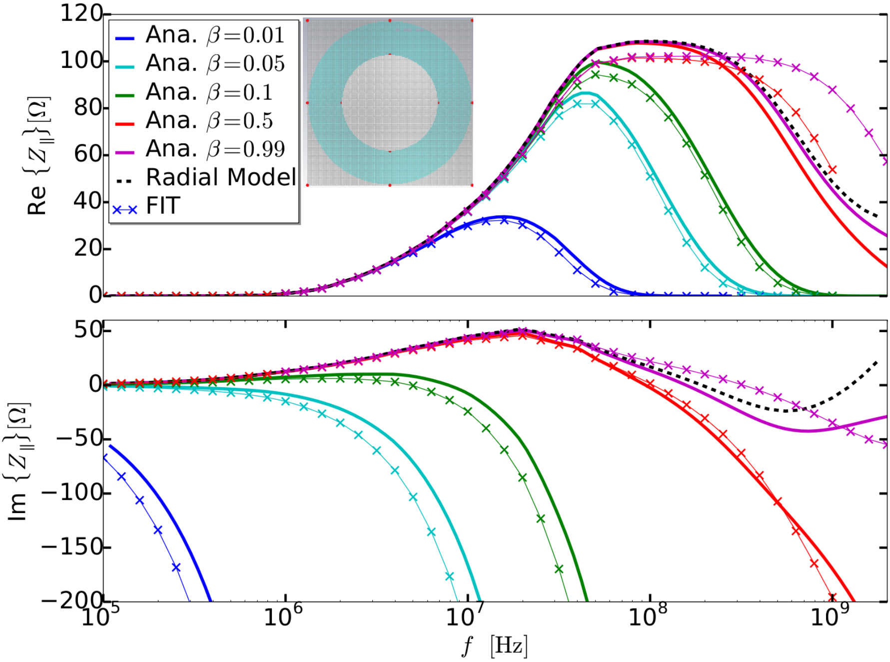

Figure 4.8.: Longitudinal impedance of the ferrite ring from 2D FIT for different β as compared to analytical calculation. The dashed line indicates the result from the radial model.

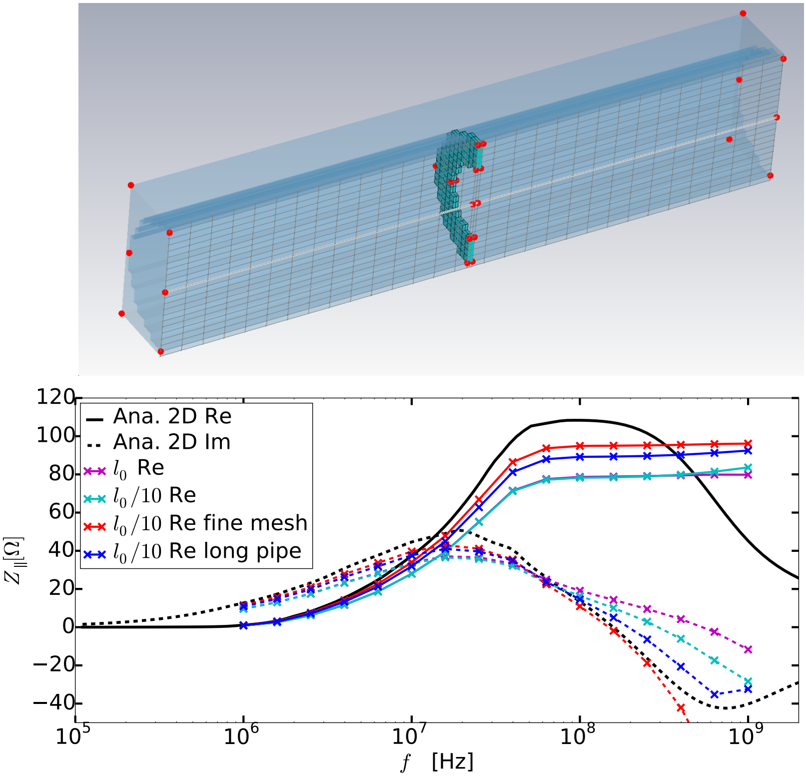

Figure 4.9.: Mesh of the ferrite ring (as in Fig. 4.1 with $l = l_0/10 = 2.54$mm) in the enveloping pipe setup (top) and longitudinal impedance from 3D FIT for $\beta = 1$ (bottom). Solid lined denote real and dashed lines imaginary parts. The red and blue lines show very long pipe stubs and shorter stubs with higher mesh resolution, respectively.

In order to reproduce the results of Fig. 4.1 for the pipe-like structure on the right, which has a strong dependence on the length, 3D computations were performed as depicted in Fig. 4.9. The length of the pipe has to be chosen such that the scattered fields are decayed at the end of the pipe, i.e. a pipe length increase should not change the result. Due to limitations in the computational time, a high mesh resolution and long pipe stubs could not be achieved at the same time. Thus, the results in Fig. 4.9 did not converge to sufficient accuracy. This general problem redirected the focus of this thesis from 3D to 2D computations.

4.2.2 Finite Element Method (FEM)

Since staircase FIT is not suitable to model a dipolar delta-function ring as Eq. 2.54, a twin wire approximation has been used. In order to model such a ring properly, the Finite Element Method (FEM) has significant advantages. Due to the unstructured mesh, arbitrary beam distributions including good approximations to δ-functions can be imprinted. This enables the subtraction of the direct space charge impedance, which is due to the electromagnetic fields within the ring source (see again 3.48). The direct space charge impedance can be obtained from the limit $b \to \infty$ in Eq. 3.47 and reads

$$\underline{Z}^{\text{spch}}_{\perp,\text{direct}} = \frac{ilZ_0}{\beta\gamma^2\pi a^2} \mathrm{I}_1(k_\varrho a)\mathrm{K}_1(k_\varrho a). \tag{4.33}$$

It can be either evaluated analytically and subtracted from the numerical calculation or it can be evaluated numerically. The numerical evaluation of the direct space charge impedance can be done on a very coarse mesh that needs to be identical to the one for the final impedance computation inside the ring and has a large extension outside the ring. Here, we follow the first approach, i.e. the mesh inside the ring is chosen rather fine and the direct space charge impedance is evaluated analytically by Eq. 4.33 and subsequently subtracted.

The finite element method is based on decomposing the computational domain Ω in finite sized subdomains Ω_e, i.e. the elements. A function in an appropriate space can be approximated by a finite basis, such that each element is the support of one basis (ansatz) function. Since such an approximation is (weakly) differentiable only once, a second order PDE has to be brought in a 'weak formulation'. This is obtained by multiplying with all test functions[7] of an appropriate test function space, integrating over the whole domain and transferring one (exterior) derivative by means of partial integration. Finally a LSE is obtained, which has number of ansatz functions as columns and number of test functions as rows.

For simplicity we will only address the 2D beam coupling impedance problem here, i.e. $\Omega \subset \mathbb{R}^2$ being a Lipschitz domain. The electric field $\underline{\vec{E}} : \Omega \to \mathbb{C}^3$ required to determine the coupling impedance is the solution of the curl-curl equation

$$\nabla \times \underline{\nu} \nabla \times \underline{\vec{E}} - \omega^2 \underline{\varepsilon}\, \underline{\vec{E}} = -i\omega \underline{\vec{J}}_s, \tag{4.34}$$

where we assume the material parameters to be constant within each triangular element, see Fig. 4.10. First, we apply a Dirichlet condition $\vec{n} \times \underline{\vec{E}} = 0$. Later, this will be optionally replaced by a metallic SIBC. For a two-dimensional (infinitely long) structure, the Fourier correspondence $\partial_z \to -i\omega/v$ holds, which motivates splitting the electric field as

$$\underline{\vec{E}} = \begin{pmatrix} \underline{\vec{E}}_\perp \\ \underline{E}_z \end{pmatrix}. \tag{4.35}$$

---

[7] In the Galerkin approach, the test functions are identical to the ansatz functions.

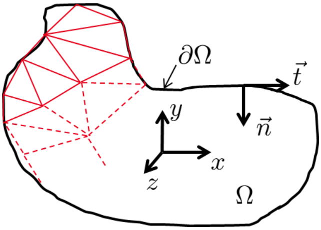

Figure 4.10.: Computational domain for the 2D impedance solver [115].

If the vectorial (transverse) parts of the field would be discretized by nodal finite elements, a jump of the normal field component on a material interface would be impossible. In order to avoid this 'too much continuity' phenomenon, Nédélec edge-elements [116, 117] are used for the discretization of the vector fields.

Since the lowest order Nédélec elements are not suited to compute the divergence of a field, the irrotational part is calculated separately by applying a Helmholtz split $\underline{\vec{E}} = \underline{\vec{E}}_{\text{curl}} + \underline{\vec{E}}_{\text{div}}$ to Eq. 4.35 on the simply connected domain Ω. Thus, the equations to be addressed are again Eqs. 3.9.

As discussed in Eq. 3.8, the continuous fields are elements of their respective Sobolev-spaces. For the 2D setup we choose $\underline{E}_{z,\text{div/curl}} \in \mathscr{H}^1(\Omega)$ and $\underline{\vec{E}}_{\perp,\text{div/curl}} \in \mathscr{H}^{\text{curl}}_{\text{2D}}(\Omega)$, such that they feature the respective properties of the de Rham complex shown in Fig. 4.11. The unidirectional solid arrows denote complete de Rham sequences, i.e. the range of one operator is the kernel of the next.

The same de Rham sequences hold for the discrete fields, provided the function spaces for discrete fields are projections from the continuous function spaces with projection

$$\begin{tikzcd}
\mathscr{H}^1 \arrow[r, "\nabla"] \arrow[rrr, dashed, leftrightarrow, bend left=40, "{\nu,\varepsilon}"] \arrow[drr, "\hat{\mathrm{A}}"] \arrow[ddr, "\nabla_\perp"'] & \mathscr{H}^{\text{curl}} \arrow[r, "\nabla\times"] \arrow[r, dashed, leftrightarrow, bend left=50, "{\nu,\varepsilon}"] \arrow[dd, dotted, leftrightarrow, "\times\mathscr{H}^1"] & \mathscr{H}^{\text{div}} \arrow[r, "\nabla\cdot"] \arrow[d, dotted, leftrightarrow, "\times\mathscr{H}^1"] & \mathscr{L}^2 \\
 & & \mathscr{H}^{\text{div}}_{\text{2D}} \arrow[ur, "\nabla_\perp\cdot"] & \\
 & \mathscr{H}^{\text{curl}}_{\text{2D}} \arrow[ur, dashed, leftrightarrow, "{\nu,\varepsilon,\hat{\mathrm{Z}}}"] \arrow[uurr, "\hat{\mathrm{B}}"'] & &
\end{tikzcd}$$

Figure 4.11.: De Rham diagram for the used operators and function spaces. The operators $\hat{\mathrm{A}} : \mathscr{H}^1(\Omega) \to \mathscr{H}^{\text{div}}_{\text{2D}}(\Omega)$ and $\hat{\mathrm{B}} : \mathscr{H}^{\text{curl}}_{\text{2D}}(\Omega) \to \mathscr{L}^2(\Omega)$ are the 2D vectorial and scalar curl operators, respectively and $\nu, \varepsilon, \hat{\mathrm{Z}}$ are invertible Hodge operators. The 2D spaces are supplemented by $\mathscr{H}^1(\Omega)$ to obtain their 3D z-periodic equivalents.

operators that commute with the exterior derivative (see [118], Theorem 5.6). In this case, the convergence of the projectors implies the convergence of the FEM method.

The functions in $\mathscr{H}^1(\Omega)$ are discretized using first order nodal elements

$$N_k(\xi,\eta) = a_k\xi + b_k\eta + c_k, \tag{4.36}$$

which fulfill

$$N_k(\xi_i,\eta_i) = \delta_{i,k}, \tag{4.37}$$

where i and k are local vertex indices and (ξ,η) are local coordinates. Transformed to the global coordinates (x,y), these elements are a basis of the discrete space $\mathscr{H}_h^1(\Omega)$, where h is the mesh size parameter. For the discretization of $\mathscr{H}_{\mathrm{2D}}^{\mathrm{curl}}(\Omega)$ functions, we employ lowest order Nédélec edge elements of the first kind (see e.g. [116, 119]), obtained from the nodal elements by (see e.g. [120])

$$\vec{w}_i(\xi,\eta) = N_k\nabla_\perp N_l - N_l\nabla_\perp N_k, \tag{4.38}$$

where i,k,l are again local vertex indices. The edge functions $\vec{w}_i$ fulfill

$$\frac{1}{|l_k|}\int_{l_k}\vec{w}_i\cdot\vec{t}_k\mathrm{d}s = \delta_{i,k} \tag{4.39}$$

with $\vec{t}_k$ being the tangential unit vector of edge l_k, which is located at the opposite of node k. Transformed to the global coordinates (x,y), the functions in Eq. 4.38 are a basis of the reduced space $\{\vec{u}\in\mathscr{H}_{\mathrm{2D}h}^{\mathrm{curl}} : \nabla_\perp\cdot\vec{u} = 0\}$, where the divergence operator is to be understood in the discrete weak sense.

Source Terms and Impedance Evaluation

The source current (Eq. 2.64) at $z=0$ is projected on the nodal functions by writing it in the $\mathscr{H}_h^1(\Omega)$-basis as

$$\sigma(x,y) = \sum_{i=1}^{N_\mathrm{n}} a_i N_i(x,y). \tag{4.40}$$

The coefficients a_i are obtained by multiplying with N_j, integrating, and solving the positive definite system for the 'mass-matrix'

$$\mathbf{M}_{ij} = \int_\Omega N_iN_j\mathrm{d}\Omega. \tag{4.41}$$

Practically, this can be done with a conjugate gradient solver, which converges quickly for the positive definite matrix.

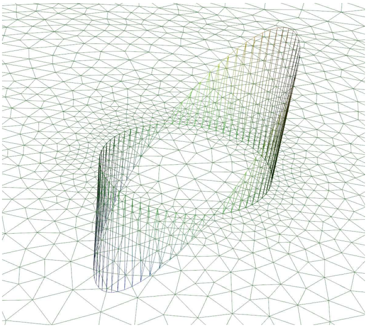

Figure 4.12.: Dipole source term $\sigma(x, y)$ in arbitrary units.

For the dipolar terms, the δ-function in Eq. 2.54 will always be smeared out over a mesh cell. This error can be minimized by adapting the mesh such that a triangular representation of the δ-function,

$$\begin{aligned}\delta_\xi(x-x_0) = \frac{1}{s^2}&\left[(\Theta(x-(x_0-\xi))-\Theta(x-x_0))(x-(x_0-\xi))\right.\\ &\left.-(\Theta(x-x_0)-\Theta(x-(x_0+\xi)))(x-(x_0+\xi))\right],\end{aligned} \tag{4.42}$$

is achieved, with $\xi \ll a$ being the width of the triangle. Note that $\delta_\xi \in \mathscr{L}^2(\Omega)$ while $\delta \notin \mathscr{L}^2(\Omega)$. A plot of this source term can be seen in Fig. 4.12. The smear-out error can be estimated by calculating the dipole moment of a source (Eq. 2.54) represented on the mesh by Eq. 4.42, i.e.

$$\int_\Omega \sigma_{d_x,\xi} x \mathrm{d}x \mathrm{d}y = q d_x \left(1 + \frac{1}{6}\frac{\xi^2}{a^2}\right). \tag{4.43}$$

An optimal choice of the parameter ξ is a trade-off between geometrical representation of the δ-function, where it should be chosen small, and avoiding small angles in the mesh, which deteriorates the condition number of the system matrix.

The impedance functionals Eqs. 2.66 and 2.69 are evaluated by inserting the discretizations of $\underline{E}_z$ and $\underline{J}_z$. One obtains a linear form involving the mass matrix Eq. 4.41,

$$\underline{Z}_\parallel = -\frac{l}{q^2}\sum_{j,k=1}^{N_n} \underline{\mathbf{a}}_k^{\mathrm{H}} \mathbf{M}_{jk} \underline{\mathbf{e}}_j = -\frac{l}{q^2}\mathbf{a}^{\mathrm{H}}\mathbf{M}\mathbf{e}, \tag{4.44}$$

with e_j being the nodal coefficients of the total longitudinal electric field and l being the length of the structure. The transverse impedance is evaluated accordingly, with normalization to the numerically integrated dipole moment according to Eq. 4.43.

Software

The implementation is done using the open source finite element toolbox FEniCS [121][8]. It provides a mathematical framework to work with function spaces that have been created on the mesh. A function in such a space is represented by a coefficient vector and basis functions which are available in the function space. Thus, basis changes, i.e. projections to other function spaces are possible. Likewise, other operators as e.g. partial differentiation, integration, or interpolation can be applied on discrete functions as if they were continuous.

FEniCS supports different programming languages, mainly C++ and Python. For simplicity, Python was chosen here, as it allows to have a complete framework from the mesh import to the final impedance result plot. Inside FEniCS, the Python source code is compiled just in time (JIT) to obtain C++ code that runs a powerful linear algebra backend such as PETSc [114]. FEniCS does not provide complex numbers, but coupled function spaces are available. This means that the degrees of freedom of multiple (even nested) function spaces can be summarized in one function space. Thus, complex functions need to be split in real and imaginary parts which are individual members of a coupled function space, which however leads to to very lengthy equations. Therefore the following notation

$$\underline{x} = x^{\mathrm{r}} + i x^{\mathrm{i}} \tag{4.45}$$

is adopted to write the lengthy equations as brief as possible.

The 2D mesh employed for FEM impedance calculation originates from GMSH [122] and it is imported using DOLFIN-CONVERT [123]. Since only open source software is involved, the hereby presented Python code 'BeamImpedance2D' [124] is published as well. A detailed description of the algorithm and further examples are published in [115]. The following two sections describe the solver, before validation results are presented.

Poisson Solver

The coupled Poisson system Eq. 3.9a is rewritten in 2D as

$$\begin{aligned}
-\nabla_\perp \cdot \varepsilon_0 \varepsilon_r \nabla_\perp \Phi^{\mathrm{r}} + \frac{\omega^2 \varepsilon_0 \varepsilon_r}{\beta^2 c^2} \Phi^{\mathrm{r}} - \nabla_\perp \cdot \frac{\kappa}{\omega} \nabla_\perp \Phi^{\mathrm{i}} + \frac{\omega \kappa}{\beta^2 c^2} \Phi^{\mathrm{i}} &= \varrho_s^{\mathrm{r}} \\
-\nabla_\perp \cdot \varepsilon_0 \varepsilon_r \nabla_\perp \Phi^{\mathrm{i}} + \frac{\omega^2 \varepsilon_0 \varepsilon_r}{\beta^2 c^2} \Phi^{\mathrm{i}} + \nabla_\perp \cdot \frac{\kappa}{\omega} \nabla_\perp \Phi^{\mathrm{r}} - \frac{\omega \kappa}{\beta^2 c^2} \Phi^{\mathrm{r}} &= 0.
\end{aligned} \tag{4.46}$$

It is solved by means of the standard Galerkin procedure, i.e. testing the real and imaginary parts of the equation separately with N_j and integration by parts to obtain

---

[8] See also the textbook [119] for a detailed description.

the weak formulation, which is subsequently discretized by inserting the ansatz function representation of $\underline{\Phi}$. Thus, the algebraic equations for the real and imaginary coefficients of $\underline{\Phi}$ are treated separately. Exemplary, the first 'stiffness' term reads

$$-\int_{\Omega} N_j \nabla_{\perp} \cdot \varepsilon \nabla_{\perp} \Phi^{\mathrm{r}} \mathrm{d}\Omega = \int_{\Omega} \nabla_{\perp} N_j \cdot \varepsilon \nabla_{\perp} \Phi^{\mathrm{r}} \mathrm{d}\Omega + \int_{\partial\Omega} N_j \vec{n} \cdot \varepsilon \nabla_{\perp} \Phi^{\mathrm{r}} \mathrm{d}s \tag{4.47}$$

with a vanishing boundary term for perfectly electric and also for a metallic surface impedance boundary condition. The first stiffness and mass matrices are

$$(\mathbf{S}_{\varepsilon}^{\mathrm{rr}})_{ij} = \int_{\Omega} \varepsilon_0 \varepsilon_r \nabla_{\perp} N_i \cdot \nabla_{\perp} N_j \mathrm{d}\Omega. \tag{4.48}$$

$$(\mathbf{M}_{\varepsilon}^{\mathrm{rr}})_{ij} = \frac{\omega^2}{\beta^2 c^2} \int_{\Omega} \varepsilon_0 \varepsilon_r N_i N_j \mathrm{d}\Omega. \tag{4.49}$$

such that the whole system becomes

$$\begin{bmatrix} \mathbf{S}_{\varepsilon}^{\mathrm{rr}} + \mathbf{M}_{\varepsilon}^{\mathrm{rr}} & \mathbf{S}_{\kappa}^{\mathrm{ri}} + \mathbf{M}_{\kappa}^{\mathrm{ri}} \\ \mathbf{S}_{\kappa}^{\mathrm{ir}} + \mathbf{M}_{\kappa}^{\mathrm{ir}} & \mathbf{S}_{\varepsilon}^{\mathrm{ii}} + \mathbf{M}_{\varepsilon}^{\mathrm{ii}} \end{bmatrix} \begin{bmatrix} \varphi^{\mathrm{r}} \\ \varphi^{\mathrm{i}} \end{bmatrix} = \begin{bmatrix} \varrho_s^{\mathrm{r}} \\ 0 \end{bmatrix}. \tag{4.50}$$

After solving Eq. 4.50, the irrotational electric field is obtained by $\vec{E}^{\mathrm{r}}_{\perp,j} = (\Phi^{\mathrm{r}}_{k'} - \Phi^{\mathrm{r}}_{k})\vec{t}_j / l_j$, where k and k' are the nodes attached to the edge l_j. It is projected, in the same manner as for the source, on the $\mathscr{H}^{\mathrm{curl}}_{2\mathrm{D}h}(\Omega)$ basis. Together with $E^{\mathrm{r}}_z = -\frac{\omega}{\beta c}\Phi^{\mathrm{i}}$ and the respective imaginary parts, the source term for the curl-curl solver, Eq. 3.10, is assembled.

Curl-Curl solver and Surface Impedance Boundary Condition

Recalling the notation in Eq. 2.72 and invoking $\partial_z \to -i\omega/v$ we have $\hat{Z}_{3\mathrm{D}} = \partial_z \vec{e}_z \times = -i\omega/v \vec{e}_z \times$ and

$$\hat{\mathrm{Z}}^2 = \frac{\omega^2}{\beta^2 c^2} \hat{\mathrm{I}}. \tag{4.51}$$

The curl-curl term in Eq. 3.9 is rewritten as

$$\nabla \times \underline{\nu} \nabla \times \underline{\vec{E}} = \begin{pmatrix} \hat{\mathrm{A}} \underline{\nu} \hat{\mathrm{B}} + \underline{\nu} \hat{\mathrm{Z}}^2 & \hat{Z} \underline{\nu} \hat{\mathrm{A}} \\ \hat{\mathrm{B}} \underline{\nu} \hat{\mathrm{Z}} & \hat{B} \underline{\nu} \hat{\mathrm{A}} \end{pmatrix} \begin{pmatrix} \underline{\vec{E}}_{\perp} \\ \underline{E}_z \end{pmatrix}. \tag{4.52}$$

which after splitting real and imaginary parts allows testing $\vec{E}^{\mathrm{r}}_{\perp}, \vec{E}^{\mathrm{i}}_{\perp}, E^{\mathrm{r}}_z, E^{\mathrm{i}}_z$ independently with $\vec{w}^{\mathrm{r}}_k, \vec{w}^{\mathrm{i}}_k, v^{\mathrm{r}}_k, v^{\mathrm{i}}_k$. After integrating by parts, one obtains a bilinear form, i.e. the curl-curl 'stiffness' matrix.

The $\mathbb{R}^3$ vectoranalytical identity $\nabla \times (\Phi\vec{w}) = \Phi\nabla \times \vec{w} - \vec{w} \times \nabla\Phi$ and Stokes' theorem imply for functions $\varphi : \Omega \to \mathbb{R}$ and $\vec{u} : \Omega \to \mathbb{R}^2$

$$\int_\Omega \varphi(\hat{\mathrm{B}}\vec{u})\mathrm{d}\Omega = \int_\Omega \vec{u}(\hat{\mathrm{A}}\varphi)\mathrm{d}\Omega - \int_{\partial\Omega} \varphi\vec{u}\cdot\vec{t}\mathrm{d}s, \tag{4.53}$$

where $\vec{t} = \vec{e}_z \times \vec{n}$ is the tangential unit vector at the boundary. For the second order operators in Eq. 4.52 follows

$$\int_\Omega (\hat{\mathrm{A}}\nu^{\mathrm{r}}\hat{\mathrm{B}}\vec{E}^{\mathrm{r}}_{\perp})\cdot\vec{w}^{\mathrm{r}}_j\mathrm{d}\Omega = \int_\Omega (\nu^{\mathrm{r}}\hat{\mathrm{B}}\vec{E}^{\mathrm{r}}_{\perp})(\hat{\mathrm{B}}\vec{w}^{\mathrm{r}}_j)\mathrm{d}\Omega + \int_{\partial\Omega} (\nu^{\mathrm{r}}\hat{\mathrm{B}}\vec{E}^{\mathrm{r}}_{\perp})\vec{w}^{\mathrm{r}}_j\cdot\vec{t}\mathrm{d}s \tag{4.54}$$

$$\int_\Omega (\hat{\mathrm{B}}\nu^{\mathrm{r}}\hat{\mathrm{A}}E^{\mathrm{r}}_z)v^{\mathrm{r}}_j\mathrm{d}\Omega = \int_\Omega (\nu^{\mathrm{r}}\hat{\mathrm{A}}E^{\mathrm{r}}_z)\cdot(\hat{\mathrm{A}}v^{\mathrm{r}}_j)\mathrm{d}\Omega - \int_{\partial\Omega} v^{\mathrm{r}}_j(\nu^{\mathrm{r}}\hat{\mathrm{A}}E^{\mathrm{r}}_{\mathrm{z}})\cdot\vec{t}\mathrm{d}s. \tag{4.55}$$

The boundary terms vanish in case of a Dirichlet boundary condition, i.e. a PEC surface.

In order to include a SIBC, the magnetic field is calculated from Faraday's law as

$$i\hat{\mathrm{Z}}\underline{E}_{\mathrm{t}} + \hat{\mathrm{A}}\underline{E}_{\mathrm{z}} = -i\omega\mu\underline{H}_{\mathrm{t}} = -i\omega\mu\underline{Y}_{\mathrm{s}}\underline{E}_{\mathrm{z}} = \underline{k}^{(\mathrm{Z})}\underline{E}_{\mathrm{z}} \tag{4.56}$$

$$\hat{\mathrm{B}}\underline{E}_{\mathrm{t}} = -i\omega\mu\underline{H}_{\mathrm{z}} = -i\omega\mu\underline{Y}_{\mathrm{s}}\underline{E}_{\mathrm{t}} = \underline{k}^{(\mathrm{Z})}\underline{E}_{\mathrm{t}}, \tag{4.57}$$

with the index t denoting the boundary tangential projection and the abbreviation $\underline{k}^{(\mathrm{Z})} = -i\omega\mu/\underline{Z}_s$. Finally the boundary integrals in Eqs. 4.54 and 4.55 read

$$\int_{\partial\Omega} (\nu^{\mathrm{r}}\hat{\mathrm{B}}\vec{E}^{\mathrm{r}}_{\perp})\vec{w}^{\mathrm{r}}_j\cdot\vec{t}\mathrm{d}s = \int_{\partial\Omega} \nu^{\mathrm{r}}(\underline{k}^{(\mathrm{Z})}\underline{\vec{E}}_{\perp}\cdot\vec{t})^{\mathrm{r}}(\vec{w}^{\mathrm{r}}_j\cdot\vec{t})\mathrm{d}s \tag{4.58}$$

$$\int_{\partial\Omega} v^{\mathrm{r}}_j(\nu^{\mathrm{r}}\hat{\mathrm{A}}E^{\mathrm{r}}_{\mathrm{z}})\cdot\vec{t}\mathrm{d}s = \int_{\partial\Omega} v^{\mathrm{r}}_j\nu^{\mathrm{r}}(\underline{k}^{(\mathrm{Z})}\underline{E}_{\mathrm{z}})^{\mathrm{r}}\mathrm{d}s, \tag{4.59}$$

plus the respective imaginary parts. Note that the $\hat{\mathrm{Z}}\underline{E}_{\mathrm{t}}$ term is normal to the boundary and therefore vanishes.

The discretization of Eq. 3.9b is finally

$$\left[\mathbf{S}_{\mathrm{curlcurl}} + \mathbf{M}_{\underline{\varepsilon}} + \mathbf{M}_{\mathrm{SIBC}}\right]\mathbf{e}_{\mathrm{curl}} = \mathbf{r} \tag{4.60}$$

where the solution vector and the matrices are arranged as

$$\mathbf{e}_{\text{curl}} = \begin{bmatrix} \mathbf{e}_{\perp}^{\text{r}} \\ \mathbf{e}_{\perp}^{\text{i}} \\ \mathbf{e}_{\text{z}}^{\text{r}} \\ \mathbf{e}_{\text{z}}^{\text{i}} \end{bmatrix}, \qquad \mathbf{S}_{\text{curlcurl}} = \begin{bmatrix} \mathbf{S}_{\perp\perp}^{\text{rr}} & \mathbf{S}_{\perp\perp}^{\text{ir}} & \mathbf{S}_{\text{z}\perp}^{\text{rr}} & \mathbf{S}_{\text{z}\perp}^{\text{ir}} \\ \mathbf{S}_{\perp\perp}^{\text{ri}} & \mathbf{S}_{\perp\perp}^{\text{ii}} & \mathbf{S}_{\text{z}\perp}^{\text{ri}} & \mathbf{S}_{\text{z}\perp}^{\text{ii}} \\ \mathbf{S}_{\perp\text{z}}^{\text{rr}} & \mathbf{S}_{\perp\text{z}}^{\text{ir}} & \mathbf{S}_{\text{zz}}^{\text{rr}} & \mathbf{S}_{\text{zz}}^{\text{ir}} \\ \mathbf{S}_{\perp\text{z}}^{\text{ri}} & \mathbf{S}_{\perp\text{z}}^{\text{ii}} & \mathbf{S}_{\text{zz}}^{\text{ri}} & \mathbf{S}_{\text{zz}}^{\text{ii}} \end{bmatrix},$$

$$\mathbf{M}_{\underline{\varepsilon}} = \begin{bmatrix} \mathbf{M}_{\varepsilon\perp}^{\text{rr}} & \mathbf{M}_{\kappa\perp}^{\text{ir}} & 0 & 0 \\ \mathbf{M}_{\kappa\perp}^{\text{ri}} & \mathbf{M}_{\varepsilon\perp}^{\text{ii}} & 0 & 0 \\ 0 & 0 & \mathbf{M}_{\varepsilon\text{z}}^{\text{rr}} & \mathbf{M}_{\kappa\text{z}}^{\text{ir}} \\ 0 & 0 & \mathbf{M}_{\kappa\text{z}}^{\text{ri}} & \mathbf{M}_{\varepsilon\text{z}}^{\text{ii}} \end{bmatrix}, \qquad \mathbf{M}_{\text{SIBC}} = \begin{bmatrix} \mathbf{D}_{\perp}^{\text{rr}} & \mathbf{D}_{\perp}^{\text{ir}} & 0 & 0 \\ \mathbf{D}_{\perp}^{\text{ri}} & \mathbf{D}_{\perp}^{\text{ii}} & 0 & 0 \\ 0 & 0 & \mathbf{T}_{\text{z}}^{\text{rr}} & \mathbf{T}_{\text{z}}^{\text{ir}} \\ 0 & 0 & \mathbf{T}_{\text{z}}^{\text{ri}} & \mathbf{T}_{\text{z}}^{\text{ii}} \end{bmatrix}. \tag{4.61}$$

For example, we spell out the terms

$$(\mathbf{S}_{\perp\perp}^{\text{rr}})_{i,j} = \int_{\Omega} \Big[(\nu^{\text{r}} \hat{\text{B}} \vec{w}_i^{\text{r}})(\hat{\text{B}} \vec{w}_j^{\text{r}}) - \nu^{\text{r}} \hat{\text{Z}}^2 \vec{w}_i^{\text{r}} \cdot \vec{w}_j^{\text{r}} \Big] \text{d}\Omega \tag{4.62a}$$

$$(\mathbf{M}_{\varepsilon\perp}^{\text{rr}})_{i,j} = -\omega^2 \int_{\Omega} \varepsilon \vec{w}_i^{\text{r}} \cdot \vec{w}_j^{\text{r}} \text{d}\Omega \tag{4.62b}$$

$$(\mathbf{D}_{\varepsilon\perp}^{\text{rr}})_{i,j} = \int_{\partial\Omega} \nu^{\text{r}} \underline{k}^{\text{r}} \vec{w}_i^{\text{r}} \cdot \vec{w}_j^{\text{r}} \text{d}s \tag{4.62c}$$

$$(\mathbf{T}_{\varepsilon\perp}^{\text{rr}})_{i,j} = -\int_{\partial\Omega} \nu^{\text{r}} \underline{k}^{\text{r}} v_i^{\text{r}} v_j^{\text{r}} \text{d}s. \tag{4.62d}$$

When lowest order elements are used, the number of DoFs in the LSE Eq. 4.60 is $2 \cdot (\#\text{nodes} + \#\text{edges})$. In the presence of different materials it is usually ill conditioned and therefore solved with a direct solver, i.e. standard LU decomposition or MUMPS (MUltifrontal Massively Parallel Sparse direct Solver).

Simulation Results and Discussion

As a first example, we revisit again the ferrite ring as already addressed in TD in Fig. 4.1 and by FD-FIT in Fig. 4.8. The longitudinal impedance curves are visible in Fig. 4.13, where also the triangular mesh from GMSH is depicted. The agreement of the simulation results with the analytical prediction is quite good, nonetheless, at low β slight discrepancies in the imaginary part are visible. This can be explained by insufficient mesh density, since all the curves in Fig. 4.13 have been computed on the same mesh. However, as predicted by Eq. 3.12, very low beam velocity requires a higher transverse mesh density.

The proper representation of the source allows also a proper computation of the space charge impedance. Figure 4.14 shows the longitudinal space charge impedance for circular beam in circular pipe as depicted in Fig. 3.10. The analytical results are the

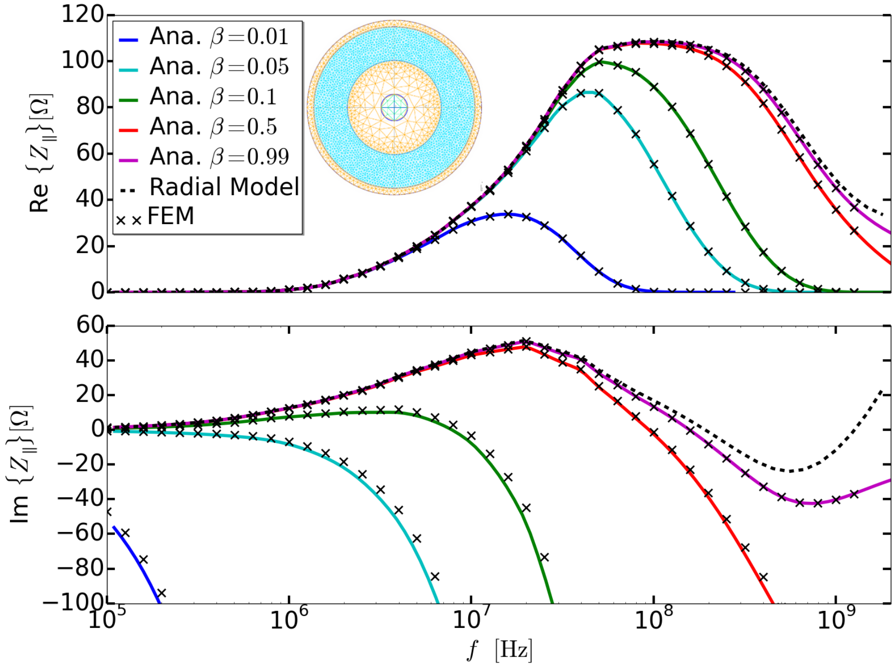

Figure 4.13.: Comparison (FEM vs. analytical) of the longitudinal impedance of the ferrite ring for different beam velocity. Additionally, the black dashed line shows an analytical calculation using the radial model.

same as already discussed in Fig. 3.11. As visible in Fig. 4.14, the agreement between the analytical and numerical curves is excellent for all frequencies.

For the transverse space charge impedance, Fig. 4.15 shows the numerical results compared to the analytical predictions already made in Fig. 3.13. The agreement for the full transverse impedance is satisfactory, but for the indirect part, the agreement is good only below the cut-off frequency. This is due to the fact that the indirect transverse space charge impedance quickly vanishes above the cutoff (cf. Eq. 3.49), but the numerical error, which is in the range of $1-10\%$, remains.

The next example is a thin resistive circular beam pipe. The geometry and the impedance in a wide frequency range are shown in Fig. 4.16. At low frequency, i.e. $f < f_{\mathrm{skin}}$, the resistive wall needs to be resolved by the mesh (resolved wall (RW) curve). For $f > f_{\mathrm{skin}}$, the mesh consisting of two layers of triangles in the thickness d, cannot resolve the skin depth anymore. Therefore the RW results deviate from the analytically expected ones. However, the surface impedance boundary condition can be employed above f_{skin}, which gives accurate results up to extremely high frequencies.

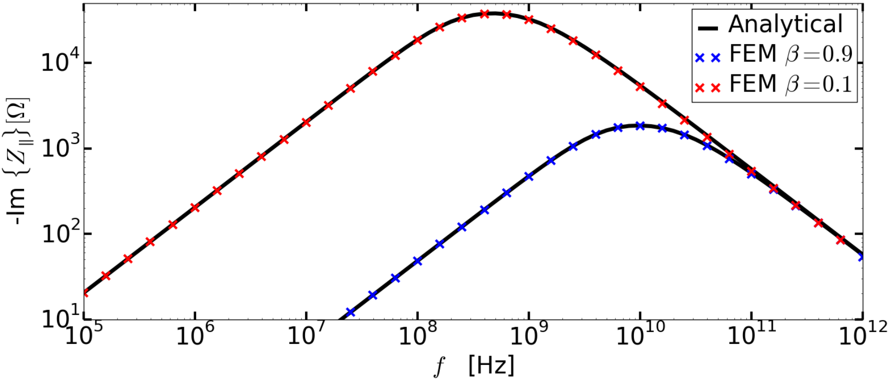

Figure 4.14.: Longitudinal space charge impedance for the setup in Fig. 3.10.

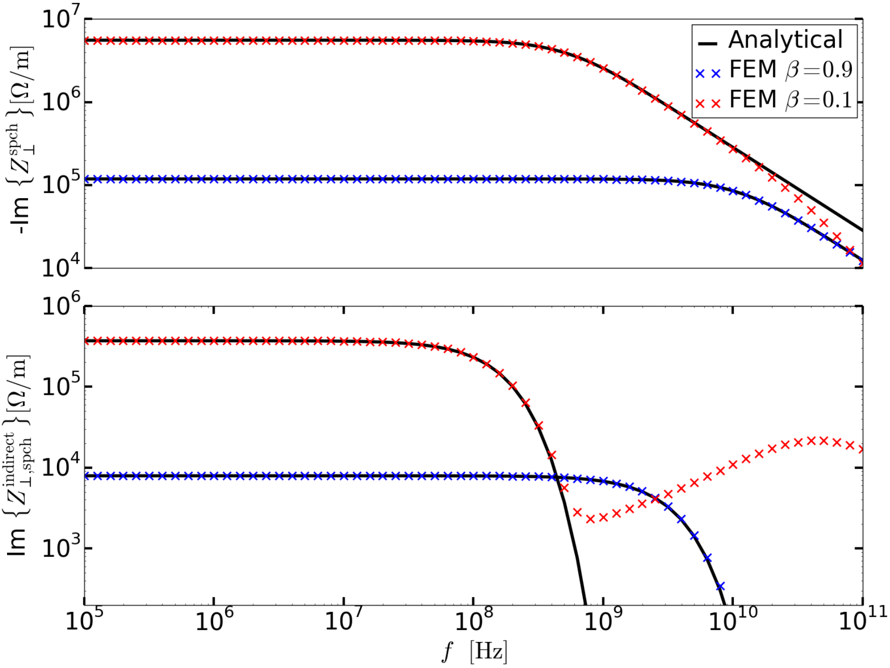

Figure 4.15.: Transverse space charge impedance for the setup in Fig. 3.10. The lower plot shows the indirect part of the space charge impedance, which vanishes at the cut-off frequency. For the FEM calculation, the numerical error remains.

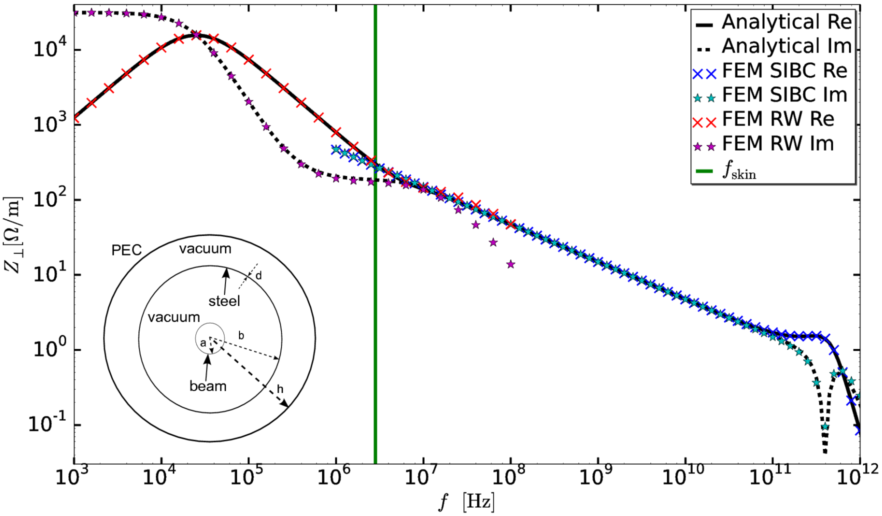

Figure 4.16.: Transverse impedance of the thin beam pipe with radius $b = 4\,\mathrm{cm}$, thickness $d = 0.3\,\mathrm{mm}$, outer boundary radius $h = 1\,\mathrm{m}$, length $l = 1\,\mathrm{m}$, conductivity $\kappa = 1\,\mathrm{MS/m}$ and $\beta = 0.999999$. The analytical curve originates from Rewall [50]. At low frequencies, the resistive wall is resolved by the mesh (RW-marks, red and magenta), while at high frequency the surface impedance boundary condition was applied (SIBC-marks, blue and cyan).

BeamImpedance2D is also applied to a first design of the beam pipe for the FCC-hh, within the FCC design study [7]. As depicted in Fig. 4.17, the pipe has a slit, in order to allow synchrotron radiation to escape the inner vacuum. There are two cooling capillaries attached on the outside, which supposedly convey all the synchrotron radiation heat power away from the beam pipe. The inner beam screen is made of titanium ($\kappa_0 = 1.8\mathrm{MS}$), coated with a thin layer of copper ($\kappa_0 = 70\mathrm{MS}$) from the inside. The conductivities are assumed to enhance by a factor of 100 due to the cryogenic temperature ($\vartheta = 50\mathrm{K}$). For a simulation of this coating, the two-layer SIBC, i.e. Eq. 3.19, is applied. Figure 4.18 shows the vertical transverse impedance, as compared to an analytical calculation by Rewall [50] for a two-layer cylindrical wall with radius 12mm and 18mm, which are the larger and small semi-axis radii. For this simulation, the value of γ was chosen realistically as 50000, i.e. $\beta \approx 1 - 1/(2\gamma^2) \approx 1 - 2\cdot 10^{-10}$. Due to the high γ and the high conductivity, the impedance becomes very small. Thus, the error of the space charge impedance can prevail over the imaginary part of the resistive wall impedance at high frequency. The discrepancy at low frequency is due to a modeling difference, i.e. in Rewall the real titanium layer thickness was taken and vacuum is behind, whereas the two-layer SIBC assumes the second layer (titanium) as infinitely thick.

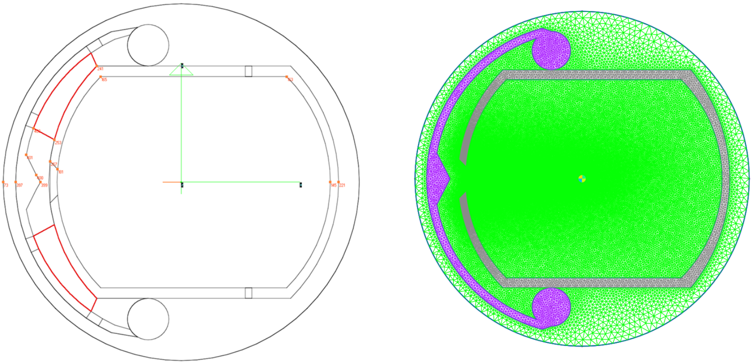

Figure 4.17.: Technical drawing of FCC-hh pipe (R. Kersevan, CERN) and GMSH [122] triangular mesh from [104]. For the SIBC, only the inner vacuum region (green) is meshed.

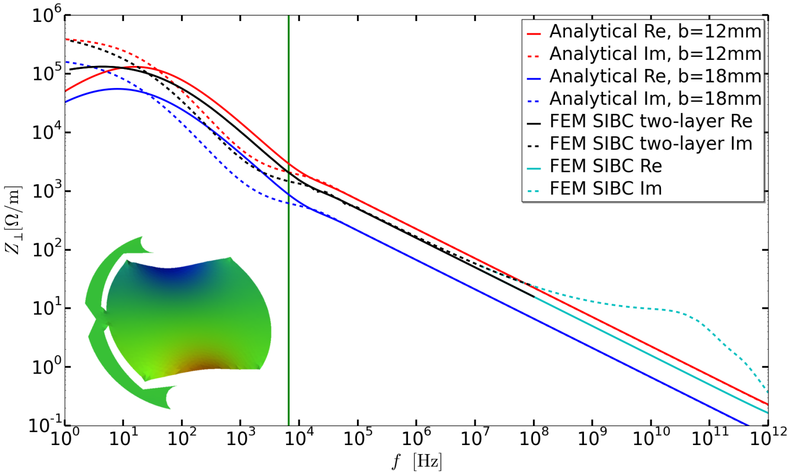

Figure 4.18.: Vertical impedance for the FCC beam pipe as compared to analytical models (Rewall) with the smaller ($b = 12\,\mathrm{mm}$) and larger ($b = 18\,\mathrm{mm}$) semi-axis radius. The vertical green line indicates the frequency at which the skin depth in copper is equal to the layer thickness. As expected, the numerical line is between the two. The bump of the imaginary part at high frequency is a numerical artifact due to inaccurate cancellation of electric and magnetic fields at the very high $\gamma = 50000$.

5 Impedance Bench Measurements

For complicated devices, such as kicker magnets or collimators, impedance simulations need to be confirmed by dedicated measurements. This is also because beam based measurements of coupling impedance can in principle only be done for the whole synchrotron. Techniques to localize the impedance are available, see e.g.[125] or [126], but they require involved beam optics manipulations and the results are rather coarse.

Therefore, in the course of this thesis, a new RF-laboratory has been set up at GSI, which is particularly dedicated to the measurement of beam coupling impedance on the bench, i.e. without beam. In the framework of a hereby supervised MSc thesis, different measurement boxes have been manufactured. Measurements for the SIS-18 kicker magnet have been performed and compared to PS simulations, see [127]. Here, only the principles of the measurement are discussed and validated on simplified examples, as it has also been published in [59]. The main results are the proof of validity of the transmission line formula for distributed impedance and the comparison of the different interpretation formulas for impedance wire measurements. In practice, it was found that in order to gain confidence on measurements, they have to go along with both wake field and microwave simulations.

The electromagnetic field of a single charge approaches the one of a lossless TEM transmission line in the ultrarelativistic limit (cf. Eq. 3.52), i.e.

$$\underline{E}_z = iq\frac{\mu_0}{2\pi}\frac{\omega}{\beta^2\gamma^2}\mathrm{K}_0\left(\frac{\omega}{\beta\gamma c}\varrho\right) \xrightarrow{\gamma\to\infty} 0 \tag{5.1a}$$

$$\frac{1}{\beta}Z_0\underline{H}_\varphi = \underline{E}_\varrho = q\frac{\mu_0}{2\pi}\frac{\omega}{\beta^2\gamma}\mathrm{K}_1\left(\frac{\omega}{\beta\gamma c}\varrho\right) \xrightarrow{\gamma\to\infty} \mathrm{q}\frac{\mathrm{Z}_0}{2\pi\varrho}. \tag{5.1b}$$

This motivates measuring the beam coupling impedance of an accelerator device by replacing the beam by a wire, which has the same TEM source fields as an ultrarelativistic beam. The overall effect of the scattered field (cf. Eqs. 3.53 and 3.55), which causes the impedance for the beam, can be measured by means of Vector Network Analyzer (VNA) measurements of scattering parameters (S-parameters, see App. E) in the wire case.

As visible from Eq. 5.1b, the restriction of the correspondence of the coaxial line technique to ultrarelativistic beams is rather strict, since the wave impedance for a beam is

$$Z_{\text{wave}} = \frac{\underline{E}_\varrho}{\underline{H}_\varphi} = \frac{Z_0}{\beta}, \tag{5.2}$$

and a TEM wave in vacuum has always $Z_{\text{wave}} = Z_0$. Due to this limitation, slow beam simulators [128], where electric and magnetic fields are excited by separate antennas, did not prevail. Thus, one has to rely on analytical or simulation techniques for the β-scaling of beam coupling impedances.

The transmission line measurement technique was introduced by Sands and Rees [129] in order to determine the beam energy loss factors in the TD using a broadband pulse with a similar shape as the particle bunch. Nowadays, modern VNAs allow sweeping a narrow-banded sinusoidal signal, to obtain the impedance directly for a particular frequency range. Especially when particular beam instability sidebands are under investigation, the FD method is advantageous.

In both TD and FD it has to be ensured that artifacts due to the measurement setup do not pollute the measurement result and only the Device Under Test (DUT), as it will be placed in the accelerator, is analyzed. This can be achieved by performing a reference measurement (REF) of an empty measurement box or pipe, such that box reflection errors are purged, i.e. the DUT becomes de-embedded. The de-embedding process was analyzed for lumped impedances by Hahn and Pedersen [130], and generally by Kroyer *et al.* [131]. In order to obtain a reasonable signal quality, the impedance mismatch from the cables to the measurement box must not exceed a certain value. Thus, a matching network is required. For high frequencies, mismatch reflections can also just be disregarded by 'Time Domain Gating' [132], but in order to represent the spectrum of the applied window-function properly, a high bandwidth of the VNA is required. Also, RF-attenuation foam is an opportunity to damp mismatch reflections.

5.1 De-embedding and Matching

The characteristic impedance of a cylindrical coaxial line is given by [133]

$$Z_c = \frac{Z_0}{2\pi} \ln \frac{b}{a}, \tag{5.3}$$

where b and a are the radii of the outer and inner conductor, respectively. Thus, the characteristic impedance of a large box with a thin wire[1] must be very high, i.e., here, in the range of 400Ω. The (generally complex[2]) reflection factor is [133]

$$r = \frac{Z_{c,1} - Z_{c,2}}{Z_{c,1} + Z_{c,2}} \tag{5.4}$$

which is for the transition of the box to a conventional 50Ω line in the range of 80%. Thus, a matching network is required, since otherwise multiple reflections would be in the same range of amplitude as the primary signal. The simplest way to construct a matching network is to use RF-resistors (carbon composite) in a way, that each side sees its own characteristic impedance, e.g. as depicted in Fig. 5.1a. Here, the two resistors

---

[1] The central wire in the coaxial setup must be thin, in order to make sure that most of the field propagates along with the wire, which corresponds to the 'rigid beam approximation'.

[2] In this chapter the underlines are not kept strictly, i.e. all quantities are allowed to be complex.

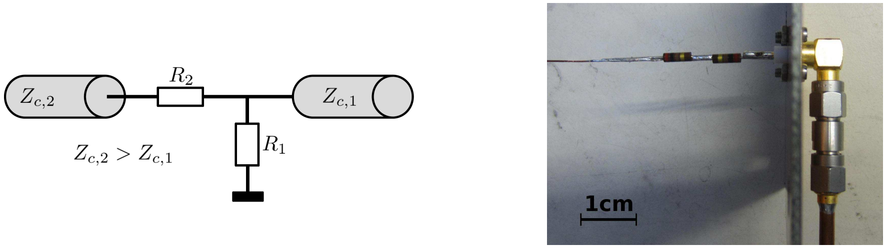

(a) Matching with a simple voltage divider.

(b) Matching with resistors and a 10dB attenuator [59].

Figure 5.1.: Different types of resistive matching.

R_1 and R_2 have to fulfill the two matching conditions

$$\begin{aligned} R_1 \parallel (R_2 + Z_{c,2}) &= Z_{c,1} && (5.5a)\\ R_2 + R_1 \parallel Z_{c,1} &= Z_{c,2}, && (5.5b) \end{aligned}$$

where $x \parallel y = xy/(x+y)$ is the abbreviation for parallel circuits. Unfortunately practical resistors have an inductance, which makes it impossible to fulfill Eqs. 5.5 at higher frequencies in a broadband manner. This can be partly overcome by taking an attenuator instead of R_1. Commercially available attenuators are broadband matched to 50Ω and do not suffer from the inductance problem.

The frequency dependent attenuation and phase shift of the matching network is calibrated out by a reference measurement, such that for an assumed perfect matching the de-embedded transmission is $S_{21}^{\text{de-embed}}(\omega) = S_{21}^{\text{DUT}}(\omega)/S_{21}^{\text{REF}}(\omega)$. Here, only the reflection of the matching network needs to be close to zero, but it is allowed to be lossy, within

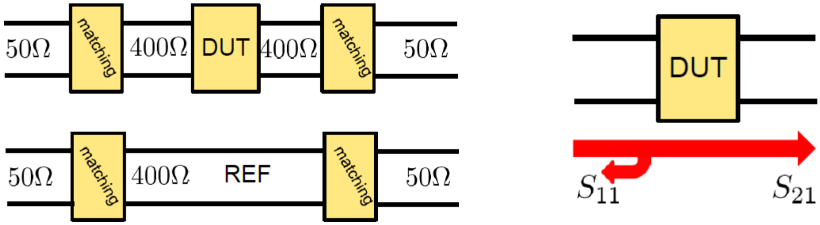

(a) REF measurement in order to de-embed the DUT

(b) Quantities of interest for the de-embedded DUT

Figure 5.2.: De-embedding by subsequent DUT and REF measurements.

Figure 5.3.: Large measurement box with $Z_c = 433 \pm 18\Omega$. The DUT in the bottom picture is a SIS-18 kicker magnet (cf. Fig. 1.3). Courtesy of L. Eidam [127, 59].

the dynamic range of the VNA. The way how S_{21}^{DUT} and S_{21}^{REF} are measured is illustrated in Fig. 5.2. Practical setups for the measurement are shown in Figs. 5.3 and 5.4. Obviously, it is advantageous to have a setup as small as possible, in order to shift the eigenmodes of the box to frequencies as high as possible.

The calibration with open, short, through, and 50Ω is to be done right in front of the matching section. Especially at high frequencies, i.e. above 100 MHz, phase-stable cables are required. Standard SMA cables have been found insufficient. Since precision measurement cables are very expensive and were not available, a good compromise

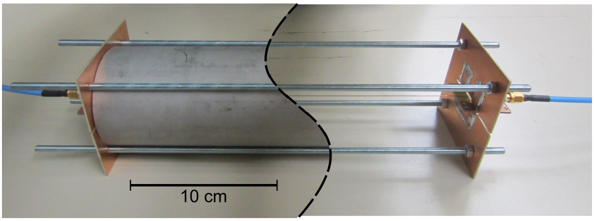

Figure 5.4.: Small measurement box with $Z_c = 299 \pm 12\Omega$. Courtesy of L. Eidam [127, 59].

was found by using semi-rigid SMA cables. The once calibrated semi-rigid cables do not change their shape between DUT and REF measurements anymore and also their temperature drift is acceptable.

5.2 Lumped vs. Distributed Impedance

There is a crucial difference between the beam and the wire setup: the TEM wave experiences an attenuation, which is not negligible and actually the quantity to be measured by the S_{21}-parameter. Thus, lumped (short) and distributed (long) impedances require different interpretation of the measured S_{21} parameters. Mathematically, lumped and distributed impedances can be identified by their distribution along the z-axis, i.e.

$$\frac{\partial Z_{\parallel}^{\mathrm{lumped}}(\omega,z)}{\partial z} = Z_{\parallel}^{\mathrm{total}}(\omega)\delta(z-z_0) \tag{5.6a}$$

$$\frac{\partial Z_{\parallel}^{\mathrm{dist}}(\omega,z)}{\partial z} = \frac{Z_{\parallel}^{\mathrm{total}}(\omega)}{l}. \tag{5.6b}$$

In a real accelerator components, there is always a mixture of both. The impedance discontinuity (geometric impedance) at the beginning of the DUT is always lumped, while the body of the DUT (resistive wall) is often almost equally distributed.

The modeling of lumped impedances is just a localized impedance element in longitudinal direction, while distributed impedances can be represented by a TEM-line with an impedance element $Z_{\parallel}/l$ equally distributed to each infinitely short transmission line element, see Fig. 5.5. We call a device a lumped (distributed) impedance if $Z^{\mathrm{lumped}} \gg Z^{\mathrm{dist}}$ ($Z^{\mathrm{lumped}} \ll Z^{\mathrm{dist}}$). Often lumped (distributed) impedances are characterized by $\Theta_z \ll 1$ ($\Theta_z \gg 1$), but as it has been exemplary shown in Fig. 4.1, this is not a sufficient criterion. If the ferrite ring with $l = l_0$, i.e. a fixed Θ_z, can be treated as a lumped or a distributed impedance, depends also on the housing structure.

The scattering matrices for the de-embedded DUT are given by [133, 134]

$$\mathbf{S}^{\mathrm{lump}} = \frac{1}{2Z_c^{\mathrm{REF}} + Z^{\mathrm{lump}}} \begin{pmatrix} Z^{\mathrm{lump}} & 2Z_c^{\mathrm{REF}} \\ 2Z_c^{\mathrm{REF}} & Z^{\mathrm{lump}} \end{pmatrix} \tag{5.7}$$

(a) Lumped impedance **(b)** Distributed impedance

Figure 5.5.: Different modeling approaches for the de-embedded accelerator component as depicted in Fig. 5.2b: the lumped impedance is a lumped element of length zero and the distributed impedance is a transmission line of length l and characteristic impedance Z_c^{DUT}.

$$\mathbf{S}^{\mathrm{dist}} = \frac{\begin{pmatrix} (Z_c^{\mathrm{DUT}^2} - Z_c^{\mathrm{REF}^2})\sin(k_z^{\mathrm{DUT}} l) & -2iZ_c^{\mathrm{DUT}} Z_c^{\mathrm{REF}} \\ -2iZ_c^{\mathrm{DUT}} Z_c^{\mathrm{REF}} & (Z_c^{\mathrm{DUT}^2} - Z_c^{\mathrm{REF}^2})\sin(k_z^{\mathrm{DUT}} l) \end{pmatrix}}{(Z_c^{\mathrm{DUT}2} + Z_c^{\mathrm{REF}2})\sin(k_z^{\mathrm{DUT}} l) - 2iZ_c^{\mathrm{DUT}} Z_c^{\mathrm{REF}} \cos(k_z^{\mathrm{DUT}} l)} \tag{5.8}$$

for the lumped and distributed impedance, respectively. How to conclude from the measured S-parameters to the DUT impedance will be discussed for lumped and distributed impedances in the following subsections.

5.2.1 Distributed Impedance Measurement

In transmission line theory, a ladder replacement circuit model as shown in Fig. 5.6 can be derived. Here, L_0', C_0', and R_0' are inductance, capacitance, and resistance per length, respectively. The distributed beam coupling impedance can be seen as an additional longitudinal element $Z_{||}/l$. From the transmission line parameters the propagation con-

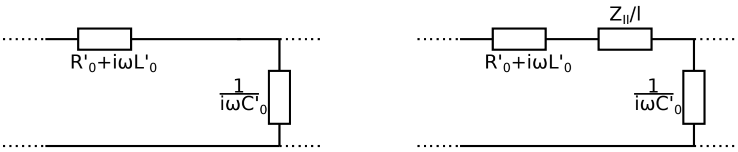

(a) REF **(b)** DUT

Figure 5.6.: Transmission line replacement circuit for distributed impedance. Courtesy of L. Eidam [127].

stants and characteristic impedances can be calculated as [133]

$$k_z^{\mathrm{DUT}} = \omega\sqrt{C_0' L_0'}\sqrt{1 - i\frac{R_0' + Z_{\parallel}/l}{\omega L_0'}} \tag{5.9a}$$

$$k_z^{\mathrm{REF}} = \omega\sqrt{C_0' L_0'}\sqrt{1 - i\frac{R_0'}{\omega L_0'}} \tag{5.9b}$$

$$Z_c^{\mathrm{DUT}} = \sqrt{\frac{R_0' + i\omega L_0' + Z_{\parallel}/l}{i\omega C_0'}} \tag{5.9c}$$

$$Z_c^{\mathrm{REF}} = \sqrt{\frac{R_0' + i\omega L_0'}{i\omega C_0'}} \approx \sqrt{\frac{L_0'}{C_0'}} =: Z_c. \tag{5.9d}$$

This system can be solved for $Z_{\parallel}$ as

$$Z_{\parallel}^{\mathrm{coax}} = iZ_c^{\mathrm{REF}} l \cdot (k_z^{\mathrm{DUT}} - k_z^{\mathrm{REF}}) \cdot \left(1 + \frac{k_z^{\mathrm{DUT}}}{k_z^{\mathrm{REF}}}\right). \tag{5.10}$$

Since the DUT setup is a combination of three transmission lines (cf. Fig. 5.5), obtaining the propagation constants can be involved, when a reflection takes place at the DUT. When this reflection is small, i.e. $Z_c^{\mathrm{DUT}} \simeq Z_c^{\mathrm{REF}}$, Eq. 5.8 simplifies to

$$S_{21} = S_{12} = e^{-ik_z l}\ ,\ S_{11} = S_{22} = 0, \tag{5.11}$$

which can be easily inverted. Otherwise a reflection corrected S_{21} parameter can be introduced, which is by definition

$$S_{21}^{\mathrm{C}} := e^{-ik_z l}. \tag{5.12}$$

The new S_{21}^{C} parameter can be obtained by solving Eq. 5.8 for k_z, which can be achieved through replacing sine and cosine by exponentials. The hereby derived quadratic equation for S_{21}^{C} is called Wang-Zhang-formula [135],

$$(S_{21}^{\mathrm{C}})^2 + \frac{S_{11}^2 - S_{21}^2 - 1}{S_{21}} S_{21}^{\mathrm{C}} + 1 = 0 \tag{5.13}$$

where only one of the two solutions, that fulfills $|S_{21}^{\mathrm{C}}| < 1$, is physical. Solving Eq. 5.13 requires the knowledge of the S_{11}-parameter, which is in practice difficult to measure due to multiple reflections between the DUT and the matching section (cf. Fig. 5.2). Nonetheless, S_{11} can be determined easily in simulations with waveguide ports.

The wavenumber k_z is found from the complex logarithm of either the original (Eq. 5.11) or the corrected (Eq. 5.12) S_{21}-parameter. It can be inserted into Eq. 5.10 to obtain [134]

$$Z_{\|}^{\mathrm{coax}} = Z_c \cdot \ln\left(\frac{S_{21}^{\mathrm{REF}}}{S_{21}^{\mathrm{DUT}}}\right) \cdot \left[1 + \frac{\ln(S_{21}^{\mathrm{DUT}})}{\ln(S_{21}^{\mathrm{REF}})}\right] \tag{5.14}$$

which is called 'improved-log-formula'[3] in the literature. This formula is exact for ideally distributed impedances, but it does not apply to lumped impedances, since the replacement circuit in Fig. 5.6 requires many such transmission line elements in succession. The dependence on the electrical length of the reference $\Theta_{\mathrm{z}}^{\mathrm{REF}} = k_{\mathrm{z}}^{\mathrm{REF}} l = \omega l/c$ can be pointed out explicitly by rewriting Eq. 5.14 as [137]

$$Z_{\|}^{\mathrm{coax}} = Z_c \cdot \ln\left(\frac{S_{21}^{\mathrm{REF}}}{S_{21}^{\mathrm{DUT}}}\right) \cdot \left[2 + \frac{i}{\Theta_{\mathrm{z}}^{\mathrm{REF}}} \ln\left(\frac{S_{21}^{\mathrm{DUT}}}{S_{21}^{\mathrm{REF}}}\right)\right]. \tag{5.15}$$

This formula contains only the logarithm of the ratio, i.e. the difference term in Eq. 5.10. Besides the implicit dependence of k_z^{DUT} on l, the $\ln(S_{21}^{\mathrm{DUT}}/S_{21}^{\mathrm{REF}})$-term is linear in l. Thus, for distributed impedances, the square bracket in Eq. 5.15 does not depend on the length explicitly.

When inserting the lumped impedance S-parameters (Eq. 5.7) into the improved-log-formula (Eq. 5.14 or 5.15) one observes that the second term in the bracket is not independent of the length anymore, i.e. Θ_z does not cancel. This shows explicitly the inapplicability of the improved-log-formula to lumped impedances since the length is not defined for lumped impedances. In other words, if a differentially short transmission line element is assigned a finite impedance value (lumped impedance) and this is integrated over a finite length, then the result must diverge.

5.2.2 Lumped Impedance Measurement

The determination of lumped impedances is significantly simpler than the one for distributed impedances, since the reflection does not influence the transmission measurement result. In fact, the reflection can even be used as an alternative method to determine a lumped impedance. However, Hahn and Pedersen argued [130], that the reflection method is inferior to the transmission method.

From solving Eq. 5.7 for Z^{lump} one obtains the so-called Hahn-Pedersen lumped impedance formula [130],

$$Z_{\|,\mathrm{HP}}^{\mathrm{lump}} = 2Z_c \frac{S_{21}^{\mathrm{REF}} - S_{21}^{\mathrm{DUT}}}{S_{21}^{\mathrm{DUT}}}. \tag{5.16}$$

---

[3] Historically, first the lumped element formulas [129, 130], then the simplified transmission line formula 'Log-formula' [136] and finally the full transmission line formula 'Improved Log-formula' [134] were derived.

In modern VNA's this impedance measurement formula is already built-in, i.e. the impedance can be directly displayed for the simplified case $S_{21}^{\mathrm{REF}} = 1$. Equation 5.16 is an improvement of the original Sands-Rees pulse-energy-loss formula [129] (see also [138])

$$Z_{\parallel,\mathrm{SR}}^{\mathrm{lump}} = 2Z_c \frac{S_{21}^{\mathrm{REF}} - S_{21}^{\mathrm{DUT}}}{S_{21}^{\mathrm{REF}}}. \tag{5.17}$$

Note that there is no theoretical limit on the impedance magnitude for the determination of purely lumped impedances. A proof, that the measured lumped impedance converges to the beam impedance for decreasing wire radius, is outlined in [139].

5.2.3 Mixed Impedance Measurement

Both the lumped (Hahn-Pedersen) and the distributed (improved-log) formulas apply only to their respective types of impedance and give incorrect results for the other. However, practical accelerator components consist of both types, and it is impossible to disentangle them. Thus, a transmission line measurement interpretation formula is required, that applies to both. Such a formula is the (Walling-) log-formula [136],

$$Z_{\parallel}^{\log} = 2Z_c \cdot \ln\left(\frac{S_{21}^{\mathrm{REF}}}{S_{21}^{\mathrm{DUT}}}\right), \tag{5.18}$$

which is obtained from Eq. 5.15 by neglecting the second term in the square bracket. The requirement for this neglect can be conveniently expressed as

$$\frac{k_{\mathrm{z}}^{\mathrm{DUT}}}{k_{\mathrm{z}}^{\mathrm{REF}}} = \frac{Z_c^{\mathrm{DUT}}}{Z_c^{\mathrm{REF}}} \approx 1, \tag{5.19}$$

i.e. the log-formula is valid if the presence of the DUT does not change the characteristic impedance significantly. Contrariwise, it must be invalid for a long distributed device causing a large attenuation, i.e. a large distributed impedance.

The systematic error of the log-formula for distributed impedances can be quantified by solving it for the logarithm and inserting into Eq. 5.15. The thereby obtained quadratic equation

$$Z_{\parallel}^{\mathrm{coax}} = Z_{\parallel}^{\log} + \frac{Z_{\parallel}^{\log^2}}{4i\Theta_{\mathrm{z}}^{\mathrm{REF}} Z_c} \tag{5.20}$$

has the two solutions

$$Z_{\parallel}^{\log} = 2i\Theta_{\mathrm{z}} Z_c \left(-1 \pm \sqrt{1 + \frac{Z_{\parallel}^{\mathrm{coax}}}{i\Theta_{\mathrm{z}}^{\mathrm{REF}} Z_c}}\right). \tag{5.21}$$

Only the positive solution is physical and gives the length independent error estimate

$$\frac{Z_{\parallel}^{\log}}{Z_{\parallel}^{\text{coax}}} = 1 + \frac{i}{4}\frac{Z_{\parallel}^{\text{coax}}}{\Theta_{\text{z}}^{\text{REF}} Z_c} - \frac{1}{8}\left(\frac{Z_{\parallel}^{\text{coax}}}{\Theta_{\text{z}}^{\text{REF}} Z_c}\right)^2 + \ldots\ , \tag{5.22}$$

which agrees with Hahn's estimate [140] to first order.

The systematic error of the log-formula (Eq. 5.18) for lumped impedance can be estimated by inserting the lumped impedance S-parameters (Eq. 5.7),

$$Z_{\parallel}^{\log} = -2Z_c \ln \frac{1}{1 + \frac{Z^{\text{lump}}}{2Z_c}}. \tag{5.23}$$

Taylor expansion results in

$$\frac{Z_{\parallel}^{\log}}{Z^{\text{lump}}} = 1 - \frac{1}{2}\frac{Z^{\text{lump}}}{2Z_c} + \frac{1}{3}\left(\frac{Z^{\text{lump}}}{2Z_c}\right)^2 - \ldots \tag{5.24}$$

i.e. the log-formula reproduces lumped impedances, for $Z^{\text{lump}} \ll 2Z_c$.

Finally, one can conclude that the log formula is valid for both lumped and distributed impedance, provided the lumped part does not exceed the characteristic impedance of the REF, and the distributed part does not change the characteristic impedance significantly. Obviously, this is true for a small impedance magnitude.

5.3 Analytical Calculation of the Quasi-TEM Eigenmode

In order to benchmark the wire measurement method, we wish to derive the relevant eigenmode in a cylindrically symmetric structure analytically. The general eigenvalue equation for Maxwell's equations and spatially constant material parameters in particular subdomains reads

$$\frac{1}{\underline{\varepsilon}}\nabla \times \frac{1}{\underline{\mu}}\nabla \times \underline{\vec{E}} = \omega^2 \underline{\vec{E}}. \tag{5.25}$$

Assuming a structure which is homogeneous in z-direction (2D) and a wave that propagates as $e^{-ik_z z}$, we find the equation

$$(\Delta_{\perp} + \omega^2 \underline{\mu}\underline{\varepsilon})\underline{E}_{\text{z}} = k_{\text{z}}^2 \underline{E}_{\text{z}} \tag{5.26}$$

for the eigenvalue k_z, which is the propagation constant for the mode being entirely described by the eigenfunction $\underline{E}_z$. Note that such a description is valid only in the lossy case, since the lossless TEM-mode has $\underline{E}_z = 0$ and subsequently another ansatz is required to determine the fields. For a circularly symmetric setup as depicted in Fig. 5.7,

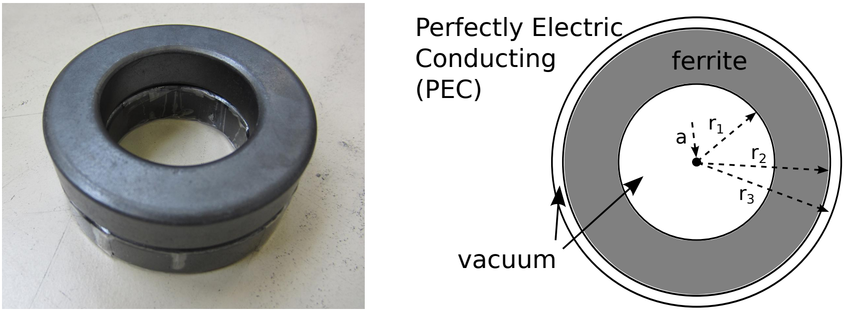

Figure 5.7.: Cylindrically symmetric ferrite ring example with material data as in Fig. 3.3. Dimensions: $r_1 = 1.78\,\mathrm{cm}$, $r_2 = 3.05\,\mathrm{cm}$, $r_3 = 3.3\,\mathrm{cm}$, $l_0 = 2.54\,\mathrm{cm}$. Courtesy of L. Eidam [59, 127]

the solution of Eq. 5.26 can be constructed from the fundamental system of ordinary Bessel functions, which reads for the quasi-TEM mode as

$$\underline{E}_z(\varrho,z) = \begin{cases} 0 & r < a \\ \underline{A}\left(\mathrm{J}_0(k_\varrho \varrho) - \frac{\mathrm{J}_0(k_\varrho a)}{\mathrm{N}_0(k_\varrho a)}\mathrm{N}_0(k_\varrho \varrho)\right) e^{-ik_z z} & a \le r < r_1 \\ \left(\underline{B}_1 \mathrm{J}_0(k_\varrho^{\mathrm{F}} \varrho) + \underline{B}_2 \mathrm{N}_0(k_\varrho^{\mathrm{F}} \varrho)\right) e^{-ik_z z} & r_1 \le r < r_2 \\ \underline{C}\left(\mathrm{J}_0(k_\varrho \varrho) - \frac{\mathrm{J}_0(k_\varrho r_3)}{\mathrm{N}_0(k_\varrho r_3)}\mathrm{N}_0(k_\varrho \varrho)\right) e^{-ik_z z} & r_2 \le r \le r_3. \end{cases} \tag{5.27}$$

Again, as in Eq. 3.6, the dispersion relation $k_\varrho^2 + k_z^2 = \omega^2 \underline{\mu\varepsilon}$ holds and k_ϱ and $\underline{\mu\varepsilon}$ are different in each subdomain, but k_z must be the same everywhere. Thus, $k_\varrho = \sqrt{\omega^2 \underline{\mu\varepsilon} - k_z^2}$ can be replaced in the argument of the Bessel functions and we are left with 5 unknowns, i.e. $\underline{A}, \underline{B}_1, \underline{B}_2, \underline{C}, k_z$. The matching of the tangential electric and magnetic field,

$$\underline{E}_z|_{r_i+} = \underline{E}_z|_{r_i-} \tag{5.28a}$$

$$\underline{H}_\varphi|_{r_i+} = \underline{H}_\varphi|_{r_i-}, \tag{5.28b}$$

where the magnetic field is connected to the radial derivative of the electric field by[4]

$$\underline{H}_\varphi(\varrho,z) = -\frac{i\omega\underline{\varepsilon}}{k_\varrho^2}\partial_\varrho \underline{E}_z(\varrho,z), \tag{5.29}$$

provides 4 conditions. Finally, we are allowed to choose an arbitrary value for the mode amplitude which we take to be $\underline{A}$ (eigenfunction scaling). Note that $\underline{B}_1$,$\underline{B}_2$, and $\underline{C}$

---

[4] This can be obtained by rearranging Maxwell's equations component by component.

scale linearly with $\underline{A}$, but k_z is amplitude independent in linear material. When all the matching conditions are assembled together, a nonlinear equation for k_z remains. This equation can be assembled symbolically and solved numerically using Mathematica. Finally the transmission factor in an infinitely long 2D structure can be obtained from k_z by Eq. 5.11. The impedances resulting from this transmission will be discussed in the next section.

This way of calculating the quasi-TEM eigenmode will be used to show that the improved-log-formula recovers the beam impedance resulting from the surface impedance (cf. Eq. 3.17)

$$Z_\mathrm{s}(\omega) = -\frac{\underline{E}_z(b)}{\underline{H}_\varphi(b)} \tag{5.30}$$

accurately, for frequencies below cutoff and in the limit of vanishing wire radius. The radius b, on which the surface impedance is evaluated, should be chosen such that the characteristic impedance is given by Eq. 5.3. For the longitudinal electric field between the wire and the surface impedance the ansatz (cf. 5.27)

$$\underline{E}_z(r) = \underline{A}\left(\mathrm{J}_0(k_\varrho \varrho) - \frac{\mathrm{J}_0(k_\varrho a)}{\mathrm{N}_0(k_\varrho a)}\mathrm{N}_0(k_\varrho \varrho)\right) \tag{5.31}$$

with the amplitude $\underline{A}$ holds. Calculating the magnetic field by Eq. 5.29 implies the eigenvalue equation for the surface impedance

$$Z_\mathrm{s}(\omega) = \frac{k_\varrho}{i\omega\varepsilon}\,\frac{\mathrm{J}_0(k_\varrho b) - \frac{\mathrm{J}_0(k_\varrho a)}{\mathrm{N}_0(k_\varrho a)}\mathrm{N}_0(k_\varrho b)}{\mathrm{J}_0'(k_\varrho b) - \frac{\mathrm{J}_0(k_\varrho a)}{\mathrm{N}_0(k_\varrho a)}\mathrm{N}_0'(k_\varrho b)}. \tag{5.32}$$

This equation cannot be solved analytically, but an asymptotic expansion for small $\xi = k_\varrho a$ with $\chi = b/a$ yields

$$Z_\mathrm{s}(\omega) = \frac{k_\varrho}{i\omega\varepsilon_0}\left(\chi\,\xi\ln(\chi) + \mathcal{O}(|\xi|^3)\right) = \frac{k_\varrho}{i\omega\varepsilon}\left(k_\varrho b\ln(b/a) + \mathcal{O}(|k_\varrho a|^3)\right). \tag{5.33}$$

The improved-log-formula as given by Eq. 5.10 can be rewritten using the dispersion relation as

$$Z_\parallel^\mathrm{coax} = -iZ_c l\,\frac{k_\varrho^2}{\omega/c}. \tag{5.34}$$

Inserting Eqs. 5.3 and 5.33 into the latter implies for the impedance measured by the improved-log-formula

$$Z_\parallel^\mathrm{coax} = \frac{l}{2\pi b}\left[Z_\mathrm{s} + \frac{k_\varrho}{i\omega\varepsilon}\mathcal{O}(|k_\varrho a|^3)\right]. \tag{5.35}$$

Thus, the imroved-log-formula impedance converges to the beam impedance of an ultrarelativistic beam (cf. Eq. 3.59) below the cutoff frequency in the limit $a \to 0$. Nonetheless, the convergence is rather slow, since k_ϱ increases for smaller wire radius (k_ϱ is always bounded), see Fig. 5.8 (right). In the same way, the log-formula can be proven by inserting its justification $k_\varrho^2 = (\omega/c)^2 - k_z^2 \approx 2\omega/c(\omega/c - k_z)$ into Eq. 5.33.

5.4 Analytical and Numerical Benchmarking of the Wire Measurement

The different formulas for the conversion of S-parameters to longitudinal impedance can be benchmarked by analytical (2D) and numerical (3D) analysis of the measurement setup for the ferrite ring depicted in Fig. 5.7. The 2D setup is an idealized purely distributed impedance, whereas the realistic 3D setup contains a combination of lumped and distributed impedances. Here, only the real parts of the discussed impedances are shown. A full discussion including the plots for the imaginary parts, can be found in [59]. In Fig. 5.8, the infinitely long (2D) setup is investigated by comparison of analytically calculated beam impedance compared to impedance from the different conversion formulas for semi-analytically calculated S-parameters (from the eigenvalue problem). Due to the entirely distributed impedance of the 2D setup, only the improved-log-formula gives appropriate results. On the right hand side, it is shown that the improved-log-formula impedance converges to the beam impedance, but the convergence is rather slow. Even for an extremely small wire radius, a visible error remains. In practice, for a wire radius of $a_0 = 0.225\,\text{mm}$, this error is in the range of 15%.

The same analysis can be performed in 3D with numerically obtained impedances and S-parameters. A handy tool to calculate S-parameters is CST Microwave Studio® [40] (MWS). Figure 5.9 shows the comparison for the different formulas with S-parameters

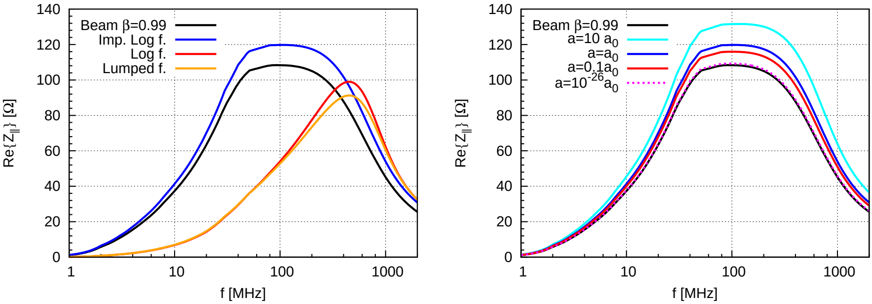

Figure 5.8.: Real impedance from analytically calculated S-parameters with different formulas vs. analytically calculated beam impedance for the 2D model (left) and convergence of the improved-log-formula impedance for decreasing wire radius a, where $a_0 = 0.225\text{mm}$ (right).

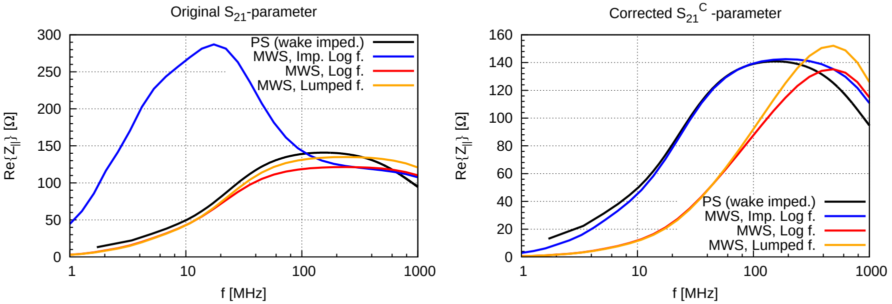

Figure 5.9.: 3D S-parameter simulation with MWS and different conversion formulas vs. impedance from wakefield simulation by PS. The two plots show the real part of the impedance for original and corrected S_{21}-parameters. Note the different vertical axis scalings, the black line (PS) is the same in both plots.

from MWS and beam impedance from PS. The left plot shows the impedance curves from the original S_{21}-parameter, where the improved-log-formula shows a strong unphysical peak, which can be accounted to the reflection at the DUT. However, the lumped and log-formulas give decent results, as one would expect for this rather short DUT. The right plot shows the impedances from the reflection corrected S_{21}^{C}-parameter, which was obtained by solving the Wang-Zhang-formula, Eq. 5.13. Here one can see that the impedance from the improved-log-formula is accurate, whereas the others are unphysically shifted.

5.5 Practical Measurement Evaluation

The ferrite ring depicted in Fig. 5.7 was also measured in the laboratory. The measurement was performed in the two measurement boxes as depicted in Fig. 5.3 and Fig. 5.4, where the S-parameters were recorded by a Rohde&Schwarz ZNB4 [141] VNA (9 kHz-4.5 GHz). The DUT measurement was performed between two averaged REF measurements, in order to obtain the REF signal at the time of the DUT measurement and thus reduce the temperature drift.

The imperfect matching leads to multiple reflections, where the dominating ones are depicted in Fig. 5.10. Therefore, the measured S-parameters show a ripple. For the REF measurement, the maxima of the ripple corresponds to constructive interference. Subsequently, the values of the maxima are roughly the same as they would be in the absence of reflections, and one can coarsely approximate S_{21}^{REF} by linear interpolation between these maxima.

For the DUT measurement, the dominating parasitic reflections are between the DUT and the matching section. Thus the interferences depend on the distance between the

(a) Dominating parasitic reflection for the REF.

(b) Dominating parasitic reflections for the DUT.

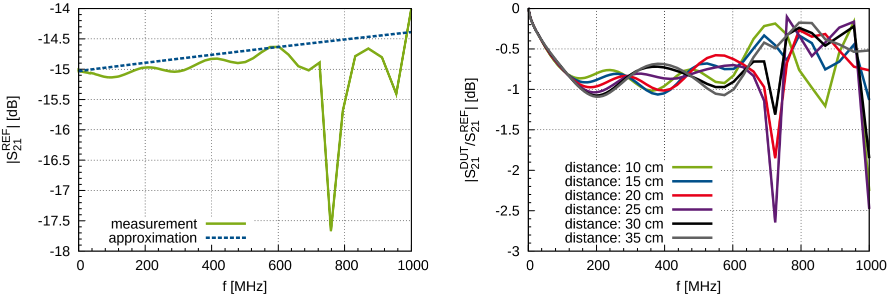

(c) Magnitude of the REF signal and constructive interference approximation.

(d) De-embedded S_{21} for different longitudinal positions of the DUT.

Figure 5.10.: Dominating parasitic reflections (top) and measured S_{21}-parameters for the ferrite ring in the large measurement setup in Fig. 5.3. The notch at ≈ 700MHz corresponds to the first HOM cutoff. Courtesy of L. Eidam [59].

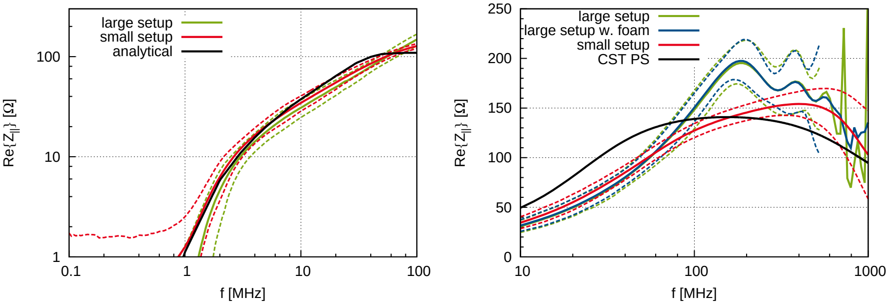

Figure 5.11.: Wire measurements with log-formula vs. analytical (2D) at LF (left) and vs. PS-simulation (3D) at HF (right), performed in the small and large setups (Figs. 5.3 and 5.4), respectively. Additionally, the blue line shows the result in the large setup with RF-attenuation foam to damp mismatch reflections. The dashed lines are error bars. Courtesy of L. Eidam [59].

DUT and the matching sections. They can be significantly diminished by averaging the measurements over many longitudinal positions.

The measurement results are depicted in Fig. 5.11, where at LF (left) the analytic (2D) field-matching result and at HF (right) a PS computation were employed as reference results. At LF the agreement is reasonably good, whereas at HF discrepancies occur. These discrepancies can be accounted to multiple reflections and higher order mode propagation in the large setup. As visible in the plot by comparison of the blue and green lines, one resoncance could be damped by using RF-attenuation foam at the end plates of the box. As expected, the agreement is better for the small setup (red line). Apart from the measurement errors, the remaining discrepancy can also be accounted to the error in the material data for the PS simulation and their fitting to an impulse response model.

5.6 Transverse Impedance

Since the transverse impedance can be measured in a similar manner as the longitudinal one, only the different aspects are reported. There are two principal methods to measure the transverse impedance: the displaced wire method and the twin wire method. In order to enhance the extremely small signals in the twin wire method at low frequencies, it can be extended to the coil method, which requires a quasi-stationary interpretation.

5.6.1 Displaced Wire Method

The displaced wire technique is based on measuring the dipolar longitudinal impedance and using the Panofsky-Wenzel theorem (more precisely the FT of Eq. A.4) to obtain the transverse impedance. In a structure with x and y symmetry, the dipolar longitudinal impedance has a quadratic dependence on the transverse offset from the center (see e.g. [81]). It can be measured in the same way as the monopolar longitudinal impedance, but with a displaced wire. Subsequently, a parabola can be fitted on the measured results for each frequency point at different transverse positions [142]. However, since a displaced wire measures both the driving and detuning impedance, the driving impedance in one plane can only be obtained if the detuning impedance vanishes, i.e. in a structure that is invariant under 90° rotation [36]. For rectangular structures, the detuning impedance can be canceled by measuring the impedance in both horizontal and vertical planes and adding the two, but this yields only the sum of both driving impedances. Therefore, the displaced wire technique is inferior to the twin wire technique for measuring the dipolar transverse driving impedance in general non-symmetric structures and we will only discuss the twin wire technique in detail.

5.6.2 Twin Wire Method

The setup is the same as for the longitudinal impedance, but with two symmetrically driven wires on the differential TEM mode. The characteristic impedance (REF) for the differential TEM mode, i.e. the voltage between the two conductors divided by the current in one conductor, is given by (cf. [143])

$$Z_c^{\text{dip}} = \frac{Z_0}{\pi} \ln\left(\frac{d + \sqrt{d^2 - a^2}}{a} \cdot \frac{b^2 - d\sqrt{d^2 - a^2}}{b^2 + d\sqrt{d^2 - a^2}} \right) \tag{5.36}$$

where a is the wire radius, b is outer shield radius and $2d = \Delta$ is the wire distance. With respect to this characteristic impedance, symmetric S-parameters can be defined. The symmetric S_{21}-parameter can be measured best with a 4-port VNA, which internally converts the 4×4 S-matrix to a 2×2 matrix for the symmetric signals. There are also approaches to use splitters and combiners with a 2-port VNA, but the limited bandwidth of those components makes the calibration (after the hybrids) an involved endeavor. For a 4-port VNA the calibration plane can just be chosen before the matching section (as for the single wire measurement) and the 18 calibration steps (open, short, match, through) can be significantly eased by using an auto-cal kit.

The twin wire approximation provides for the ultrarelativistic dipolar transverse impedance (cf. Eq. 2.68 and Eq. 4.24)

$$Z_\perp(\omega) \approx \frac{c}{\omega \Delta^2} \delta Z_\parallel(\omega) = \frac{c}{\omega \Delta^2} \cdot 2 Z_c^{\text{dip}} \frac{S_{21,\text{dip}}^{\text{REF}} - S_{21,\text{dip}}^{\text{DUT}}}{S_{21,\text{dip}}^{\text{DUT}}}, \tag{5.37}$$

where $\delta Z_\parallel$ is the impedance obtained by the conversion formula Eq. 5.16 for the differential mode S_{21} parameter and characteristic impedance Z_c^{dip}.

As visible in Fig. 5.12, the S_{21}-parameters show much smaller magnitude and phase deviations (to REF) for the dipole mode than for the monopole mode. Therefore, the major difficulty in the dipolar measurement is the poor Signal-to-Noise Ratio (SNR), especially at low frequency (note the extremely small values of $S_{21}^{\text{dip}} < 10^{-6}$ dB at 1 MHz). However, this small signal allows all conversion formulas to be linearized, i.e. they agree with Eq. 5.16. Thus, one does not have to distinguish between lumped and distributed impedance in the twin wire measurement.

A comparison of the transverse impedance from wake field and S-parameter simulation for the ferrite ring is shown in Fig. 5.13. The agreement between the two is reasonably good, except at low frequency, where the computational accuracy is insufficient. The same is visible also for the lab measurement, as plotted in Fig. 5.14. Since the DUT alters the EM-fields only slightly in the twin wire measurement, the dominating parasitic reflections are the same for DUT and REF measurements. Thus, they are almost entirely removed by the de-embedding. However, since the difference between DUT and REF measurement is so small, temperature drifts and noise are the main issues. The temperature drift can be reduced by taking metal film resistors instead of carbon resistors for the matching network, which have a higher inductance but a smaller temperature coefficient. The thereby enlarged mismatch is less critical than the temperature drift for the twin wire measurement. The noise can be reduced by averaging many subsequent DUT and REF measurements.

As visible in Fig. 5.14, the result for the ferrite ring in both the large and the small measurement setup is reasonably good at medium and high frequency. However, at LF the method becomes impracticable. This can be improved by employing the coil method instead of the twin wire method.

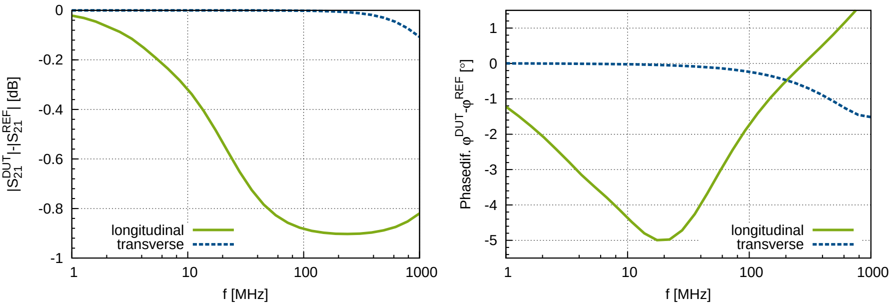

Figure 5.12.: S-parameters for the monopole and dipole TEM mode (simulation). At LF the transverse signal becomes extremely small, i.e. $-3.1 \cdot 10^{-7}$ dB and $3.7 \cdot 10^{-5}$ deg at 1 MHz. Courtesy of L. Eidam [59].

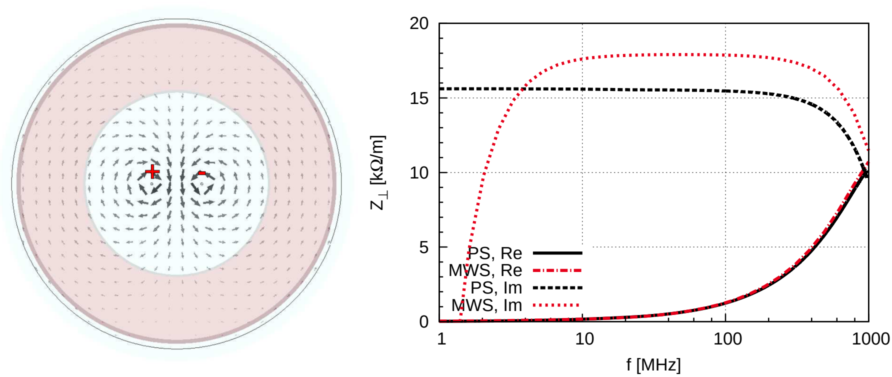

Figure 5.13.: Magnetic field of dipole TEM eigenmode obtained by the multi-pin-portmode-solver. The wire distance is $\Delta = 10$ mm with an uncertainty of 10% for the measurement. The plot shows the impedance from S-parameter simulation (MWS) compared to wake field simulation (PS). Courtesy of L. Eidam [59].

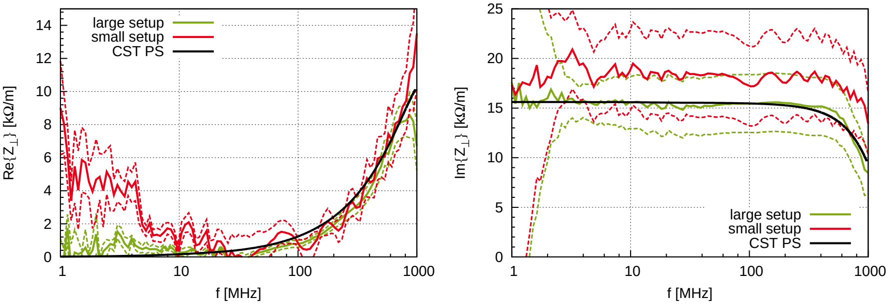

Figure 5.14.: Transverse impedance of the ferrite ring: Measurement vs. wakefield simulation. The dashed lines denote error bars. Courtesy of L. Eidam [59].

5.6.3 Coil Method

In order to enhance the extremely small signals in the twin wire method at low frequencies, the two wires can be replaced by a multi-turn coil. Both the magnetic flux and the induced voltage are magnified by the number of turns N and thus Eq. 5.37 has to be replaced by

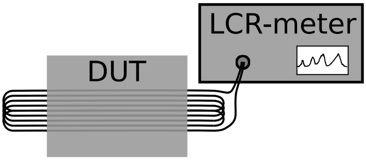

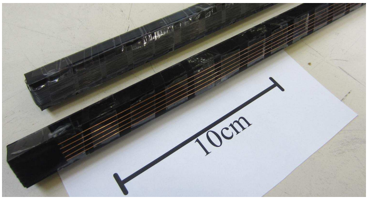

Figure 5.15.: Coil measurement setup (left) and different coils (right). Courtesy of L. Eidam [59].

$$Z_{\perp}^{\text{coil}} \approx \frac{c}{\omega \Delta^2 N^2} \delta Z \tag{5.38}$$

for the determination of the dipolar transverse impedance. The coil impedance difference $\delta Z = Z^{\text{DUT}} - Z^{\text{REF}}$ can be determined by a LCR-meter[5], where the REF measurement is performed just by measuring the coil outside the DUT in free space. The setup and two measurement coils can be seen in Fig. 5.15. The coil method has an upper frequency limit, at which the inter-turn capacitance causes a resonance. The resonance frequency is usually in the range of 1 MHz. It can be increased by taking fewer turns

---

[5] We used the Agilent E4980A [144], 20 Hz-2 MHz.

and increasing the turn distance. At extremely low frequency, the accuracy is limited by the instrument noise and the temperature drift of the coil resistance. Thus, it makes sense to use different coils, a temperature stable one (e.g. constantan wire) with many turns for low frequency and one with few turns and high conductivity (copper wire) for higher frequencies.

Since ferrites usually have very small impedance contributions at such low frequencies, the coil method is benchmarked using a steel beam pipe[6] of 2 mm wall thickness and 3.3 cm radius. The real part of the transverse impedance of the pipe, measured with the coils depicted in Fig. 5.15 is plotted in Fig. 5.16. Besides the noise at extremely low frequency, the measured real part of the impedance agrees well with the analytic prediction by Rewall [50].

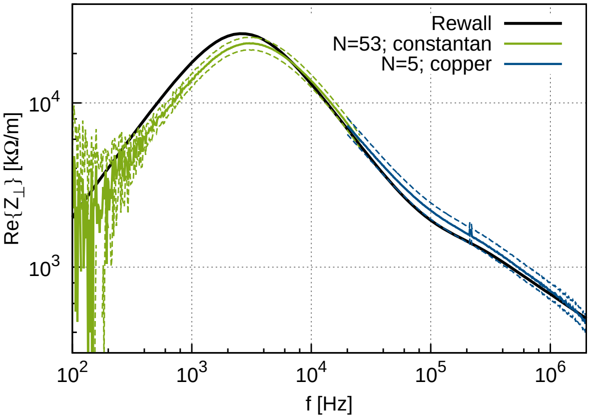

Figure 5.16.: Coil measurement of real transverse impedance of a tubular beam pipe vs. analytical calculation by Rewall. The dashed lines are error bars, obtained from measurement standard deviations and systematic errors, as e.g. the wire distance uncertainty.

Since the phase of the coil current does not depend on the longitudinal position, the coil method corresponds to entirely 2D source fields, i.e. $\partial_z = 0$ holds for the source fields. Thus, it does not correspond to an ultrarelativistic beam, but rather to the radial model, cf. Sect. 3.3.2. The agreement of the real part of the transverse beam impedance with the one obtained by the radial model at low frequencies is discussed in [52] and is hereby also confirmed by measurement.

However, the imaginary part of the measurement includes also the 'image inductance', i.e. the magnetic part of the transverse space charge impedance. For a circular

---

[6] The beam pipe dominates the transverse impedance of a synchrotron at such low frequencies.

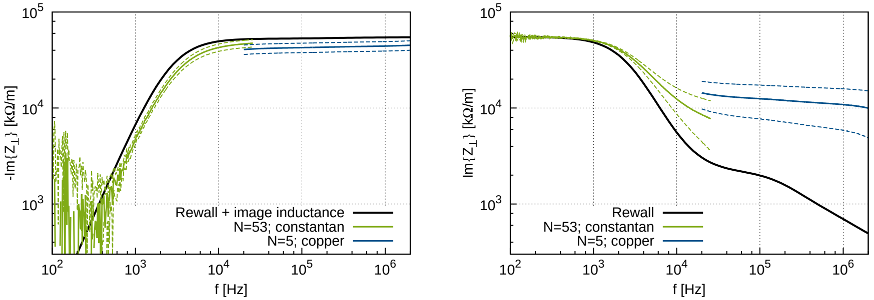

(a) Imaginary part of the measurement vs. Rewall analytical result plus image inductance $-i5.5 \cdot 10^4 \Omega/\mathrm{m}$ from Eq. 5.39.

(b) Imaginary part of the measurement minus image inductance vs. Rewall analytical result.

Figure 5.17.: Coil measurement of the imaginary part of the transverse resistive wall impedance of the tubular beam pipe. Again, dashed lines are error bars. Due to the high bias of the image inductance, the imaginary resistive wall impedance measurement result becomes very inaccurate.

pipe, it can be obtained separately [80], or from the space charge impedance (Eq. 3.49) by applying the radial model limit $\beta \rightarrow \infty$ (cf. Eq 3.36) as[7]

$$\underline{Z}_{\perp}^{\text{image}} = \frac{-iZ_0 l}{2\pi b^2} = \lim_{\beta \rightarrow \infty} \frac{1}{\beta} \underline{Z}_{\perp,\text{spch}}^{\text{indirect}}. \tag{5.39}$$

Note that the *direct* magnetic space charge impedance occurs in both DUT and REF measurements and is thus not present in the difference.

The measurement result of the imaginary part of the impedance is shown in Fig. 5.17. Since the image inductance is much higher than the imaginary part of the resistive wall impedance, small relative measurement errors lead to large relative errors for the imaginary restive wall impedance.

Thus, it can be concluded, that the coil method is effective only for the determination of the real part of the transverse restive wall impedance, as it is the case for simulations with the radial model.

---

[7] The factor $1/\beta$ occurs here, since $(\underline{\vec{E}} + \vec{v} \times \underline{\vec{B}})$ is in the definition of the impedance and thus dividing by β before taking the limit yields the magnetic part only.

6 Applications

6.1 Selected Impedance Induced Beam Effects

The imaginary part of the longitudinal and transverse beam coupling impedance causes real valued coherent tune shifts which are in good approximation proportional to the beam intensity. Thus, the imaginary (effective) impedance can be measured by so-called tune slopes, i.e. $\Delta Q/N \propto \mathrm{Im}\{Z\}$ with a known constant, calculated from the beam parameters, see e.g. [145]. The real part of the impedance, which corresponds to resistive loss, causes an imaginary coherent tune shift, which corresponds to a normalized beam instability rise time. In the following we will briefly discuss the quantification of the beam induced heat load and selected beam instabilities.

6.1.1 Beam Induced Heat Load

Beam induced heat load can become problematic in high intensity particle accelerators. Strongly lossy components can heat up to their melting point or to temperatures that severely interfere with the component's function (e.g. Curie-temperature). Also weakly lossy components are problematic in cryogenic sections, since the cryostat has to be designed to maintain the low temperature, which leads to costly power consumption of the cryo-plant.

Beam induced heat load increases strongly for decreasing bunch length. For coasting beams, there is no coherent heat load at all. The only power loss is due to the incoherent Schottky spectrum, i.e. the spectrum of the deviation of the real beam with large but finite number of particles from the idealized beam distribution function. However, this incoherent power loss scales only linearly with the number of particles N, whereas the coherent loss scales with N^2. Thus, the incoherent power loss is expected to be significantly smaller than the coherent one, but due to the extremely short length scale of the individual particles, it probes the longitudinal impedance at very high frequencies.

In the following we will look only at coherent loss. Starting from a single bunch and a single shot (as e.g. in a linac), the loss concept will be applied to multi-bunch systems in circular accelerators.

Coherent Losses of a Single Bunch and a Single Shot

The total heat load in an accelerator structure due to the passing of a particle bunch can be equated to the energy loss ΔE. Thus, the heat power is $P = \Delta E f_0$, where f_0 is the repetition frequency. The loss factor $\kappa_\parallel$ is defined by $\Delta E =: \kappa_\parallel q^2$. It can be obtained from the wake potential as

$$\kappa_\parallel = \int_{-L/2}^{L/2} W_{\mathrm{pot}}(s)\lambda(s)\mathrm{d}s, \quad \int_{-L/2}^{L/2} \lambda(s)\mathrm{d}s = N_\mathrm{b}, \tag{6.1}$$

where $\lambda(s)$ is the line density normalized to the total number of particles in the bunch N_b (see e.g. [89, 37]). Equation 6.1 presents the integrated product of the instantaneous voltage and current. Inserting the wake potential as the convolution of wake function and beam distribution we obtain

$$\kappa_\parallel = \int_{-L/2}^{L/2}\int_{-\infty}^{\infty} W_\parallel(s')\lambda(s-s')\lambda(s)\mathrm{d}s\mathrm{d}s' = L\int_{-\infty}^{\infty} W_\parallel(s')\mathrm{ACF}(-s')\mathrm{d}s', \tag{6.2}$$

where the auto-correlation function is defined as

$$\mathrm{ACF}(s') = \frac{1}{L}\int_{-L/2}^{L/2} \lambda(s+s')\lambda(s)\mathrm{d}s. \tag{6.3}$$

Here, the correlation length L was assumed to be much larger than the support of λ (bunch length). By means of the Wiener-Khinchine theorem, the FT of the ACF is the power spectral density

$$\mathrm{PSD}(\omega) = \int_{-\infty}^{\infty} \mathrm{ACF}(s)e^{-i\omega s/v}\frac{\mathrm{d}s}{v} = \frac{v}{L}|\underline{\lambda}(\omega)|^2. \tag{6.4}$$

The PSD is real valued, thus the time reversal in Eq. 6.2 has no effect. Transforming Eq. 6.2 to the FD by means of Plancherel's theorem, one obtains

$$\boxed{\kappa_\parallel = \frac{vL}{2\pi}\int_{-\infty}^{\infty} \underline{Z}_\parallel(\omega)\mathrm{PSD}(\omega)\mathrm{d}\omega = \frac{v^2}{\pi}\int_0^{\infty} \mathrm{Re}\{\underline{Z}_\parallel(\omega)\}|\underline{\lambda}(\omega)|^2\mathrm{d}\omega,} \tag{6.5}$$

where the contribution of the imaginary impedance vanishes since it is an odd function and the PSD is even.

We consider the simplified example of a Gaussian bunch[1]

$$\lambda(s) = \frac{N_\mathrm{b}}{\sqrt{2\pi}\sigma_s}e^{-\frac{1}{2}\left(\frac{s}{\sigma_s}\right)^2}, \quad |\underline{\lambda}(\omega)|^2 = \frac{N_\mathrm{b}^2}{v^2}e^{-\left(\frac{\sigma_s\omega}{v}\right)^2}. \tag{6.6}$$

---

[1] In practice, bunches in synchrotrons are rather parabolic, due to the RF-potential well. However, since the exact distribution is crucial for heat load estimations, the use of measured PSD can be preferable [146].

The loss factor for a simplified cylindrical thick wall resistive impedance $\mathrm{Re}\,\{\underline{Z}_\parallel(\omega)\} = R_\mathrm{Ohm}\sqrt{\omega/\omega_\mathrm{skin}}$ becomes (see also [42], p. 20)

$$\kappa_\parallel = \frac{1}{\pi}N_\mathrm{b}^2\int_0^\infty R_\mathrm{Ohm}\sqrt{\frac{\omega}{\omega_\mathrm{skin}}}e^{-\left(\frac{\sigma_s\omega}{v}\right)^2}\mathrm{d}\omega = \frac{1}{2\pi}N_\mathrm{b}^2\frac{R_\mathrm{Ohm}}{\sqrt{\omega_\mathrm{skin}}}\left(\frac{v}{\sigma_s}\right)^{3/2}\Gamma(3/4), \tag{6.7}$$

where Γ is the Euler Gamma-function and $\Gamma(3/4) \approx 1.225$. Note the dependence on σ_s, which leads to a strong increase of the power loss for smaller bunch length.

Coherent Losses of Many Bunches Revolving in a Ring

Due to the periodic passage of the beam in a ring accelerator, the spectrum must be discrete, i.e. it probes the impedance only at integer revolution harmonics. Thus, Eq. 6.5 must be replaced by

$$\kappa_\parallel = \frac{v^2}{\pi}\sum_{k=1}^{\infty}\mathrm{Re}\,\{\underline{Z}_\parallel(k\omega_0)\}|\underline{\lambda}(k\omega_0)|^2\omega_0. \tag{6.8}$$

We will now look at many bunches in the ring. For M equi-spaced buckets, filled with $M-\xi$ bunches of equal intensity N_b (ξ empty buckets), the line density in TD reads

$$\lambda_M(t) = \sum_{m=0}^{M-1-\xi}\lambda_B\left(t - \frac{m}{M}T_0\right), \tag{6.9}$$

where λ_B is the distribution of one bunch with support $\mathrm{supp}(\lambda_B) \subset]0, C/M[$ and revolution period $T_0 = 2\pi/\omega_0$. Thus, the scaled PSD becomes

$$|\underline{\lambda}_M(\omega)|^2 = |\underline{\lambda}_B(\omega)|^2\left|\sum_{m=0}^{M-1-\xi}e^{-i\omega T_0\frac{m}{M}}\right|^2. \tag{6.10}$$

The sum of exponentials can be simplified by means of the finite geometric series as

$$\sum_{m=0}^{M-1-\xi}e^{-i\omega T_0\frac{m}{M}} = \frac{\sin\left(\frac{\omega T_0}{2M}(M-\xi)\right)}{\sin\left(\frac{\omega T_0}{2M}\right)}e^{-i\omega T_0\frac{M-\xi-1}{2M}}. \tag{6.11}$$

In the special case where $\xi = 0$, i.e. all buckets filled with M equi-spaced and equi-populated bunches the PSD becomes

$$|\underline{\lambda}_M(\omega)|^2 = |\underline{\lambda}_B(\omega)|^2\left|\frac{\sin\left(\frac{\omega T_0}{2}\right)}{\sin\left(\frac{\omega T_0}{2M}\right)}\right|^2. \tag{6.12}$$

Evaluated at the revolution harmonics $k \in \mathbb{N}$, this is

$$|\underline{\lambda}_M(k\omega_0)|^2 = |\underline{\lambda}_B(k\omega_0)|^2 \left| \frac{\sin(k\pi)}{\sin\left(\frac{k\pi}{M}\right)} \right|^2 = |\underline{\lambda}_B(k\omega_0)|^2 M^2 \sum_{\nu=-\infty}^{\infty} \delta_{k,\nu M}, \tag{6.13}$$

i.e. only every M-th revolution harmonic is present in the spectrum. Thus, the loss factor can be written as

$$\kappa_{\|} = \frac{v^2}{\pi} \omega_0 M^2 \sum_{k=1}^{\infty} \mathrm{Re}\left\{\underline{Z}_{\|}(kM\omega_0)\right\} |\underline{\lambda}_B(kM\omega_0)|^2. \tag{6.14}$$

Some comments about this result are in order. For a narrow banded impedance in the range of an M-th revolution harmonic, the power load of many bunches will add up coherently, i.e.

$$\kappa_{\|}^{\mathrm{NB}} = \frac{v^2}{\pi} \omega_0 M^2 \mathrm{Re}\left\{\underline{Z}_{\|}(k_{\mathrm{res}} M\omega_0)\right\} |\underline{\lambda}_B(k_{\mathrm{res}} M\omega_0)|^2, \tag{6.15}$$

where a sharp resonance at the frequency $\omega_{res} = k_{\mathrm{res}} M\omega_0$ was assumed such that all other impedance contributions can be neglected. However, if the impedance is broadband, one can see in Eq. 6.14 that only every M-th revolution band is sampled. Thus for a roughly constant broadband impedance, there is only a linear dependence on M, i.e. the losses of multiple bunches add up incoherently. Assuming realistically that even $M \cdot \omega_0$ is much smaller than the frequency associated with the bunch length, it is justified to approximate a broadband impedance to be constant within an $M\omega_0$-interval. Under this assumption, Eqs. 6.14, Eq. 6.8, and Eq. 6.5 evaluate almost identically, provided the single bunch cases are multiplied by the number of bunches M. Therefore, in practice, the integral formula for the single bunch single shot loss is frequently used also for losses on broadband impedances in circular accelerators with many bunches.

6.1.2 Coasting Beam and Coupled Bunch Transverse Instabilities

Complicated transverse beam instabilities, such as the ‘head-tail’ instability [147] or the Transverse Mode Coupling Instability (TMCI) [148], take place in a broad range of the beam spectrum, i.e. on many betatron sidebands. Therefore, one defines a so-called effective impedance, i.e. an impedance weighted with the beam (mode-) spectrum, integrated over the whole frequency axis.

For simplicity, we restrict ourselves here to transverse instabilities that happen at a single frequency in the spectrum, such as the resistive coasting beam instability, which is illustrated in Fig. 6.1. We assume a coherent motion which needs to be C periodic in

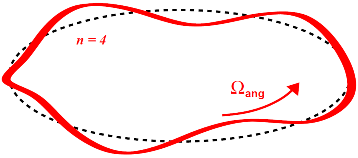

Figure 6.1.: A coherent coasting beam mode. Courtesy of V. Kornilov [15].

z, i.e. $k_z = 2\pi n/C$, as

$$\overline{y} = y_0 \mathrm{Re}\left\{e^{i(k_z z - \underline{\Omega} t)}\right\} = y_0 \mathrm{Re}\left\{e^{i(n\omega_0 - \underline{\Omega})t}\right\}, \tag{6.16}$$

where $\underline{\Omega}$ is the complex frequency of the mode and $\mathrm{Im}\{\underline{\Omega}\} > 0$ corresponds to an exponential growth, i.e. a beam instability. The coherent dipolar beam current is

$$I_{\mathrm{dip}}^{\mathrm{coh}} = \overline{y}\frac{Nq}{C}v \tag{6.17}$$

and the dipolar transverse impedance creates the coherent integrated force on a single test charge q

$$\oint F(\omega_w)\mathrm{d}z = iZ_\perp^{\mathrm{dip}}(\omega_w) I_{\mathrm{dip}}^{\mathrm{coh}} q = iZ_\perp^{\mathrm{dip}}(\omega_w)\frac{Nq^2 v}{C}\overline{y} \tag{6.18}$$

in each turn, where the ω_w is the yet unknown frequency of the mode.

Neglecting the average detuning impedance, the equation of coherent transverse motion (Eq. 2.34) can be written as

$$\partial_t^2 \overline{y} + \omega_\beta^2 \overline{y} = \frac{1}{m\gamma} i\underline{Z}_\perp \frac{Nq^2 v}{C^2}\overline{y}. \tag{6.19}$$

This equation can be transformed using the FT correspondence $\partial_t^2 \to -(n\omega_0 - \underline{\Omega})^2$, obtained from Eq. 6.16, as

$$\omega_\beta^2 - (n\omega_0 - \underline{\Omega})^2 = i\underline{Z}_\perp \frac{Nq^2 v}{C^2 m\gamma}, \tag{6.20}$$

which can be solved for $\underline{\Omega}$ as

$$\underline{\Omega} = n\omega_0 \pm \sqrt{\omega_\beta^2 - i\underline{Z}_\perp \frac{Nq^2 v}{C^2 m\gamma}} \approx n\omega_0 \pm \left[\omega_\beta - \frac{1}{2\omega_\beta} i\underline{Z}_\perp \frac{Nq^2 v}{C^2 m\gamma}\right]. \tag{6.21}$$

Note that Eq. 6.20 is actually an eigenvalue equation for the mode frequency. However, when the impedance is treated as a perturbation, it can be readily solved as in Eq. 6.21. The two solutions correspond to two different kinds of plasma waves along the ring. The 'fast wave' ('+' solution) probes the impedance at $(n+Q)\omega_0$, i.e. the right hand side betatron sideband. The positive real part of the resistive impedance leads to a negative $\mathrm{Im}\{\underline{\Omega}\}$, which is a damping. For the 'slow wave' ('-' solution), which probes the impedance at $(n-Q)\omega_0$, it is oppositely, and the growth rate for each mode n is

$$\frac{1}{\tau_n} = \mathrm{Im}\{\underline{\Omega}_n\} = \frac{Nq^2}{4\pi C Q_y m\gamma} \mathrm{Re}\{\underline{Z}_\perp^{\mathrm{dip}}[(n-Q_y)\omega_0]\}. \tag{6.22}$$

When there is no damping, all modes n rise simultaneously. However, in many synchrotrons, due to the beam pipe, $\mathrm{Re}\{\underline{Z}_\perp^{\mathrm{dip}}\}$ is highest for the lowest frequency. Thus, the $(1-Q_f)\omega_0$- mode, where Q_f is the fractional part of the tune, rises dominantly.

Similarly as for the coasting beam, also the lowest frequency coupled bunch mode (i.e. each bunch treated as a rigid body) happens to be at $(1-Q_f)\omega_0$. Therefore, the low frequency transverse impedance is a major concern in the construction of large synchrotrons. However, particularly at LF, impedance induced instabilities can be damped by feedback systems. The amount of impedance that can be damped, depends on the feedback gain. However, at high gain also the amplified pickup noise becomes significant, which can lead to beam heating and emittance growth.

6.1.3 Longitudinal Instabilities in Coasting Beams and Long Bunches

As an example for longitudinal instabilities, we will mention only the so-called 'negative-mass-' or 'microwave-instability' for coasting beams or long uncoupled bunches. Exchanging the RF-potential with a beam created potential, one obtains an eigenvalue equation similarly to Eq. 6.20, namely (see [31], Eq. 19.59 or [42], Eq. 5.16)

$$(\underline{\Omega} - n\omega_0)^2 = -in\underline{Z}_\parallel(n\omega_0)\frac{Nq^2\omega_0}{C^2 m^*}, \tag{6.23}$$

where $m^* = m\gamma/\eta$ is the effective mass which changes sign at transition energy. In the presence of a real part of the impedance, we always find an unstable solution called 'microwave-instability', since the square root of something imaginary has to be taken. However, if the impedance is purely imaginary ($\underline{Z}_\parallel = iZ_\parallel^{\mathrm{i}}$), we find a real solution if η and $Z_\parallel^{\mathrm{i}}$ have the same signs. The instability for opposite signs lead to the name 'negative-mass-instability'. Thus, we can conclude, that for space charge dominated synchrotrons (i.e. $Z_\parallel^{\mathrm{i}} \ll 0$) the negative mass instability does not occur below transition energy.

6.1.4 Landau Damping and Nonlinear Contributions

After reading the two previous sections one would assume that any resistive energy loss causes a destructive beam instability. In reality, a certain amount of resistivity is tolerable due to Landau damping of collective phenomena. Landau damping is based on a dispersion relation for the particle distribution, which leads to interaction of coherent and incoherent phenomena. The crucial parameter is the momentum spread, which influences the longitudinal stability directly and the transverse stability by virtue of a tune spread obtained from the chromaticity, i.e.

$$\frac{\Delta Q}{Q_0} = \xi \frac{\Delta p}{p_0}. \tag{6.24}$$

The tolerable amount of impedance ('impedance budget') is usually quantified in stability diagrams (see e.g. [42], p. 168), visualizing contours of constant growth rate in the complex impedance plane. In the presence of Landau damping, the stability diagrams feature an area of zero growth rate, i.e. a domain of the impedance in the complex plane, on which the beam is stable. This area depends, among other parameters, on the beam intensity N and on the momentum spread. It can be estimated by stability criteria, such as the Keil-Schnell criterion [149] for the longitudinal negative mass or microwave instability in long bunches or coasting beams (see also e.g. [31], Eq. 19.98 or [42], Eq. 5.23)

$$\frac{|\underline{Z}_{\parallel}(n\omega_0)|}{n} < F \frac{m\gamma v|\eta|C}{q^2 N} \left(\frac{\Delta p}{p_0}\right)^2_{\mathrm{FWHM}}, \tag{6.25}$$

where the beam distribution dependent form factor F is of the order of 1. In the transverse plane, a similar stability criterion was derived for the coasting beam instability by Zotter [150] (see also [42], Eq. 13.86),

$$|\underline{Z}_{\perp}^{\mathrm{dip}}((n-Q)\omega_0)| \lesssim F \frac{8\pi^2}{\sqrt{3}} \frac{m\gamma Qc}{q^2 N} |S_n| \left(\frac{\Delta p}{p_0}\right)_{\mathrm{HWHM}}, \tag{6.26}$$

where $S_n = \xi + (n-Q)\eta$ is the effective chromaticity for the mode n. Furthermore, the transverse Landau damping can be enhanced by a betatron amplitude dependent tune spread, which is created by higher order multipole magnets (in practice mostly octupoles). Space charge and beam-beam effects play an important role in the analysis of Landau damping, since they can introduce significant tune spreads. However, space charge tune spreads do not introduce Landau damping themselves, since the incoherent space charge field moves as a whole in the presence of coherent oscillations. Nonetheless, space charge can both enhance or deteriorate the Landau damping due to other nonlinearities, as discussed in detail for the coasting beam in [151, 152] and for head-tail modes in bunched beams in [153, 154, 155].

6.2 Selected Impedance Results for the FAIR SIS-100

The kicker magnets in the future SIS-100 synchrotron are the dominant sources of transverse impedance at the frequency associated with the bunch length. Also, they have a large longitudinal impedance contribution at this frequency, which makes them susceptible to beam induced heat load. There are different kinds of kicker magnets outlined for the SIS-100, see [156] and an excerpt of the relevant data in App. F. The largest transverse impedance effects are supposed to originate from the bipolar extraction/emergency kicker magnets, where eight modules will be installed in the SIS-100. Another concern is the heat load in the SIS-100-to-SIS-300 transfer kicker magnets, which are outlined for the last stage of FAIR. Due to limited space in the ring, it was outlined to place one of the six modules in a cryogenic section, which requires to reduce the heat load as much as possible. Apart from the kicker magnets, we will also estimate the heat load for the cryogenic beam pipe.

6.2.1 Beam Induced Heat Load

The beam induced heat loads in the cryogenic pipe and transfer kicker magnets for the SIS-100 are evaluated for the high intensity single-bunch proton scenario (see Tab. F.1). Apart from the highest intensity, this scenario presents the shortest bunch length and thus the highest heat load.

The power loss per length in an idealized SIS100 pipe with radius 4 cm and conductivity $\kappa = 2\,\mathrm{MS/m}$ is evaluated by Eq. 6.5 to

$$\frac{P}{l} = \frac{\kappa_{\|} q^2}{T_0 l} = 0.89\,\mathrm{W/m}, \tag{6.27}$$

i.e. a total loss of $\approx 500\,\mathrm{W}$ in the cryogenic sections, which is acceptable for the cooling system.

The beam induced heat load in a kicker module depends crucially on the ferrite yoke gap. If there is no gap, the magnetic circuit is closed and the longitudinal impedance is much larger. In the presence of a gap, the longitudinal impedance can be further decreased by increasing the path length for the magnetic field lines outside the ferrite. However, achieving this by increasing the gap thickness can be disadvantageous for the kick field quality. For this reason, it is outlined to fill the gap highly conductive material, i.e. copper. Such a copper sheet influences the kick-field only weakly, since the dipolar field has a symmetry plane at the position of the gap. Figure 6.3 shows the longitudinal impedance of a transfer kicker module (see tab. F.2) from 2D FIT and FEM simulations, as a comparison between a vacuum and a copper filled gap. The difference between

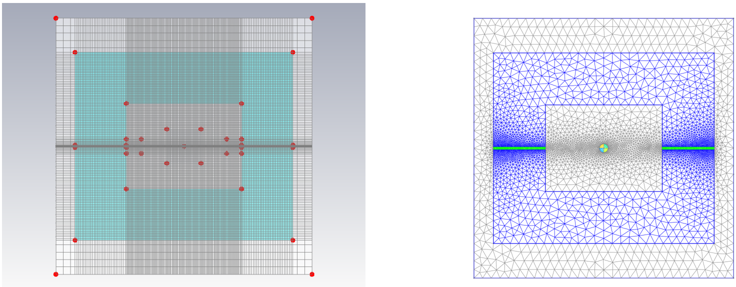

Figure 6.2.: FIT and FEM mesh for the extraction/emergency kicker (vertical kick). The 2.8 mm wide yoke gaps (green) are either open (vacuum) or filled with a copper sheet.

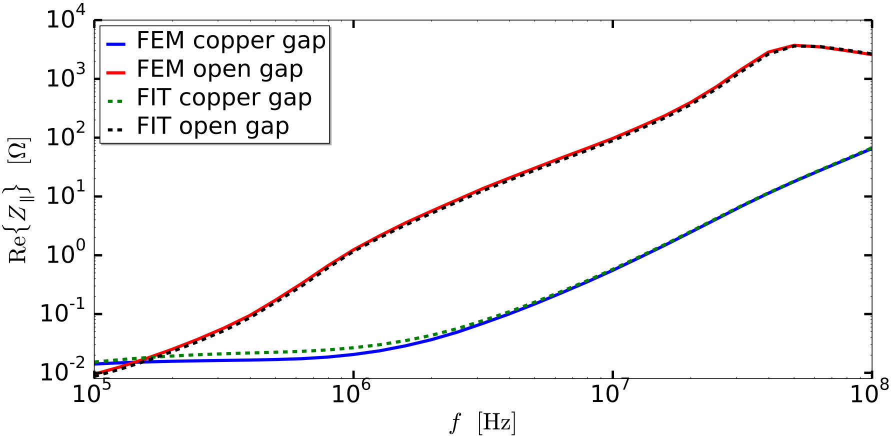

Figure 6.3.: Longitudinal impedance of the transfer kicker magnet w/o copper filling of the yoke gap ($\beta = 1$).

the two is significantly, i.e. two orders of magnitude. The resulting heat power for the proton scenario is evaluated by Eq. 6.8 as

$$P \approx \begin{cases} 7327\,\mathrm{W} & \text{for vacuum gap (red line)} \\ 48\,\mathrm{W} & \text{for copper filled gap (blue line).} \end{cases} \tag{6.28}$$

Note that these value holds for CW operation, in practice they have to be scaled with the duty factor which is in the range of 0.5 at most. Since between the ferrite yoke and its mounting structure is always a small vacuum gap, the heat conduction is poor.

Thus, the cooling of the yoke happens almost solely by heat radiation. The temperature (at thermal equilibrium) can be calculated by invoking the Stefan-Boltzmann law, see [157], where it is discussed that the 48 W are tolerable.

6.2.2 Transverse Impedance of an Emergency/Extraction Kicker Module

The transverse impedance of a ferrite kicker module does not only originate from the lossy ferrite yoke, but also from the coupling to the supply network of the kicker. The supply network is in principle a TEM cable, that is supposed to store a rectangular current pulse and transport it through the kicker magnet in a low-dispersion manner. Since realizing this with a cable requires a rather long, bulky, and expensive cable, a lumped element replacement circuit for the cable is preferred in many cases. This so-called Pulse Forming Network (PFN) introduces a low-pass behavior with an upper limit frequency. The low pass behavior restricts the rise time of the kicker pulse, which is one of the critical design parameters for the PFN, see [158] for more details.

Instead of discussing all details of the PFN, we will just regard its complex impedance, $\underline{Z}_{\mathrm{g}}(\omega)$, seen from the kicker magnet's terminal. The finite-valued circuit elements in the PFN introduce resonances in $\underline{Z}_{\mathrm{g}}$, which lead to resonances in the transverse beam impedance. A numerical calculation of the PFN impedance for the SIS-100 extraction kicker system is shown in App. F.

Generally one can consider the connection of the Pulse Forming Network (PFN) to the transverse beam impedance as 4-pole network, where two poles are represented by the network and the other two poles are given by the beam as

$$\begin{bmatrix} \underline{U}_{\mathrm{beam}} \\ \underline{U}_{\mathrm{terminal}} \end{bmatrix} = \begin{bmatrix} \underline{Z}_{11} & \underline{Z}_{12} \\ \underline{Z}_{21} & \underline{Z}_{22} \end{bmatrix} \begin{bmatrix} \underline{I}_{\mathrm{beam}} \\ \underline{I}_{\mathrm{terminal}} \end{bmatrix}. \tag{6.29}$$

From the impedance matrix of such a four pole one finds [159]

$$d_y Z_{\perp,y} = \frac{\underline{U}_{\mathrm{beam}}}{\underline{I}_{\mathrm{beam}}} = \underline{Z}_{11} + \frac{\underline{Z}_{21}\underline{Z}_{12}}{\underline{Z}_{\mathrm{g}} - \underline{Z}_{22}}, \quad \text{with} \quad \underline{Z}_{\mathrm{g}} = \frac{\underline{U}_{\mathrm{terminal}}}{\underline{I}_{\mathrm{terminal}}}. \tag{6.30}$$

The first term, $\underline{Z}_{11}$, can be interpreted as the impedance of the kicker without the network, i.e. the coil being open-circuited. It is obtained from a FIT and FEM simulation, as depicted in Fig. 6.4.

Under the assumptions of the radial model, the second term can be interpreted as a transformator circuit, i.e. the Nassibian-Sacherer [81] model. The coil self inductance and the beam-coil mutual inductance can be written as

$$L = N_{\mathrm{coil}}^2 \mu_0 l \frac{b_v}{b_h} \quad \text{and} \quad M = N_{\mathrm{coil}} \mu_0 l \frac{d_y}{b_h}, \tag{6.31}$$

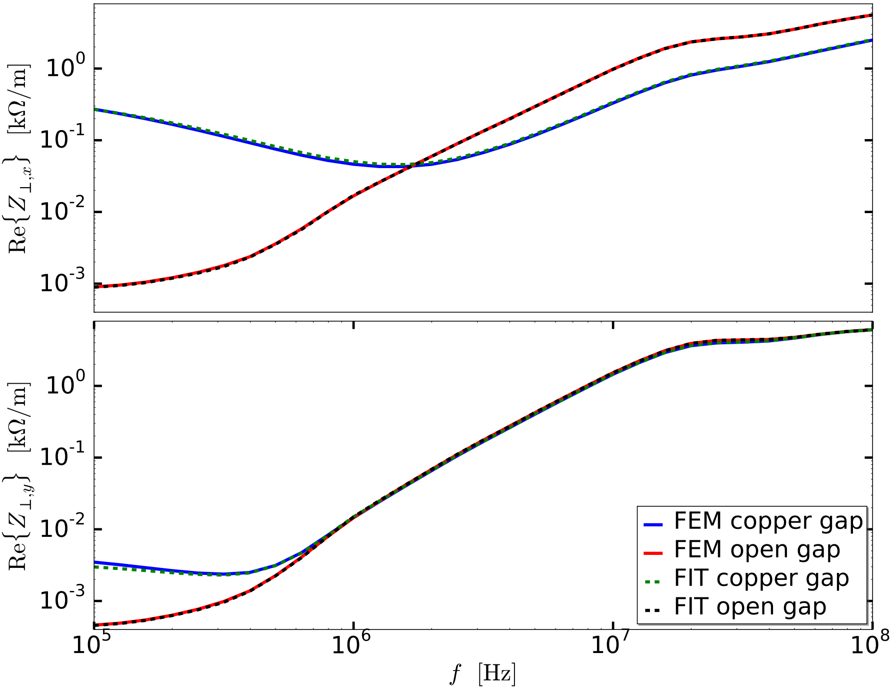

Figure 6.4.: Horizontal and vertical transverse impedance due to the ferrite yoke of an extraction/emergency kicker module w/o copper inserts in the ferrite gaps ($\beta = 1$).

where the geometrical parameters can be taken from Tab F.3. By direct comparison, the impedance matrix entries are found as

$$\frac{1}{d_y}\underline{Z}_{12}\underline{Z}_{21} = \frac{c}{\omega d_y^2}(\omega M)^2 \quad \text{and} \quad \underline{Z}_{22} = i\omega L, \tag{6.32}$$

where the first term in the product is the same as for the coil measurement, cf. Eq. 5.38. Note that the coil inductance can also be easily measured, see Fig. F.4 for a measurement of the SIS-18 kicker. The frequency at which the inductance drops down, i.e. ≈ 45 MHz, marks the limit of the validity of the transformer model. Inserting Eq. 6.32 into Eq. 6.30 and taking the values from Tab F.3, the transverse beam impedance due to the PFN is found from the PFN impedance as plotted in Fig. 6.5 (top). The impedance of the PFN (Fig. F.2) is computed by circuit simulation using LT-SPICE [160] (Simulation Program with Integrated Circuit Emphasis) and plotted in Fig. F.3.

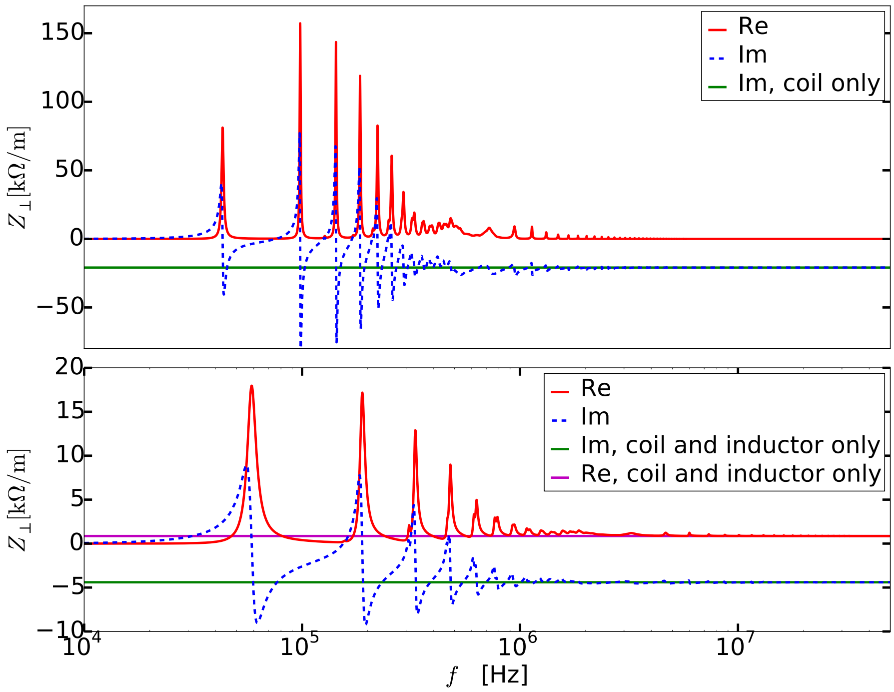

Figure 6.5.: Transverse impedance due to the PFN of the extraction/emergency kicker module. The upper plot shows the original PFN. In the lower plot a nonlinear complex inductor of $10 - 2.5i\,\mu$H in series has been added.

A method to reduce the impedance due to the PFN is given by adding a ferrite inductor in series to the kicker, i.e. $\underline{Z}_{22} = i\omega(L + \underline{L}_{\text{ind}})$. In order to make sure that such an inductor does not distort the shape of the kicker pulse, it can be realized by a ferrite tube, which is immediately driven into saturation by the strong kicker pulse[2]. For the much less intense dipolar beam signal the (complex) inductance is for a coaxial shape

$$\underline{L}_{\text{ind}} = \underline{\mu}_r\, l \frac{\mu_0}{2\pi} \ln \frac{r_a}{r_i}. \tag{6.33}$$

Taking realistic values $\underline{\mu}_r = (1000 - i250)$, $l = 5\,\text{cm}$, $r_i = 1\,\text{cm}$, and $r_a = 2.71\,\text{cm}$, we obtain $\underline{L}_{\text{ind}} = (10 - 2.5i)\,\mu\text{H}$. Redoing the calculation of the beam impedance with the new Z_{22} leads to a much lower transverse impedance, as plotted in Fig. 6.5 (bottom). Additionally, due to the losses in the inductor, the PFN resonances have been broadened.

---

[2] The use of nonlinear material allows nicely to circumvent the reciprocity theorem!

7 Summary and Outlook

After introducing the theory of wake functions and beam coupling impedances, analytical methods and reduced numerical models have been discussed first. Quasi-stationary modeling can be employed for the computation of beam coupling impedances only under particular circumstances. The Darwin model, which neglects EM waves, is suited for low beam velocity. Contrarily, the radial model, which neglects the beam charge, is suited only for high beam velocity, since it actually corresponds to infinite velocity, i.e. $\partial_z = 0$ for the source terms. However, a general tool for impedance computation at arbitrary beam velocity requires solving the full Maxwell equations.

Two FD solvers were developed in the course of this thesis. The first one is based on the FIT and uses a simple, structured, staircase mesh. It has the drawback that curved structures cannot be modeled accurately. This leads to the inability to model a dipole moment as a $\cos\varphi$-shape for the transverse impedance and thus a twin wire representation is chosen. However, since the direct space charge field is unknown for a twin wire representation on a finite mesh, the imaginary part of the transverse wall impedance can be determined by the FIT solver for $\beta = 1$ only.

This problem is overcome by the second solver developed in this thesis, which uses the FEM on an unstructured 2D mesh. The dipole moment is represented as a $\cos\varphi$-shaped ring and the analytically known direct transverse space charge impedance is subtracted from the impedance result. Thus, the indirect space charge and resistive wall impedance can be determined for arbitrary β.

The FIT solver works both in 2D and 3D. However, since the number of DoFs in 3D is very high, the focus was put on small and handy 2D computations. In order to make use of the 3D solver practically, parallel computing would be required.

The 2D solvers have been validated on metallic beam pipes and a tubular ferrite structures, where analytic solutions are available. The agreement to the analytical results was found reasonably well, although the convergence of the staircase FIT for curved structures is slow. The SIBC, which was implemented in FEM, allows to increase the frequency to very high values, since meshing the skin depth is avoided. However, at extremely high conductivity and high frequency, the transverse impedance becomes small, and even at high γ the error of the space charge impedance can prevail over the small resistive wall impedance. This problem was found to pollute the solution of the imaginary part of the transverse impedance of the FCC beam pipe at high frequency.

In order to get more confidence on involved impedance simulations, dedicated bench measurements were outlined. An extensive analysis of the single and twin wire method was performed and the impedance of particular samples was measured in a dedicated laboratory at GSI, which was set up during the years of this thesis. For the longitudinal impedance, one has to distinguish a-priori between lumped and distributed impedances.

This is required since a large impedance causes an attenuation, which can be localized or distributed. This attenuation has to be measured to conclude on the impedance, based on the a-priori model. For the dipolar transverse impedance measurement, the signals become small, and the conversion formulas can be linearized. Thus, one does not have to distinguish between lumped and distributed impedances anymore. However, the signal becomes extremely small at LF, and the insufficient SNR makes the method unusable. This can be improved by taking a multi-turn coil instead of the wires. The signal is enhanced by the number of turns squared, and is thus measurable down to very low frequencies. Since there is no longitudinal phase advance in the coil, the coil method has to be interpreted in the framework of the radial model, i.e. quasi-stationary.

In the last chapter, applications were discussed. First, beam induced component heat load and impedance induced beam instabilities were reviewed. Then, selected calculations for the kicker magnets in the future SIS-100 synchrotron for FAIR were presented. These calculations are the basis of beam stability estimates performed in the GSI PBBP (beam physics) group. The kicker impedance does not only consist of the dispersive ferrite yoke part, but also of the coupling to the kicker's external supply network. This can be readily imagined by a transformer picture and the reciprocity theorem (primary and secondary coils can be exchanged). It was shown, that the transverse beam coupling impedance due to the network can be significantly reduced by putting a nonlinear ferrite inductor in series to the network. The kicker pulse, however, is not affected, since the strong pulse current drives the ferrite immediately into saturation, and therefore the permeability (and thus the inductance) becomes small.

In the future, also the FEM solver can be extended to 3D simulations, which would require similar computational resources as for FIT. In my opinion, it is worth investing efforts to create such a tool in a computationally effective and parallelized manner. This would be the counterpart to 3D TD solvers, which would complete the ensemble of available solvers, such that the impedance of any accelerator component can be computed. However, in the development of such a 3D solver one would have to face many challenges beyond high performance computing. For example, holes in the computational domain (PEC wires) would put restrictions on the Helmholtz decomposition. Furthermore, the unstructured mesh does not allow simple Floquet boundary conditions, i.e. the map from the entry to the exit of the beam cannot be used. Port boundary conditions would have to be implemented instead.

The Floquet boundary conditions in FIT, however, can also be employed to compute the impedance of periodic structures. Examples of such are dielectric gratings, which are used in Dielectric Laser Acceleration (DLA), see [161].

8 Acknowledgment

First of all, I would like to thank Prof. O. Boine-Frankenheim for accepting me as a PhD student. Due to him, it was possible for me to explore the field of accelerator physics and travel around the world to visit many accelerator laboratories and conferences. Prof. Boine-Frankenheim convinced me to publish a lot and to interact as much as possible with other scientists, which opened plenty of opportunities and broadened my knowledge immensely.

I am grateful to Prof. T. Weiland for being the second referee in this thesis and for his few, but extremely precise comments on the manuscript. Also I thank him for valuable hints on presenting complicated beam impedance issues comprehensively. Additionally, I thank him and Ulrich Römer for teaching me skiing in the Kleinwalsertal.

I thank GSI Darmstadt and the graduate school HGS-hire for FAIR for the financial support and offering soft-skills and accelerator physics courses. Particularly the 'power-week' on software design was informative, thus I am grateful to our instructor Dr. C. Mann.

I am grateful for the productive and friendly environment at TEMF. Particularly Prof. H. De Gersem, Prof. S. Schöps, Dr. W. Ackermann and Ulrich Römer gave me extremely valuable comments on finite element methods. Dr. W. Müller had always answers to my questions in administrative and computation issues. I thank Klaus Klopfer for his help concerning the PETSc software and the extremely good collaboration in the material measurements that have been performed for his PhD thesis. Hereby, I wish to thank Prof. H. Klingbeil for supporting us at GSI and sharing his wide knowledge in RF-engineering. Aside from their scientific inspirations, I wish to thank my office colleagues Paul Görgen, Kerstin Groß and Thibault Ferrand for being nice company and calming me down when trivial computer errors drive me crazy. A big 'thank you' also to all the other TEMF colleagues and former TEMF colleagues who are not listed by name.

My distinguished gratitude goes to Lewin Eidam. His MSc thesis under my supervision was a great success and we had a particularly great time also in collaborating with CERN in the bench measurements. The work that has been done in Lewin's thesis found its way into a publication [59] and also into this thesis, i.e. in Chapter 5.

I also enjoyed the working environment in the GSI PBBP group, thus I particularly thank Dr. S. Appel, Dr. V. Kornilov, Dr. G. Franchetti, and Dr. J. Oberrath. I owe particular gratitude to Prof. A. Al-Khateeb, King-Faisal university, Saudi Arabia (formerly GSI and TEMF) for teaching me about analytical impedance calculations. I thank Dr. U. Blell (GSI PBHV) for explaining me about ferrite kicker function and providing the relevant data for SIS-100. Also, I owe him gratitude for helping us with furnishing the new RF-lab for the bench measurements. I also thank Martin Stedler, who is

with Rohde&Schwarz GmbH, for interesting discussions about RF-network analysis and paragliding fun.

I am indebted to the colleagues from CERN, particularly to Dr. E. Metral, who invited me for a 4 weeks stay as a guest scientist. During this period, I could learn a lot about the impedance issues for the CERN synchrotrons. I was warmly welcomed at CERN and for that I wish to thank especially Dr. B. Salvant. Particularly interesting discussions came up with Dr. N. Mounet, Dr. C. Zannini, Dr. N. Biancacci and Dr. A. Burov. For the bench measurements, Lewin and I had another stay at CERN, invited by E. Metral. In this short period we worked together with Fritz Caspers and Manfred Wendt, who I hereby wish to thank deeply.

For the work that we have recently done collaboratively for the FCC design study, I thank especially Thilo Egenolf and Dr. F. Petrov from TEMF and Dr. X. Buffat from CERN.

Finally, I wish to thank Prof. Boine-Frankenheim, Prof. Weiland, Prof. De Gersem, Paul Görgen, Lewin Eidam, Nikolai Schmitt, and Peter Schmidt for proofreading this manuscript.

Last but not least, I thank my family and friends for supporting me during a tough and busy period of life.

A Multipole Expansions for the Wake Potential and Generalizations

Throughout this chapter we will assume $\beta = 1$ and the total (source) charge is q_1. Thus, according to Theorem 2, the longitudinal wake function is a harmonic function of the transverse coordinates of the test particle.

This dependence can be written as a multipole expansion with m-polar longitudinal wake functions $W_{\|,m,k}$ in units of $\mathrm{V}/(\mathrm{Asm}^{m+k})$ as

$$W_{\|}(x,y,s) = \sum_{m=0}^{\infty} a^k \varrho^m \left[W^{\text{normal}}_{\|,m,k}(s)\cos(m\varphi) + W^{\text{skew}}_{\|,m,k}(s)\sin(m\varphi) \right], \tag{A.1}$$

with cylindrical coordinates $x = \varrho\cos\varphi,\ y = \varrho\sin\varphi$. Here, the source is chosen to be a multipole of order k,

$$\sigma(\varrho,\varphi) = \frac{1}{\pi a^2}\delta(a-\varrho)\cos(k\varphi), \tag{A.2}$$

where one has to take into account, that for $k > 1$ the moments are not independent of the reference radius a anymore. Note that for a cylindrically symmetric structure all wake-multipoles with $m \neq k$ vanish, and many authors identify m with k.

The transverse wake function can be written as

$$\begin{aligned}
&-\partial_s \vec{W}_{\perp}(x,y,s) = \nabla_{\perp} W_{\|}(x,y,s) \\
&= \sum_{m=0}^{\infty} a^k m \varrho^{m-1} \Big[(W^{\text{normal}}_{\|,m,k}(s)\cos(m\varphi) + W^{\text{skew}}_{\|,m,k}(s)\sin(m\varphi))\vec{e}_{\varrho} + \\
&\qquad\qquad (-W^{\text{normal}}_{\|,m,k}(s)\sin(m\varphi) + W^{\text{skew}}_{\|,m,k}(s)\cos(m\varphi))\vec{e}_{\varphi} \Big] \\
&= \sum_{m=0}^{\infty} a^k m \varrho^{m-1} \Big[W^{\text{normal}}_{\|,m,k}(s)\big[\cos((m-1)\varphi)\vec{e}_x - \sin((m-1)\varphi)\vec{e}_y\big] \\
&\qquad\qquad W^{\text{skew}}_{\|,m,k}(s)\big[\sin((m-1)\varphi)\vec{e}_x + \cos((m-1)\varphi)\vec{e}_y\big]\Big].
\end{aligned} \tag{A.3}$$

For each mode we can define with the Panofsky-Wenzel theorem,

$$W_{\perp,m,k}(s) := -\int_{-\infty}^{s} W_{\|,m,k}(s')\mathrm{d}s' \tag{A.4}$$

in units of $\mathrm{V/(Asm^{m+k-1})}$. The lowest order multipoles acting coherently on the beam are

$$W_{\|}(s) \approx W_{\|,0,0}^{\mathrm{normal}}(s) \tag{A.5a}$$

$$W_{\perp,x}^{\mathrm{drive}}(s) \approx W_{\perp,1,1}^{\mathrm{normal}}(s) \tag{A.5b}$$

$$W_{\perp,y}^{\mathrm{drive}}(s) \approx W_{\perp,1,1}^{\mathrm{skew}}(s). \tag{A.5c}$$

For the transverse coherent beam dynamics one usually takes also into account one more term, i.e. $m = 2$, which is readily found from Eq. A.3,

$$\vec{W}_{\perp,2,k}(s) = a^k \left(W_{\perp,2,k}^{\mathrm{normal}}(s)(x\vec{e}_x - y\vec{e}_y) + W_{\perp,2,k}^{\mathrm{skew}}(s)(y\vec{e}_x + x\vec{e}_y) \right). \tag{A.6}$$

Finally, detuning and quadrupolar impedances can be interpreted as

$$W_{\perp}^{\mathrm{det}}(s) \approx W_{\perp,2,0}^{\mathrm{normal}}(s) \tag{A.7a}$$

$$W_{\perp}^{\mathrm{quad}}(s) \approx W_{\perp,2,2}^{\mathrm{normal}}(s). \tag{A.7b}$$

The two are quite different, as they describe the chamber asymmetry and the susceptibility of the beam to quadrupolar oscillation, respectively.

A generalized definition of multipolar transverse beam coupling impedance can be written as

$$\underline{Z}_{\perp,m,k}(\omega) = -\frac{v}{\omega M_m \tilde{M}_k} \int_{\mathrm{beam}} \underline{\vec{E}} \cdot \underline{\vec{J}}_{\mathrm{test},m}^{*} \mathrm{d}V \tag{A.8}$$

where $\underline{\vec{E}}$ is the solution of Maxwell's equations subject to the excitation by

$$\underline{\vec{J}}_{s,k} = \frac{M_k}{\pi a^2} \delta(a - \varrho) \cos(k\varphi) e^{-i\omega z/v} \vec{e}_z. \tag{A.9}$$

The two multipole moments are generally different, i.e. $M_m = q_2 a^m$ and $\tilde{M}_k = q_1 a^k$ and the test current distribution reads

$$\underline{\vec{J}}_{\mathrm{test},m} = \frac{\tilde{M}_m}{\pi a^2} \delta(a - \varrho) \cos(m\varphi) e^{-i\omega z/v} \vec{e}_z. \tag{A.10}$$

A similar expansion was also performed by Tsutsui [162], in the view of the interpretation of impedance bench measurements with displaced wires.

B The Hilbert Space $\mathscr{L}^2$ and associated Sobolev Spaces

We are following several mathematics textbooks in this chapter, particularly the one by Monk [56]. Hilbert spaces are linear spaces equipped with a scalar product, that are complete w.r.t. the norm induced by the scalar product. We look at functions $f, g : \Omega \to \mathbb{C}$ on an open Lipschitz domain $\Omega \subset \mathbb{R}^n$. The scalar product is defined as

$$(f,g) = \int_\Omega f(x) g^*(x) \mathrm{d}^n x, \tag{B.1}$$

which is linear in one and semi-linear in the other argument. The scalar product induces the norm

$$||f||_{\mathscr{L}^2(\Omega)} = \sqrt{(f,f)} = \sqrt{\int_\Omega |f(x)|^2 \mathrm{d}^n x}, \tag{B.2}$$

which is sometimes also written as $||f||_2$ for brevity. The Hilbert space $\mathscr{L}^2(\Omega)$ of functions $f : \Omega \to \mathbb{C}$ is defined as

$$\mathscr{L}^2(\Omega) = \{f : ||f||_2 < \infty\}, \tag{B.3}$$

where the involved (Lebesgue-) integration theory is mostly required to show the completeness of the space.

Sobolev spaces are Hilbert spaces of (weakly) partially differentiable functions, where the respective partial derivatives are also square integrable. All derivative operators in the following are to be understood in the weak sense. In particular one defines for $m \in \mathbb{N}$

$$\mathscr{H}^m(\Omega) = \{f \in \mathscr{L}^2(\Omega) \text{ and } \partial^{\mathbf{q}} f \in \mathscr{L}^2(\Omega) \ \forall |\mathbf{q}| \le m\}, \tag{B.4}$$

where $\mathbf{q}$ is a multi-index, i.e. *all* partial derivative combinations have to be square integrable.

Particular Sobolev spaces are relevant for Maxwell's equations in $\Omega \subset \mathbb{R}^3$, namely

$$\mathscr{H}^1(\Omega) = \{f \in \mathscr{L}^2(\Omega) \text{ and } \nabla f \in (\mathscr{L}^2(\Omega))^3\} \tag{B.5a}$$

$$\mathscr{H}^{\mathrm{curl}}(\Omega) = \{\vec{F} \in (\mathscr{L}^2(\Omega))^3 \text{ and } \nabla \times \vec{F} \in (\mathscr{L}^2(\Omega))^3\} \tag{B.5b}$$

$$\mathscr{H}^{\mathrm{div}}(\Omega) = \{\vec{F} \in (\mathscr{L}^2(\Omega))^3 \text{ and } \nabla \cdot \vec{F} \in \mathscr{L}^2(\Omega)\} \tag{B.5c}$$

and $\mathscr{L}^2(\Omega)$ itself, which is the space for the source charge density. These spaces are equipped with the Sobolev norms

$$||f||_{\mathscr{H}^1} = \sqrt{||f||_2^2 + ||\nabla f||_2^2} \tag{B.6a}$$

$$||\vec{F}||_{\mathscr{H}^{\text{curl}}} = \sqrt{||\vec{F}||_2^2 + ||\nabla \times \vec{F}||_2^2} \tag{B.6b}$$

$$||\vec{F}||_{\mathscr{H}^{\text{div}}} = \sqrt{||\vec{F}||_2^2 + ||\nabla \cdot \vec{F}||_2^2} \tag{B.6c}$$

We will furthermore define the spaces for Maxwells equations in 2D,

$$\mathscr{H}_{2\text{D}}^{\text{curl}}(\Omega) = \{\vec{F} \in (L^2(\Omega))^2 \text{ and } \hat{\text{B}}\vec{F} \in \mathscr{L}^2(\Omega)\} \tag{B.7a}$$

$$\mathscr{H}_{2\text{D}}^{\text{div}}(\Omega) = \{\vec{F} \in (L^2(\Omega))^2 \text{ and } \nabla_\perp \cdot \vec{F} \in \mathscr{L}^2(\Omega)\}, \tag{B.7b}$$

with the appropriate Sobolev norms.

In order to account for the boundary conditions, we need to define

$$\mathscr{H}_0^1(\Omega) = \{f \in H^1(\Omega) \text{ and } f|_{\partial\Omega} = 0\} \tag{B.8a}$$

$$\mathscr{H}_0^{\text{curl}}(\Omega) = \{\vec{F} \in \mathscr{H}^{\text{curl}}(\Omega) \text{ and } \vec{n} \times \vec{F}|_{\partial\Omega} = 0\}, \tag{B.8b}$$

i.e. spaces of functions where the Dirichlet boundary conditions have been applied a-priori.

Furthermore, for the treatment of SIBC a space

$$\mathscr{H}_{\text{imp}}^{\text{curl}}(\Omega) = \{\vec{F} \in \mathscr{H}^{\text{curl}}(\Omega) \text{ and } \vec{n} \times \vec{F} \in \mathscr{L}_t^2(\partial\Omega)\}. \tag{B.9}$$

is required, where $\mathscr{L}_t^2(\Omega)$ is the space of the surface tangential fields, i.e.

$$\mathscr{L}_t^2(\partial\Omega) = \{\vec{F} \in (\mathscr{L}^2(\partial\Omega))^3 \text{ with } \vec{n} \cdot \vec{F} = 0 \text{ almost everywhere on } \partial\Omega\}. \tag{B.10}$$

The norm on $\mathscr{H}_{\text{imp}}^{\text{curl}}(\Omega)$ is

$$||\vec{F}||^2_{\mathscr{H}_{\text{imp}}^{\text{curl}}(\Omega)} = ||\vec{F}||^2_{\mathscr{H}^{\text{curl}}(\Omega)} + ||\vec{n} \times \vec{F}||^2_{(\mathscr{L}^2(\partial\Omega))^3}. \tag{B.11}$$

Similarly as $\mathscr{H}^{\text{curl}}$ itself, this space can also be restricted to 2D.

C Radial Model Results for the SIS-100 Beam Pipe

As discussed in Sect. 3.3.2, the radial model is particularly suitable for low frequency highly relativistic impedance computation. It was employed to calculate the LF impedance of the SIS-100 beam pipe and bellows using EMS, see also [52, 79]. The following summarizes the LF impedance study, which is published in [52], for the SIS-100 beam pipe depicted in Fig. 1.2b. The pipe wall is made of a $d = 0.3\,\text{mm}$ stainless steel sheet, with cooling capillaries attached on the outside. The pipe has an elliptic shape, which is a trade-off for a large aperture and yet vertically small dipole magnet gaps. In order to study a worst case model, the conductivity was assumed for room temperature, i.e. $\kappa = 1.4\text{MS}$. Beyond the pipe wall, a poorly conducting ($\kappa = 10^{-2}\text{MS}$) frame, which summarized all outside equipment, has been attached. The discretization in CST EMS is done with 2 layers of tetrahedrons in the steel sheet, which should give accurate results up to the skin effect frequency (cf. Eq 3.21) The longitudinal and trans-

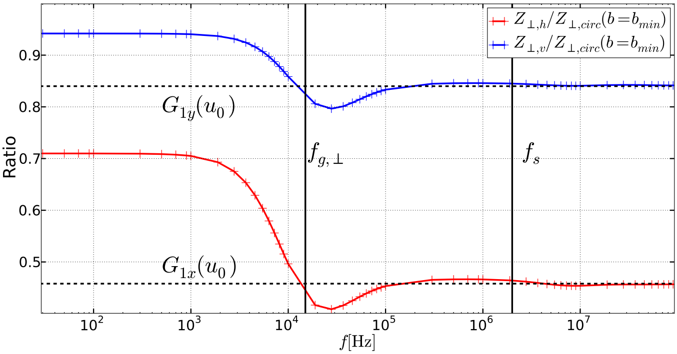

Figure C.1.: Numerically calculated ratios between the transverse resistive impedance (real part) of an elliptical and a circular beam pipe ($b = b_{\text{min}}$) with semi-axis radii $b_v = b_{\text{min}} = 40$ mm and $b_h = 2b_v$. $G_{1x}(u_0) \approx 0.46$ and $G_{1y}(u_0) \approx 0.84$ are the form factors calculated numerically by Eq. 6.6 of [163] with $u_0 = \operatorname{arccosh}(b_h/\sqrt{b_h^2 - b_v^2})$, see also [52].

verse impedance are obtained by Eqs. 3.38, where the power loss (Eq. 3.37) is directly evaluated by a post-processing template in EMS.

The impedance of such an elliptical pipe can also be accessed by form factor theory, e.g. the one by Gluckstern *et al.* [163]. However, form factor theory is valid only in the thick wall regime, i.e. above the skin effect frequency. Figure C.1 shows a comparison between the analytically calculated form factors and the numerically obtained ones for different frequencies. The numerical form factors are the transverse impedance ratio between a plain, thin, elliptic pipe and a round pipe with the radius being the vertical (smaller) semi-axis radius.

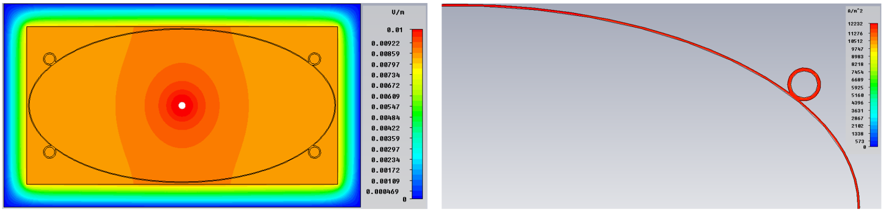

(a) $f = 1$ kHz, $f < f_{g,\|}$, $E_{max,disp} = 0.01$ V/m

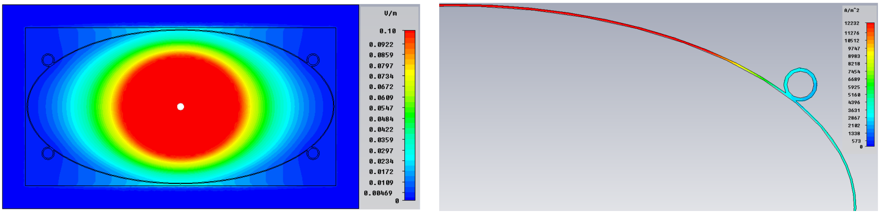

(b) $f = 100$ kHz, $f_{g,\|} < f < f_s$, $E_{max,disp} = 0.1$ V/m

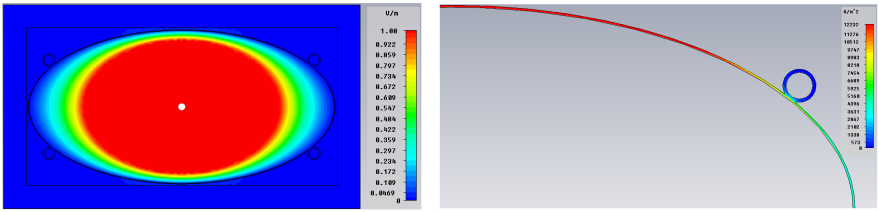

(c) $f = 3$ MHz, $f > f_s$,$E_{max,disp} = 1$ V/m

Figure C.2.: Longitudinal electric field (left) and wall current density (right) resulting from a monopolar excitation. The color scale is adapted for each frequency [52].

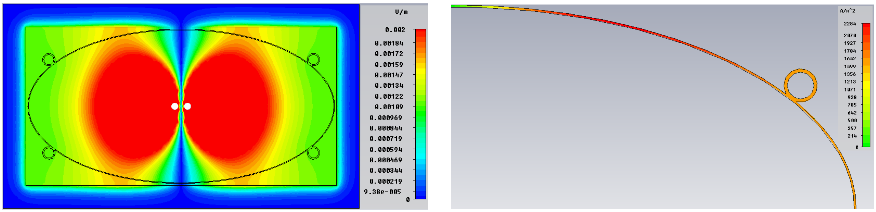

(a) $f = 10$ kHz,$f < f_{g,\perp}$, $E_{max,disp} = 0.002$ V/m

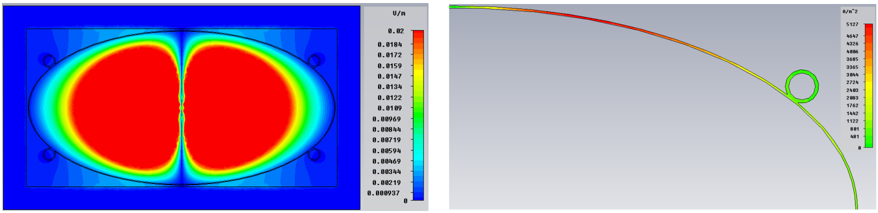

(b) $f = 300$ kHz, $f_{g,\|} < f < f_s$, $E_{max,disp} = 0.02$ V/m

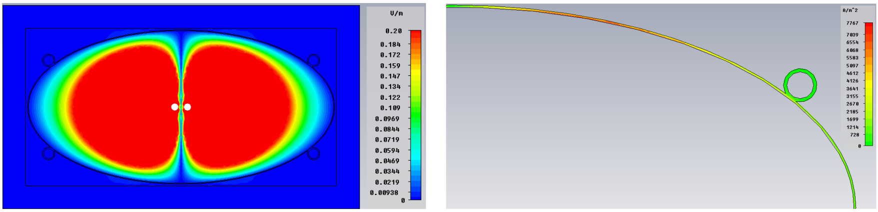

(c) 3 MHz, $f > f_s$,$E_{max,disp} = 0.2$ V/m

Figure C.3.: Longitudinal electric field (left) and wall current density (right) resulting from a dipolar excitation. The color scale is adapted for each frequency [52].

The longitudinal electric field and the wall current density can be seen for monopolar and dipolar excitation in Figs. C.2 and C.3. The frequency of onset of the wall current is given for a circular thin pipe in the radial model by [52]

$$f_{g,\|} = \frac{1}{2\pi\mu\kappa bd \ln(h_2/h)} \tag{C.1a}$$

$$f_{g,\perp} = \frac{1}{\pi\mu\kappa bd} \tag{C.1b}$$

for monopolar (longitudinal impedance) and dipolar (transverse) excitation, respectively. Here, h_2 is the radius of an outer PEC boundary condition with $h_2 \gg h$. The two frequencies are quite different, since for the monopole current, the magnetic flux linked between the beam and wall current, is located outside the pipe (cf. Figs. 3.8, 3.9). Contrarily, the dipole field flux is mostly inside the pipe and leaks to the outside at low frequency only when there is a material in which it could drive a current.

The Figs. C.2 and C.3 illustrate the three different regimes:

(a) $f < f_g$, The image current in the pipe wall is very small and "DC-like" distributed. The electromagnetic fields can penetrate through the pipe and outside equipment affects the impedance.

(b) $f_g < f < f_s$, The wall current is almost as large as the beam current and shields the electromagnetic fields almost completely. The real part of the longitudinal impedance is the Ohmic resistance of the pipe.

(c) $f > f_s$, The wall current is on the inner surface of the pipe and shields the electromagnetic fields completely. The impedance can be computed using the SIBC.

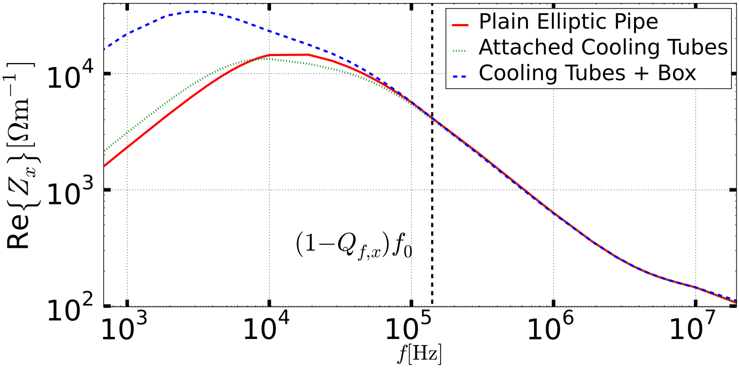

Figure C.4.: Numerically obtained horizontal impedance of the SIS100 pipe of 1m lengthy [52]. The dashed vertical line indicates the lowest coherent betatron sideband.

Finally the transverse impedance for those different setups is plotted in Fig. C.4. The vertical black dashed line indicates the lowest left betatron sideband at $(1-Q_f)f_0$, i.e. the lowest frequency relevant for a transverse beam instability. As visible in the plot, there is an influence of outside equipment only at frequencies below this line. Therefore, it was concluded, that the impact of equipment beyond the pipe wall is of no concern to the beam stability.

D The Most Simplified Case for 2D Beam Coupling Impedance Calculation with FIT

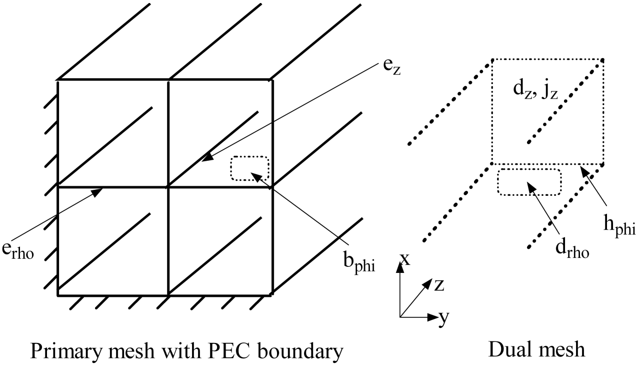

Figure D.1.: Simplest imaginable mesh for beam coupling impedance computation with FIT, see also [164].

Applying the MGE (4.10a)-(4.10d) to a strongly simplified mesh as shown in Fig. D.1 results in the following equations:

$$-i\frac{\omega}{v}\Delta z\underline{\widehat{\mathbf{e}}}_{\varrho} - \underline{\widehat{\mathbf{e}}}_{z} = -i\omega\underline{\widehat{\widehat{\mathbf{b}}}}_{\varphi} \tag{D.1a}$$

$$4\underline{\widehat{\mathbf{h}}}_{\varphi} - i\omega\underline{\widehat{\widehat{\mathbf{d}}}}_{z} = \underline{\widehat{\widehat{\mathbf{j}}}}_{s,z} \tag{D.1b}$$

$$-i\frac{\omega}{v}\Delta\tilde{z}\underline{\widehat{\widehat{\mathbf{d}}}}_{z} + 4\underline{\widehat{\widehat{\mathbf{d}}}}_{\varrho} = \mathbf{q}_e = \frac{\Delta\tilde{z}}{v}\underline{\widehat{\widehat{\mathbf{j}}}}_{s,z} \tag{D.1c}$$

These three equations for the three unknowns $\underline{\widehat{\mathbf{e}}}_{z}, \underline{\widehat{\mathbf{e}}}_{\varrho}$ and $\underline{\widehat{\widehat{\mathbf{b}}}}_{\varphi}$ can be solved using the material operators 4.15,

$$\begin{aligned} 4\underline{\widehat{\mathbf{e}}}_{z} + \omega^2\mathbf{M}_{\mu}^{\varphi}\mathbf{M}_{\varepsilon}^{z}(\mathbf{I} - \frac{\Delta z\Delta\tilde{z}}{v^2}\mathbf{M}_{\mu^{-1}}^{\varphi}\mathbf{M}_{\varepsilon^{-1}}^{\varrho})\underline{\widehat{\mathbf{e}}}_{z} \\ = i\omega\mathbf{M}_{\mu}^{\varphi}(\mathbf{I} - \frac{\Delta z\Delta\tilde{z}}{v^2}\mathbf{M}_{\mu^{-1}}^{\varphi}\mathbf{M}_{\varepsilon^{-1}}^{\varrho})\underline{\widehat{\widehat{\mathbf{j}}}}_{e,z}. \end{aligned} \tag{D.2}$$

Inserting $A_{\varphi} = \Delta\varrho\Delta z$ and $\tilde{A}_{\varrho} = \Delta\tilde{\varphi}\Delta\tilde{z}$, the following mimetic correspondence to the relativistic relation $1 - 1/\beta^2 = -1/(\beta\gamma)^2$ is found

$$\boxed{\mathbf{I} - \frac{\Delta z \Delta\tilde{z}}{v^2}\mathbf{M}^{\varphi}_{\mu^{-1}}\mathbf{M}^{\varrho}_{\varepsilon^{-1}} = -\frac{1}{\beta^2\gamma^2}\mathbf{I},} \tag{D.3}$$

independent of the mesh lengths. Thus, Eq. D.2 can be solved as

$$\underline{\widehat{\mathbf{e}}}_z = \frac{-i\omega\mu_0\Delta z}{4\beta^2\gamma^2 - \omega^2\delta_{\perp}^2/c^2}\underline{\widehat{\widehat{\mathbf{j}}}}_{e,z}. \tag{D.4}$$

for equal transverse mesh lengths $\delta_{\perp} = \Delta x = \Delta\tilde{x} = \Delta y = \Delta\tilde{y}$. Equation D.4 is the mimetic correspondence to the longitudinal space charge impedance. It fulfills all its qualitative properties, i.e. $\propto \beta^{-2}\gamma^{-2}$, $\propto \omega$, negative imaginary and a cut-off frequency. Furthermore, the factor 4 in Eq. D.2 originates from the difference stencil of the transverse Laplacian. Obviously, the geometry factor g (cf Eq. 3.44) is poorly reproduced by staircase FIT for curved structures.

E Scattering Parameters and Vector Network Analysis

Voltages and currents cannot always be defined in RF-structures, since the respective line integral is not independent of the path. Thus, complex wave amplitudes are used instead. We restrict ourselves here to TEM modes on ports with identical characteristic impedance Z_c. For each port $k = 1...N$ of such an RF structure, the TEM wave amplitude is defined as

$$a_k := \frac{1}{2\sqrt{Z_c}}(U_k + Z_c I_k) \tag{E.1a}$$

$$b_k := \frac{1}{2\sqrt{Z_c}}(U_k - Z_c I_k) \tag{E.1b}$$

for the ingoing and outgoing waves, where U_k and I_k are the voltage and inflowing current phasor at port k, respectively. The amplitudes are in linear units of $\sqrt{\mathrm{VA}}$. The vectors of incident and reflected waves are connected by the scattering matrix $\mathbf{S} = [S_{ik}]$

$$b_i = \sum_{k=1}^{N} S_{ik} a_k. \tag{E.2}$$

Reversely, the S-parameters are obtained by

$$S_{ik} = \left.\frac{b_i}{a_k}\right|_{a_m = 0\ \forall m \neq k}. \tag{E.3}$$

In this way, S-parameters can be measured by means of a Vector Network Analyzer (VNA). A stimulus a_k is applied in port k and the outgoing waves b_i in port i are measured. Such a measurement requires that all ports are matched and that the VNA is calibrated at the plane where the S-matrix is defined.

For the measurements performed during this thesis, a Rohde & Schwarz ZNB4 (9kHz-4.5GHz) VNA [141] was purchased at GSI. The advantage of such a 4 port VNA is that symmetric S-parameters can be directly recorded. Also, the complex impedance as function of the frequency can be determined from the S_{11}-parameter, provided the impedance can be seen as a lumped element and the reflection is not close to 100%. An example of such a direct impedance measurement can be seen in Fig. F.4.

F Data of the FAIR SIS-100 Synchrotron

The relevant technical data of the SIS-100 are in [4] and follow-up reports, as particularly [156]. Note that some of these data are still subject to design changes.

Table F.1.: Parameters for the SIS-100 high intensity single proton bunch scenario.

Proton scenario	Symbol	Value
Total pipe length	l	1083.6 m
Cryogenic pipe length	l_c	$\approx$ 554 m
Top energy	E_{top}	28.8 GeV
Velocity	β	0.983
Particle number	N_{b}	$2 \cdot 10^{13}$
Bunch length	σ_s	3.7 m
Freq. associated with bunch length	$\sigma_f = \frac{\beta c}{2\pi\sigma_s}$	12.7 MHz
Revolution frequency	f_0	274 kHz

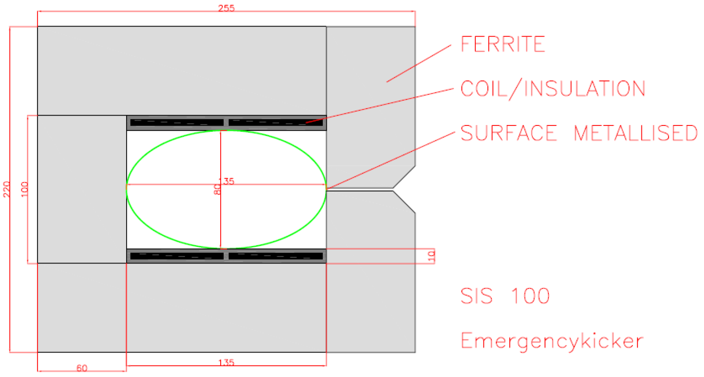

Figure F.1.: Technical Drawing of the SIS100 emergency kicker. Courtesy of U. Blell, GSI. Recent design changes, however, do not arrange for a beam pipe anymore. Additionally, there shall be 2 yoke gaps, each filled with a copper strip.

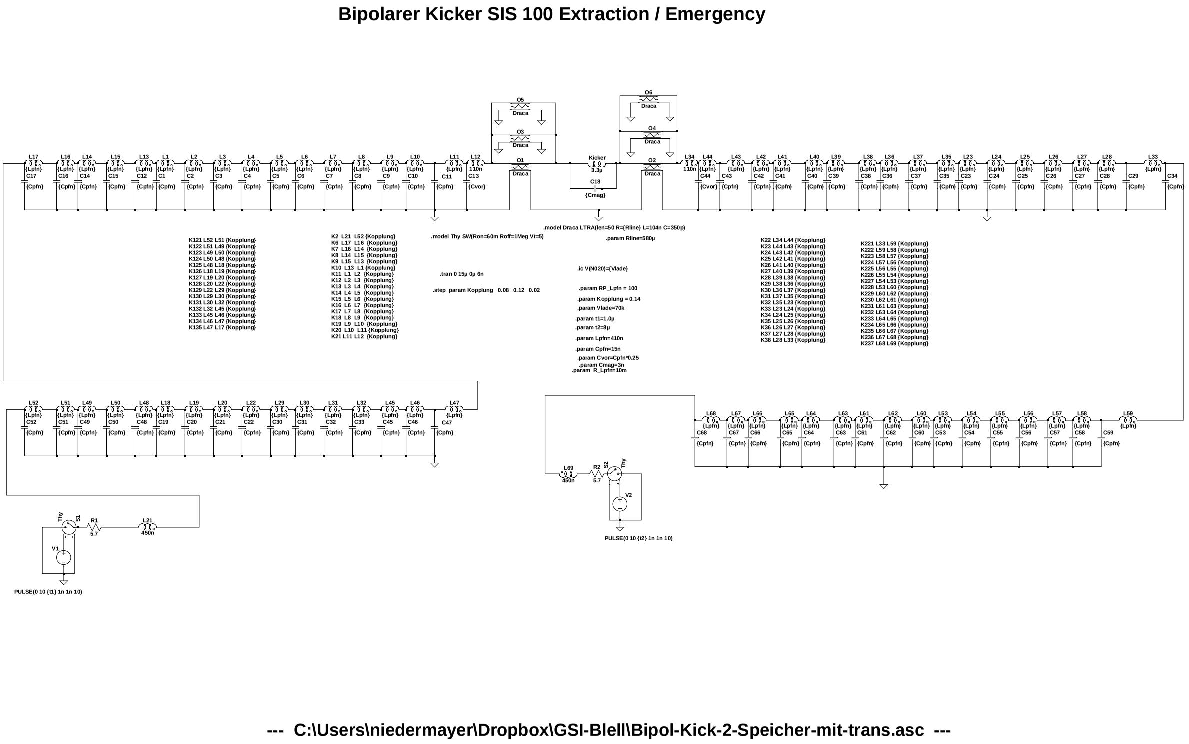

Figure F.2.: Bipolar extraction/emergency kicker supply network (PFN). Courtesy of U.Blell, GSI.

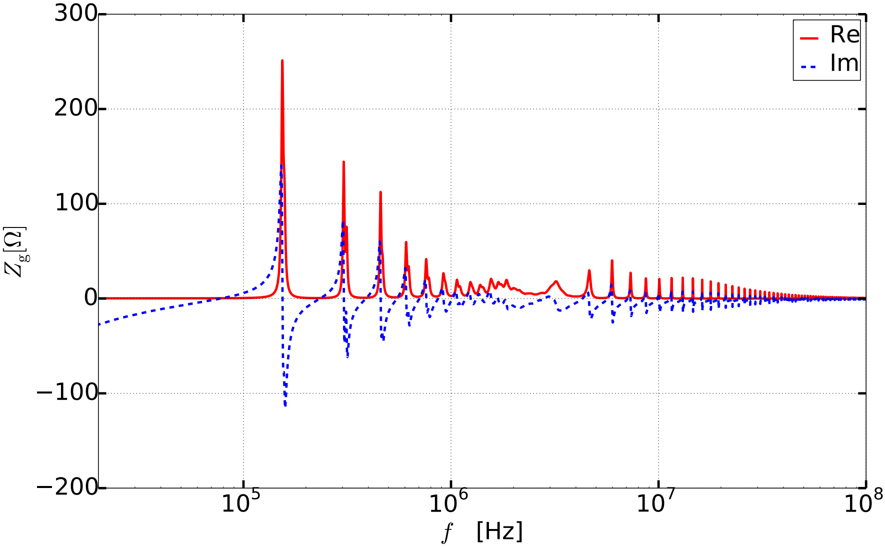

Figure F.3.: Impedance Z_g of the PFN in Fig. F.2 at the kicker terminals, simulated with LT-SPICE [160].

Table F.2.: Relevant parameters for the SIS-100 to SIS-300 transfer kicker.

SIS100 transfer kicker	Symbol	Value
Kick direction		Vertical monopolar
Coil turns	N_{coil}	2
Coil inductance (specified)	L	$3.33\,\mu$H
Material	Ferroxcube	8C11 [165]
Outside Height	h_v	20 cm
Outside Width	h_h	23 cm
Inside Height	b_v	8 cm
Inside Width	b_h	11 cm
Ferrite thickness	D	6 cm
Yoke gap thickness	G	2.8 mm
Yoke gap material	Copper, κ	58 MS/m
Module length	l	80 cm
Number of modules	N_M	6
Beam deflection field	B	120 mT

Table F.3.: Relevant parameters for the SIS-100 extraction/emergency kicker.

SIS100 extr./emerg. kicker	Symbol	Value
Kick direction		Vertical bipolar
Coil turns	N_{coil}	2
Coil inductance (specified)	L	$3.3\,\mu$H
Material	Ferroxcube	8C11 [165]
Outside Height	h_v	22 cm
Outside Width	h_h	25.5 cm
Inside Height	b_v	10 cm
Inside Width	b_h	13.5 cm
Ferrite thickness	D	6 cm
Gap thickness	G	2.8 mm
Gap material	Copper, κ	58 MS/m
Module length	l	75 cm
Number of modules	N_M	8
Beam deflection field	B	114 mT

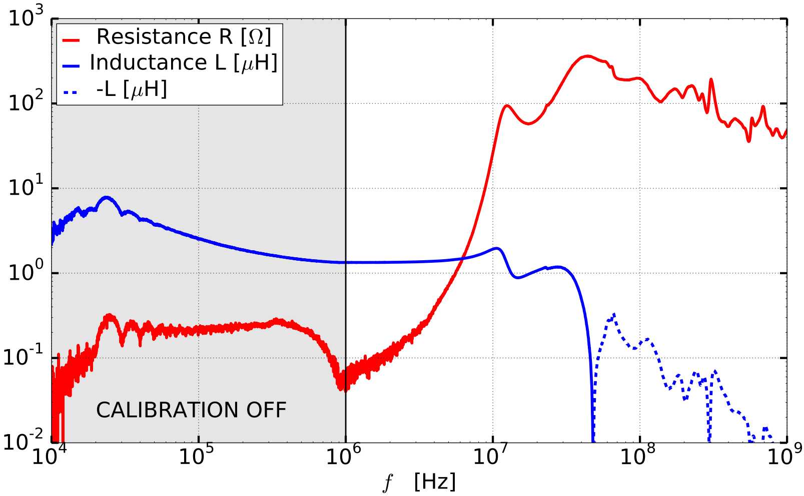

Figure F.4.: SIS-18 kicker (Fig. 1.3) coil inductance and resistance measurement at the PFN terminal. The zero-crossing of the inductance at ≈ 45 MHz marks the limit of validity of the transformer circuit model. The specified inductance is $2\,\mu$H.

G Lists

List of Figures

List of Tables

Bibliography

[1] K. Wille, *The Physics of Particle Accelerators*. Oxford University Press, 2000. 1, 3, 19, 20, 137

[2] L. Landau, "On the vibration of the electronic plasma," Translated by E. Lifshitz, 1946. 1

[3] B. Franczak, "SIS 18 Parameterliste, 10.09.1987," Darmstadt, 1987. 1

[4] P. Spiller et al., "FAIR Technical Design Report," GSI, Darmstadt, Tech. Rep., 2008. 1, 131

[5] O. Brüning, P. Collier, P. Lebrun, S. Myers, R. Ostojic, J. Poole, and P. Proudlock, "LHC Design Report," CERN, Tech. Rep., 2004. 1

[6] S. Maury, W. Oelert, W. Bartmann, P. Belochitskii, H. Breuker, F. Butin, C. Carli, T. Eriksson, S. Pasinelli, and G. Tranquille, "ELENA: the extra low energy anti-proton facility at CERN," Springer, Tech. Rep., 2014. 2

[7] "www.fcc.web.cern.ch," 2015. 2, 78

[8] M. Benedikt, B. Goddard, D. Schulte, F. Zimmermann, and M. J. Syphers, "FCC-hh Hadron Collider - Parameter Scenarios and Staging Options," in *Proc. of IPAC*, 2015. 2

[9] A. K. Jain, "Basic Theory of Magnets," in *CERN Accelerator School: Measurement and Alignment of Accelerator and Detector Magnets*, no. 2, 1997, pp. 1–26. 3

[10] E. Courant and H. Snyder, "Theory of the alternating-gradient synchrotron," *Annals of Physics*, vol. 3, pp. 1–48, 1958. 4, 15

[11] H. Klingbeil, U. Laier, and D. Lens, *Theoretical Foundations of Synchrotron and Storage Ring RF-Systems*. Heidelberg: Springer, 2015. 4, 19

[12] B. Salvant et al., "LHC impedance model: experience with high intensity operation in the LHC," in *Proc. of ICFA-HB*, 2012. 5

[13] "LHC Beam Pipe," 1997. [Online]. Available: http://cds.cern.ch/record/39110 6

[14] N. Mounet, “The LHC Transverse Coupled Bunch Instability,” Ph.D. dissertation, EPFL Lausanne, 2012. 6, 54

[15] V. Kornilov and O. Boine-Frankenheim, “Transverse Instability of Coasting Beam in SIS18,” GSI, Tech. Rep., 2009. 6, 107, 138

[16] U. Niedermayer, “Coupling impedance calculation for a thin layered beampipe,” Diplomarbeit, TU Darmstadt, 2011. 6, 50

[17] M. Balk, “Feldsimulationen starrer Teilchenstrahlen beliebiger Geschwindigkeit und deren Anwendung in der Schwerionenbeschleunigerphysik,” Ph.D. dissertation, TU-Darmstadt, Cuvillier Verlag Göttingen, 2005. 6, 22

[18] J. C. Maxwell, “A Dynamical Theory of the Electromagnetic Field,” 1865. 9

[19] ——, “A Treatise on Electricity & Magnetism,” *Dover Publications*, 1873. 9

[20] O. Heaviside, “On the Forces, Stresses, and fluxes of energy in the Electromagnetic Field,” *Philosophical Transactions of the Royal Society of London*, vol. 183, pp. 423–480, 1892. 9

[21] A. Waser, “On the Notation of Maxwell’s Field Equations,” *AW-Verlag*, 2000. 9

[22] S. Humphries, *Charged Particle Beams*. John Wiley & Sons, Incorporated, 1990. 10

[23] A. Chao, *Lecture Notes on Topics in Accelerator Physics*, 2002. 10, 27

[24] J. P. Verboncoeur, “Particle simulation of plasmas: review and advances,” *Plasma Physics and Controlled Fusion*, vol. 47, no. 5A, pp. A231–A260, 2005. 10

[25] V. G. Vaccaro, “Longitudinal Instability of a Coasting Beam above Transition, due to the action of Lumped Discontinuities,” CERN report ISR-RF/66-35, Tech. Rep., 1966. 11

[26] O. Boine-Frankenheim and V. Kornilov, “Implementation and Validation of Space Charge and Impedance Kicks in the Code Patric for Studies of Transverse Coherent Instabilities in the Fair Rings,” in *Proc. of ICAP*, 2006. 11

[27] G. Rumolo and E. Metral, “Multi-Bunch Simulations with HEADTAIL,” in *Proc. of PAC*, 2009. 11

[28] S. Chattopahdyay, “Some Fundamental Aspects of Fluctuations and Coherence in Charged-Particle Beams in Storage Rings,” in *CERN 84-11*, 1984. 12

[29] R. Unbehauen, *Systemtheorie*. München, Wien: Oldenbourg, 1983. 13

[30] K. Küpfmüller, *Einführung in die theoretische Elektrotechnik*. Springer, 1932. 13

[31] H. Wiedemann, *Particle Accelerator Physics*. Berlin Heidelberg: Springer, 2007. 15, 108, 109

[32] M. J. Syphers and D. A. Edwards, *An Introduction to the Physics of High energy Accelerators*. Weinheim: Wiley-VCH Verlag GmbH, 2004. 15

[33] L. Deniau et al., “http://madx.web.cern.ch/madx/,” 2015. 16

[34] A. Parfenova, “Linear and nonlinear Response Matrix and its application to the SIS18 synchrotron,” Ph.D. dissertation, Johann Wolfgang Göthe-Universität Frankfurt am Main, 2008. 16

[35] M. Reiser, *Theory and Design of Charged Particle Beams*. Weinheim, Germany: Wiley-VCH Verlag GmbH, 2008. 16

[36] A. Burov and V. Danilov, “Suppression of transverse bunch instabilities by asymmetries in the chamber geometry,” *Physical Review Letters*, vol. 82, no. 11, p. 11, 1999. 19, 96

[37] T. Weiland and R. Wanzenberg, “Wake Fields and Impedances,” in *CERN Accelerator School (CCAS)*, 1993. 21, 29, 104

[38] L. Palumbo, V. G. Vaccaro, and M. Zobov, “Wake Fields and Impedance,” in *Cern Accelerator School*, 1994. 21

[39] M. Balk, R. Schuhmann, and T. Weiland, “Open boundaries for particle beams within fit-simulations,” *Nucl. Instrum. Meth. Section A*, vol. 558, no. 1, pp. 54–57, mar 2006. 22

[40] “CST Studio Suite. www.cst.com,” 2013. [Online]. Available: www.cst.com 22, 44, 55, 93

[41] J. Haissinski, “Exact Longitudinal Equilibrium Distribution of Stored Electrons in the Presence of Self-Fields,” *Il Nuovo Cimento B*, vol. 18, no. 2, pp. 72–82, 1973. 23

[42] K. Y. Ng, *Physics of Intensity Dependent Beam Instabilities*. Singapore: World Scientific, 2006. 23, 105, 108, 109

[43] A. Al-Khateeb, R. Hasse, O. Boine-Frankenheim, W. Daqa, and I. Hofmann, "Transverse resistive wall impedances and shielding effectiveness for beam pipes of arbitrary wall thickness," *Physical Review Special Topics - Accelerators and Beams*, vol. 10, no. 6, p. 064401, jun 2007. 23, 46

[44] W. K. H. Panofsky and W. A. Wenzel, "Some Considerations Concerning the Transverse Deflection of Charged Particles in Radio-Frequency Fields," *Review of Scientific Instruments Volume 27*, no. May 2011, pp. 967–968, 1956. 27

[45] T. Weiland, "Comment on Wake Field Computation in the Time Domain," *Nucl. Instrum. Meth.*, vol. 216, pp. 31–34, 1983. 29

[46] O. Napoly, "The Wake Potentials from the Fields on the Cavity Boundary," *Particle Accelerators*, vol. 36, pp. 15–23, 1991. 29

[47] O. Napoly, Y. H. Chin, and B. Zotter, "A generalized method for calculating wake potentials," *Nucl. Instrum. Meth. Section A*, vol. 334, no. 2-3, pp. 255–265, oct 1993. 29

[48] H. Henke and W. Bruns, "Calculation of Wake Potentials in general 3D structures," in *Proc. of EPAC*, no. 8, 2006, pp. 2170–2172. 29

[49] I. Zagorodnov, "Indirect methods for wake potential integration," *Physical Review Special Topics - Accelerators and Beams*, vol. 9, no. 10, p. 102002, oct 2006. 29

[50] N. Mounet and E. Metral, "Electromagnetic field created by a macroparticle in an infinitel long and axisymmetric multilayer beam pipe," *CERN-BE-2009-039*, 2009. 32, 51, 78, 100

[51] H. Hahn, "Matrix solution for the wall impedance of infinitely long multilayer circular beam tubes," *Physical Review Special Topics - Accelerators and Beams*, vol. 13, no. 1, p. 012002, jan 2010. 32, 42

[52] U. Niedermayer and O. Boine-Frankenheim, "Analytical and numerical calculations of resistive wall impedances for thin beam pipe structures at low frequencies," *Nucl. Instrum. Meth. Section A*, vol. 687, pp. 51–61, 2012. 32, 42, 44, 51, 100, 123, 124, 125, 126, 139

[53] S. A. Heifets and S. A. Kheifets, “Coupling impedance in modern accelerators,” *SLAC*, 1991. 32

[54] N. Biancacci, V. G. Vaccaro, E. Métral, B. Salvant, M. Migliorati, and L. Palumbo, “Impedance studies of 2D azimuthally symmetric devices of finite length,” *Physical Review Special Topics - Accelerators and Beams*, vol. 17, no. 2, p. 021001, feb 2014. 32

[55] T. Flisgen, J. Heller, and U. van Rienen, “Computation of Eigenmodes in Long and Complex Accelerating Structures by Means of Concatenation Strategies,” in *Proc. of IPAC*, Dresden, 2014. 32

[56] P. Monk, *Finite Element Methods for Maxwell’s Equations*. Oxford University Press, 2003. 33, 64, 121

[57] “Helmholtz Decomposition.” [Online]. Available: https://en.wikipedia.org/wiki/Helmholtz_decomposition 33

[58] Y. Tong, S. Lombeyda, A. N. Hirani, and M. Desbrun, “Discrete multiscale vector field decomposition,” *ACM Transactions on Graphics*, vol. 22, no. 3, p. 445, 2003. 33

[59] U. Niedermayer, L. Eidam, and O. Boine-Frankenheim, “Analytic modeling, simulation and interpretation of broadband beam coupling impedance bench measurements,” *Nucl. Instrum. Meth. Section A*, vol. 776, pp. 129–143, 2015. 34, 36, 44, 45, 55, 56, 66, 81, 83, 84, 85, 91, 93, 95, 98, 99, 117, 137, 138

[60] P. Drude, “Zur Elektronentheorie der Metalle,” *Annalen der Physik*, 1900. 35

[61] “Amidon Material 43,” 2013. [Online]. Available: http://www.amidon.de/contents/de/d542.html 36

[62] W. Barry, “A Broad-Band, Automated, Stripline Technique for the Simultaneous Measurement of Complex Permittivity and Permeability,” *IEEE Transactions on Microwave Theory and Techniques*, vol. MIT-34, no. 1, 1986. 36

[63] F. Caspers, M. Morvillo, C. Gonzalez, and D. Misha, “Measurements of Complex Permeability and Permittivity of Ferrites for the LHC Injection Kicker,” *LHC Project Note 203*, 1999. 36

[64] C. Völlinger, F. Caspers, and E. Jensen, “Permittivity and Permeability Measurement Methods for Particle Accelerator Related Materials,” in *Proc. of IPAC 2014*, 2014, pp. 3893–3895. 36

[65] A. Stadler, “Messtechnische Bestimmung und Simulation der Kernverluste in weichmagnetischen Materialien,” Ph.D. dissertation, Erlangen, 2009. 37

[66] H. Klingbeil, “Ferrite cavities,” *arXiv:1201.1154v1*, pp. 1–19, 2011. 37

[67] K. Klopfer, “Computation of Complex Eigenmodes for Resonators Filled With Gyrotropic Materials,” Ph.D. dissertation, TU-Darmstadt, 2014. 37, 59

[68] K. Klopfer, U. Niedermayer, H. Klingbeil, W. Ackermann, H. G. König, and T. Weiland, “Measurement of the magnetic material properties for ferrite-loaded cavities,” *Physical Review Special Topics - Accelerators and Beams*, vol. 18, pp. 1–10, 2015. 37

[69] J. Eberhardt, F. Caspers, and C. Vollinger, “Ferrite Material Characterization in a Static Bias Field for the Design of a Tunaeable Cavity,” in *Proc. of IPAC 2014*, no. 2, 2014, pp. 6–8. 37

[70] T. B. A. Senior and J. L. Volakis, *Approximate boundary conditions in electromagnetics*. London: The Institution of Electrical Engineers, 1995. 37

[71] K. Schmidt and A. Chernov, “Robust transmission conditions of high order for thin conducting sheets in two dimensions,” *IEEE Transactions on Magnetics*, vol. 50, pp. 1–4, 2014. 37

[72] H. K. Dirks, “Quasi-stationary fields for microelectronic applications,” *Springer Electrical Engineering*, vol. 79, no. 2, pp. 145–155, 1996. 39, 40

[73] M. Clemens and T. Weiland, “Regularization of eddy-current formulations using discrete grad-div operators,” *IEEE Transactions on Magnetics*, vol. 38, no. 2, pp. 569–572, 2002. 41

[74] W. Shin and S. Fan, “Accelerated solution of the frequency-domain Maxwells equations by engineering the eigenvalue distribution of the operator,” *Optics Express*, vol. 21, no. 19, p. 22578, 2013. 41

[75] I. Munteanu, “Tree-cotree condensation properties,” *International Compumag Society Newsletter*, vol. 9, no. 1, pp. 10–14, 2002. 41

[76] C. G. Darwin, “The Dynamical Motions of Charged Particles,” *Philosophical Magazine*, vol. 6, no. 233, pp. 537–551, 1920. 42

[77] P. Degond and P.-A. Raviart, “An analysis of the Darwin model of approximation to Maxwell ’ s equations .” *Forum Mathematicum*, vol. 4, pp. 13–44, 1992. 42

[78] G. Waldschmidt and A. Taflove, “The determination of the effective radius of a filamentary source in the FDTD mesh,” *IEEE Microwave and Guided Wave Letters*, vol. 10, no. 6, pp. 217–219, 2000. 43, 61

[79] U. Niedermayer, “Low frequency impedance calculations for the SIS18 beam pipe bellow,” GSI-Darmstadt (unpublished), Tech. Rep., 2014. 44, 123

[80] L. Vos, “The transverse impedance of a cylindrical pipe with arbitrary surface impedance,” *CERN-AB-2003-005 ABP*, 2003. 45, 101

[81] G. Nassibian and F. Sacherer, “Methods for Measuring Transverse Coupling Impedances,” *Nucl. Instrum. Meth.*, vol. 159, no. 6, pp. 21–27, 1978. 45, 96, 112

[82] N. Mounet and E. Metral, “Impedances of Two dimensional Multilayer Cylindrical and Flat Chambers in the Non-Ultrarelativistic Case,” in *Proc. of ICFA-HB*, Morschach, 2010, p. TUO1C02. 45

[83] K. Bane and G. Stupakov, “Using surface impedance for calculating wakefields in flat geometry,” *Physical Review Special Topics - Accelerators and Beams*, vol. 18, no. 3, pp. 1–6, 2015. 45

[84] K. Schindl, “Space Charge,” in *Cern Accelerator School*, 2000. 46

[85] R. Gluckstern, “Analytic methods for calculating coupling impedances,” in *Cern Accelerator School*. Cern Accelerator School, 2000. 46, 47, 48, 50

[86] A. Al-Khateeb, O. Boine-Frankenheim, R. Hasse, and I. Hofmann, “Longitudinal impedance and shielding effectiveness of a resistive beam pipe for arbitrary energy and frequency,” *Physical Review E*, vol. 71, no. 2, p. 026501, feb 2005. 46

[87] A. Al-Khateeb, R. W. Hasse, and O. Boine-Frankenheim, “Comparison of the longitudinal coupling impedance from different source terms,” *Nucl. Instrum. Meth. Section A*, vol. 593, pp. 171– 176, 2008. 50

[88] A. W. Chao, *Physics of Collective Beam Instabilities in High Energy Accelerators*. New York: John Wiley & Sons, Incorporated, 1993. 51

[89] B. Zotter and S. A. Kheifets, *Impedances and Wakes in High-Energy Particle Accelerators*. Singapore: World Scientific Publishing Co. Pte. Ltd., 1998. 51, 104

[90] “Wolfram Mathematica 9.0.” 2013. [Online]. Available: www.wolfram.com 51

[91] E. Gjonaj, T. Lau, and T. Weiland, "Computation of Short Range Wake Fields with PBCI," *ICFA Beam Dynamics Newsletter*, no. 37, 2005. 53

[92] R. L. Gluckstern and S. S. Kurennoy, *Impedance Calculation, Frequency Domain, Handbook of Accelerator Physics and Engineering*, 2nd ed., A. Chao, K. H. Mess, M. Tigner, and F. Zimmermann, Eds. World Scientific Publishing Co. Pte. Ltd., 2013. 53

[93] K. Yee, "Numerical solution of initial boundary value problems involving Maxwell's equations in isotropic media," *Antennas and Propagation, IEEE Transactions on*, vol. 14, no. 3, pp. 302–307, 1966. 54

[94] T. Weiland, "Eine Methode zur Lösung der Maxwellschen Gleichungen für sechskomponentige Felder auf diskreter Basis," *Electronics and Communication (AEÜ)*, vol. 31, pp. 116–120, 1977. 54, 57

[95] H. Kawaguchi and T. Honma, "On the wake fields reaction force which acts on electrons in an accelerator cavity," *Nucl. Instrum. Meth. Section A*, vol. 363, pp. 145–152, 1995. 54

[96] K. Fujita, H. Kawaguchi, I. Zagorodnov, and T. Weiland, "Time domain wake field computation with boundary element method," *IEEE Trans. Nuclear Science*, vol. 53, no. 2, 2006. 54

[97] K. Fujita, H. Kawaguchi, and S. Nishiyama, "Scattered-Field Time Domain Boundary Element Method and Its Application to Transient Electromagnetic Field Simulation in," *IEICE Trans. Electron.*, vol. 90, no. 2, pp. 265–274, 2007. 54

[98] E. Gjonaj, T. Lau, T. Weiland, and D. Darmstadt, "Wakefield Computations with the PBCI Code using a Non-Split finite Volume Method," in *Proc. of PAC 2009*, 2009. 54

[99] P. Thoma, "Zur numerischen Lösung der Maxwellschen Gleichungen im Zeitbereich," Ph.D. dissertation, TU-Darmstadt, 1997. 54, 55

[100] R. Courant, K. Friedrichs, and H. Lewy, "Über die partiellen Differenzengleichungen der mathematischen Physik," *Mathematische Annalen*, vol. 100, no. 1, pp. 32–74, 1928. 55

[101] F. Edelvik, R. Schuhmann, and T. Weiland, "A general stability analysis of FIT/FDTD applied to lossy dielectrics and lumped elements," *International Journal of Numerical Modelling: Electronic Networks, Devices and Fields*, vol. 17, no. 4, pp. 407–419, 2004. 55

[102] S. Gutschling, H. Krüger, and T. Weiland, "Time-domain simulation of dispersive media with the finite integration technique," *Int. J. Numer. Model.*, no. 13, pp. 329–348, 2000. 55

[103] R. Hiptmair, F. Krämer, and J. Ostrowski, "A robust Maxwell formulation for all frequencies," *IEEE Transactions on Magnetics*, vol. 44, no. 6, pp. 682–685, 2008. 57

[104] T. Egenolf, "Impedance of the beam pipe for the Future Circular Collider," Bachelor's thesis, TU-Darmstadt, 2015. 57, 79, 138

[105] B. Doliwa, H. De Gersem, T. Weiland, and T. Boonen, "Optimised electromagnetic 3D field solver for frequencies below the first resonance," *IET Sci. Meas. Technol.*, pp. 53–56, 2007. 57

[106] M. T. Jochum, "Niederfrequenzstabile Potenzialformulierungen zur Finite-Elemente-Simulation elektromagnetischer Felder im Frequenzbereich," Ph.D. dissertation, Universität des Saarlandes, 2013. 57

[107] M. Clemens and T. Weiland, "Discrete Electromagnetism with the Finite Integration Technique," *PIER*, vol. 32, pp. 65–87, 2001. 59

[108] T. Weiland et al., "Verfahren und Anwendungen der Feldsimulation I," *Lecture manuscript TU-Darmstadt*, 2012. 60

[109] A. Bossavit, "Generalized Finite Differences in Computational Electromagnetics," *PIER*, no. 32, pp. 45–64, 2001. 60

[110] B. Doliwa, H. De Gersem, and T. Weiland, "Numerical Calculation of Coupling Impedance for Kicker Modules," FAIR report, Tech. Rep., 2006. 61, 64

[111] ——, "Numerical Calculation of Coupling Impedance for Kicker Modules," FAIR report, Tech. Rep., 2004. 64

[112] Mathworks, "MATLAB," 2011. [Online]. Available: www.mathworks.com 64

[113] Microsoft, "Visual Studio 2008," 2007. 64

[114] "Portable, Extensible Toolkit for Scientific Computation," 2014. [Online]. Available: http://www.mcs.anl.gov/petsc/ 65, 72

[115] U. Niedermayer, O. Boine-Frankenheim, and H. De Gersem, “Space charge and resistive wall impedance computation in the frequency domain using the finite element method,” *Physical Review Special Topics - Accelerators and Beams*, vol. 18, no. 3, pp. 1–10, 2015. 69, 72, 138

[116] J. C. Nedelec, “Mixed Finite Elements in R3,” *Numer. Math.*, vol. 35, pp. 315–341, 1980. 69, 70

[117] ——, “A New Family of Mixed Finite Elements in R3,” *Numer. Math.*, vol. 50, pp. 57–81, 1986. 69

[118] D. N. Arnold, R. S. Falk, and R. Winther, “Finite element exterior calculus, homological techniques, and applications,” *Acta Numerica*, vol. 15, p. 1, may 2006. 70

[119] A. Logg, K.-A. Mardal, and G. N. Wells, *Automated Solution of Differential Equations by the Finite Element Method*. Springer, 2013. 70, 72

[120] P. Ingelström, “A New Set of (curl)-Conforming Hierarchical Basis Functions for Tetrahedral Meshes,” *IEEE Transactions on Microwave Theory and Techniques*, vol. 54, no. 1, pp. 106–114, 2006. 70

[121] “FEniCS,” 2014. [Online]. Available: www.fenicsproject.org 72

[122] C. Geuzaine and J.-F. Remacle, “GMSH 2.8.4 www.geuz.org/gmsh,” 2014. [Online]. Available: www.geuz.org/gmsh 72, 79, 138

[123] A. Logg, “Dolfin-Convert,” 2010. [Online]. Available: www.people.sc.fsu.edu/$\sim$jburkardt/py_src/dolfin-convert/dolfin-convert.html 72

[124] “https://bitbucket.org/uniederm/beamimpedance2d/src,” 2015. 72

[125] V. Kiselev and V. Smaluk, “Measurement of local impedance by an orbit bump method,” *Nuclear Instruments and Methods in Physics Research, Section A: Accelerators, Spectrometers, Detectors and Associated Equipment*, vol. 525, no. 3, pp. 433–438, 2004. 81

[126] N. Biancacci, “Improved techniques of impedance calculation and localization in particle accelerators,” Ph.D. dissertation, University of Rome "La Sapienza", 2014. 81

[127] L. Eidam, “Bench Measurements of Beam Coupling Impedance for SIS100 Components,” Master’s thesis, TU-Darmstadt, 2014. 81, 84, 85, 86, 91, 138

[128] F. Caspers, D. Möhl, and A. Schwinn, “A new Bench Method to simulate electromagnetic fields of Slow Beams,” in *Proc. of EPAC*, no. 2, 1990, pp. 1037–1039. 81

[129] M. Sands and J. R. Rees, “A Bench Measurement of the Energy Loss of a Stored Beam to a Cavity,” *SLAC-TN-05-051*, aug 1974. 82, 88, 89

[130] H. Hahn and F. Pedersen, “On Coaxial Wire Measurements of the Longitudinal Coupling Impedance,” *BNL Report 78-9*, 1978. 82, 88

[131] T. Kroyer, F. Caspers, and E. Gaxiola, “Longitudinal and Transverse Wire Measurements for the Evaluation of Impedance Reduction Measures on the MKE Extraction Kickers,” CERN AB-2007-28, Tech. Rep., 2007. 82

[132] F. Caspers, “Bench Methods for Beam-Coupling Impedance Measurements,” 1992. 82

[133] D. Pozar, *Microwave Engineering*. John Wiley & Sons, Incorporated, 1998. 82, 85, 87

[134] V. G. Vaccaro, “Coupling Impedance Measurements: An improved wire method,” *INFN/TC-94/023*, 1994. 85, 88

[135] J. Wang and S. Zhang, “Measurement of coupling impedance of accelerator devices with the wire-method,” *Nucl. Instrum. Meth. Section A Volume 459*, pp. 381–389, 2001. 87

[136] L. S. Walling, D. E. McMurry, D. V. Neuffer, and H. A. Thiessen, “Transmission-line impedance measurements for an advanced Hadron facility,” *Nucl. Instrum. Meth. Section A Volume 281*, vol. 281, pp. 433–447, 1989. 88, 89

[137] E. Jensen, “An improved log-formula for homogeneously distributed impedance,” *CERN PS/RF/Note 2000-001*, 2000. 88

[138] E. Karantzoulis, “An Overview of Impedances and Impedance Measuring Methods for Accelerators,” Sincrotrone Trieste, Tech. Rep., 1991. 89

[139] A. Argan, L. Palumbo, M. R. Masullo, and V. G. Vaccaro, “On the Sands and Rees Measurement Method of the Longitudinal Coupling Impedance,” in *Proc. of PAC*, no. 8, 1999, pp. 1599–1601. 89

[140] H. Hahn, “Validity of Coupling Impedance Bench Measurements,” *Physical Review Special Topics - Accelerators and Beams*, vol. 3, no. 084, p. 122001, 2000. 90

[141] "Rohde & Schwarz ZNB4," 2013. [Online]. Available: http://www.rohde-schwarz.de/de/Produkte/messtechnik-testsysteme/netzwerk-analysatoren/ZNB.html 94, 129

[142] E. Métral, F. Caspers, M. Giovannozzi, A. Grudiev, T. Kroyer, and L. Sermeus, "Kicker impedance measurements for the future multiturn extraction of the CERN Proton Synchrotron," in *Proc. of EPAC*, Edinburgh, 2006. 96

[143] J. Wang and S. Zhang, "Coupling impedance measurements of a model fast extraction kicker magnet for the SNS accumulator ring," *Nucl. Instrum. Meth. Section A*, vol. 522, no. 3, pp. 178–189, apr 2004. 97

[144] "Agilent E4980A," 2013. [Online]. Available: http://cp.literature.agilent.com/litweb/pdf/5989-4435EN.pdf 99

[145] J. Gareyte, "Impedances: Measurements and Calculations for Non-Symmetric Structures," in *Proc. of EPAC*, 2002. 103

[146] B. Salvant et al., "Update on Beam Induced RF Heating in the LHC," in *Proc. of IPAC*, Shanghai, China, 2013. 104

[147] F. Sacherer, "Transverse Bunched-Beam Instabilities," CERN Accelerator School, Tech. Rep., 1976. 106

[148] G. Arduini, E. Benedetto, H. Burkhardt, E. Métral, G. Rumolo, E. Shaposhnikova, and E. Métral, "Transverse Mode-Coupling Instability in the CERN Super Proton Synchrotron," CERN-AB-2005-020, Tech. Rep., 2005. 106

[149] E. Keil and W. Schnell, "Concerning longitudinal stability in the ISR," CERN/ISR-TH-RF/69, Tech. Rep., 1969. 109

[150] B. Zotter and F. Sacherer, "Transverse Instabilities of Relativistic Particle Beams in Accelerator and Storage Rings," CERN, Tech. Rep., 1976. 109

[151] M. Blaskiewicz, "Transverse stability with nonlinear space charge," *Physical Review Special Topics - Accelerators and Beams*, vol. 4, no. 4, pp. 89–97, 2001. 109

[152] V. Kornilov, O. Boine-Frankenheim, and I. Hofmann, "Stability of transverse dipole modes in coasting ion beams with nonlinear space charge, octupoles, and chromaticity," *Physical Review Special Topics - Accelerators and Beams*, vol. 11, no. 1, p. 014201, jan 2008. 109

[153] M. Blaskiewicz, "Fast head-tail instability with space charge," *Physical Review Special Topics - Accelerators and Beams*, vol. 1, no. 4, pp. 1–12, 1998. 109

[154] A. Burov, “Head-tail modes for strong space charge,” *Physical Review Special Topics - Accelerators and Beams*, vol. 12, no. 4, pp. 1–13, 2009. 109

[155] V. Kornilov and O. Boine-Frankenheim, “Head-tail instability and Landau damping in bunches with space charge,” *Physical Review Special Topics - Accelerators and Beams*, vol. 13, no. 11, p. 114201, nov 2010. 109

[156] U. Blell, “Injection and Extraction Components of SIS 100 / 300,” GSI Darmstadt, Tech. Rep., 2013. 110, 131

[157] U. Niedermayer and O. Boine-Frankenheim, “Estimation of beam induced heat load in SIS100 kicker magnets,” GSI Scientific Report, Darmstadt, Tech. Rep., 2013. 112

[158] T. Wietoska, “Optimierung der Ansteuerung von Ablenkmagneten in Teilchenbeschleunigern unter besonderer Berücksichtigung halbleiterbasierter Lösungen,” Ph.D. dissertation, TU Darmstadt, 2008. 112

[159] B. Doliwa, E. Arevalo, and T. Weiland, “Numerical calculation of transverse coupling impedances: Comparison to Spallation Neutron Source extraction kicker measurements,” *Physical Review Special Topics - Accelerators and Beams*, vol. 10, p. 102001, 2007. 112

[160] LinearTechnology, “LT Spice,” 2014. [Online]. Available: http://www.linear.com/designtools/software/#LTspice 113, 133, 139

[161] J. England et al., “Dielectric Laser Accelerators,” *Reviews of Modern Physics*, vol. 86, no. 102, pp. 1337–1389, 2014. 116

[162] H. Tsutsui, “On single wire technique for transverse coupling impedance measurement,” CERN-SL-Note-2002-034 AP, Tech. Rep., 2002. 120

[163] R. L. Gluckstern, J. van Zeijts, and B. Zotter, “Coupling impedance of beam pipes of general cross section,” *Physical Review E*, 1993. 123, 124

[164] U. Niedermayer and O. Boine-Frankenheim, “Numerical Calculation of Beam Coupling Impedances in the Frequency Domain using FIT,” in *Proc. of ICAP 2012*, Rostock, 2012. 127

[165] Ferroxcube, “8C11 Material specification,” Tech. Rep., 2002. 133, 134

Publication List

Journal Articles

- E. Metral, …, U. Niedermayer, *et al.*, “Beam Instabilities“, invited paper to be published in IEEE Transactions on Nuclear Science (TNS) to commemorate the 50th anniversary of the original Particle Accelerator Conference originally launched by the IEEE in 1965, 2015 (currently under review)
- U. Niedermayer, O. Boine-Frankenheim, and H. De Gersem, “ Space charge and resistive wall impedance computation in the frequency domain using the finite element method“,Phys. Rev. ST Accel. Beams 18, 032001, 2015
- U. Niedermayer, L. Eidam , and O. Boine-Frankenheim,“ Analytic modeling, simulation and interpretation of broadband beam coupling impedance bench measurements“,Nucl. Instrum. Methods Phys. Res. Sect. A 776, 129, 2015
- K. Klopfer, U. Niedermayer, H. Klingbeil, W. Ackermann, H. G. König, and T. Weiland, “Measurement of the magnetic material properties for ferrite-loaded cavities“, Phys. Rev. ST Accel. Beams 18, 010101, 2015
- U. Niedermayer and O. Boine-Frankenheim, “Analytical and numerical calculations of resistive wall impedances for thin beam pipe structures at low frequencies”, Nucl. Instrum. Methods Phys. Res., Sect. A 687, 51, 2012

Invited Talks

- FCC week, Washington, DC, USA “Single Beam Collective Effects for FCC-hh”, 2015
- TU-Darmstadt, Seminar ‘Physics and Technology of Accelerators’, “Determination of Beam Coupling Impedance in the Frequency Domain and Applications in Ion Synchrotrons”, 2014
- ICFA Mini-Workshop on Electromagnetic Wake Fields and Impedances in Particle Accelerators, Erice, Sicily, “Impedance Computation in the Frequency Domain”, 2014
- International Computational Accelerator Physics Conference (ICAP), Rostock, Germany, “Numerical Calculation of Beam Coupling Impedances in the Frequency Domain using the Finite Integration Technique”, 2012

Conference Proceedings

- U. Niedermayer and O. Boine-Frankenheim, Proc. of IPAC, Dresden, Germany, 2014
- U. Niedermayer and O. Boine-Frankenheim, Proc. of ICFA-HB, Beijing, China, 2012
- U. Niedermayer and O. Boine-Frankenheim, Proc. of ICAP, Rostock, Germany, 2012
- U. Niedermayer, O. Boine-Frankenheim, and L. Hänichen, Proc. of IPAC, San Sebastian, Spain, 2011

Supervised Theses

- Thilo Egenolf, “Impedance of the beam pipe for the Future Circular Collider”, Bachelor-Thesis, TU-Darmstadt, Department of Physics, May 2015
- Lewin Eidam, “Bench Measurements of Beam Coupling Impedance for SIS100 Components”, Master-Thesis, TU-Darmstadt, Department of Physics, Jan. 2014

Curriculum Vitae

Uwe Niedermayer
Eckhardtstr. 22
64289 Darmstadt, Germany

niedermayer@temf.tu-darmstadt.de
Office phone: +49 6151 16-75607

Education

24 Sept. 2015	PhD defense at TEMF TU-Darmstadt
7 April – 5 May 2013	Guest scientist (cooperation associate) at CERN (BE-ABP-ICE) Subject: impedance simulations
16-27 Jan. 2012	US particle accelerator school "Microwave Measurements and Beam Instrumentation Lab" in Austin, TX, USA
Sept. 2011 – present	PhD student at the Institute for Theory of Electromagnetic Fields (TEMF) at Technical University Darmstadt, Germany
Oct. 2005 – Aug. 2011	Diploma (equivalent to BSc. + MSc.) in electrical engineering at Technical University Darmstadt, Germany
July 2008 – May 2009	Student exchange with IIT (Indian Institute of Technology) Madras, Chennai, India
June 2004	Abitur (high school diploma), major subjects: Mathematics and Physics

Work experience

Feb. 2013 – present	Full position in TEMF research staff, TU-Darmstadt, Germany
Sept. 2011- Jan. 2013	PhD scholarship at TU-Darmstadt by GSI and HGS-hire graduate school
Apr. 2010 – Aug.2011	Student trainee at GSI, Department: Beam physics
Oct. 2009 – Apr.2010	Student trainee at GSI, Department: Synchrotron RF
June 2009 – Oct.2009	Internship at GSI Helmholtzzentrum für Schwerionenforschung GmbH (GSI Helmholtz-center for heavy ion research), Darmstadt, Germany Department: Synchrotron RF
Aug. 2005 – Oct. 2005	Internship at H. Kleinknecht GmbH, Siegen, Germany (automatic control)
Aug. 2004 – July 2005	Alternative civilian service at INVEMA e.V., Kreuztal, Germany (integration of disabled children in regular schools)

Language skills

German (mother tongue)
English (fluent)
French (medium level)